UC Berkeley
UC Berkeley Electronic Theses and Dissertations

Title
Marine Biogeochemical Cycling of Carbon and Cadmium

Permalink
https://escholarship.org/uc/item/9s42m00n

Author
Bourne, Hannah

Publication Date
2018

Peer reviewed|Thesis/dissertation

eScholarship.org Powered by the California Digital Library
University of California

Marine Biogeochemical Cycling of Carbon and Cadmium

by

Hannah Bourne

A dissertation submitted in partial satisfaction of the

requirements for the degree of

Doctor of Philosophy

in

Earth and Planetary Science

in the

Graduate Division

of the

University of California, Berkeley

Committee in charge:

Professor James Bishop, Chair
Professor Inez Fung
Professor Alice M. Agogino
Professor Phoebe Lam

Fall 2018

Marine Biogeochemical Cycling of Carbon and Cadmium

Copyright 2018

by

Hannah Bourne

Abstract

Marine Biogeochemical Cycling of Carbon and Cadmium

by

Hannah Bourne

Doctor of Philosophy in Earth and Planetary Science

University of California, Berkeley

Professor James Bishop, Chair

The actions of single celled organisms living in the surface ocean drive the distribution of many elements in the ocean - both vertically and horizontally across the ocean surface, determining global chemical signatures. Autotrophs fix CO_2 and dissolved nutrients into their cells, building biomass that forms the base of the food chain, providing the energy source for all higher trophic levels. The subsequent export of fecal pellets produced by zooplankton and small particles aggregated into larger particles drive the biological pump. The magnitude and processes of biomass export from the surface determines distributions of elements and the partial pressure of CO_2 near the surface, which ultimately affects global climate.While the spatial distribution of near-surface biomass is well quantified through high frequency satellite observations, observations of the vertical distribution and the processes determining these distributions are relatively few.

In the first section, I present a model predicting the horizontal global distribution of Cd, a toxic trace metal, in particles in the surface ocean. Particulate Cd concentrations is higher in HNLC environments with cold temperatures and low dissolved silica levels than in warm, oligotrophic regions. I hypothesize that this is due to inadvertent uptake of cadmium by transporter cells outside of cells targeting other divalent trace metals such as iron and zinc. In regions with low concentrations of bioavailable necessary divalent trace metals, Cd is more likely to be accidentally taken up by cells. Another finding in this study is that particulate P occurs in two forms with different labilities. One phase, such as phosphorus in DNA, is more labile than Cd while the other phase, such as P bound in phospholipids, is less labile than Cd. These differences in remineralization lead to subsurface Cd:P peaks occurring near the euphotic zone depth.

In the second part, I present the development of a novel in-situ sampling system which was integrated with robotic profiling floats called Carbon Flux Explorers. We built two of these integrated CFEs, which are called CFE-Cals. The CFE-Cals are capable of collecting particles in-situ while drifting with currents at depth. During a 30 day research expedition in June 2017 off the coast of California, I deployed the CFE-Cals 15 times. With samples collected during the expedition, I successfully calibrated the CFEs optical measurements of particle flux in terms of carbon and nitrogen. This translates sensor images into biogeochemical terms, and is an important step forward in the advancement of autonomous optical carbon export observations for quantifying processes in the carbon pump. Samples were collected in varied environments - from very productive near shore regions where export was dominated by large anchovy fecal pellets to low nutrient, low flux offshore waters dominated by small particles. Regression slopes for the optical properties measured by the CFE, Volume Attenuance (VA), to concentrations of particulate organic carbon and particulate nitrogen (units mATN-cm^2: mmol; R^2, n, p-value in parentheses) were 10.07×10^3 (0.86, 12, 5.7×10^{-8}), 10.05×10^4 (0.87, 15, 5.2×10^{-10}) respectively.

In the last section, I examine carbon export beneath a highly productive filament of nutrient rich upwelled water in dynamic waters off the coast of California. In this study, export is relatively high and increases with depth, contrary to typical observations of export magnitude rapidly attenuating with depth. These observations indicate that in coastal regions, efficient export by filtering organisms and lateral transport of material facilitate high levels of carbon export.

To My Family

Thank you for supporting me on my journey.

Contents

Contents **ii**

List of Figures **iii**

1 Introduction **1**
1.1 Dissertation Roadmap 4

2 Global Spatial and Temporal Variation of Cd:P in Euphotic Zone Particulates **7**
2.1 Introduction 7
2.2 Methods 13
2.3 Results and Discussion 16
2.4 Conclusions 29

3 Carbon Flux Explorer Optical Assessment of C, N and P Fluxes **32**
3.1 Introduction 32
3.2 Materials and Methods 34
3.3 Results and Discussion 44
3.4 Conclusions 51

4 Carbon Export Beneath a Dynamic Upwelled Filament off the CA Coast **53**
4.1 Introduction 53
4.2 Methods 59
4.3 Results 68
4.4 Discussion 83
4.5 Conclusions 89

5 Conclusions and Future Research **91**
5.1 Conclusions 91
5.2 Significance 92
5.3 Future Research 92

List of Figures

2.1 Map of sampling locations. MULVFS profiles are marked in red. GEOTRACES transects GA03 and GP16 (McLane samples) are marked in blue. 12
2.2 Comparison of rinsed (y-axes) and unrinsed (x-axes) P (left) and Cd (right) concentrations from combined 1-51 µm and <1 µm size-fractions taken at the SAFe site. Gray shading within the dashed lines represents 95% confidence interval of a single linear regression (solid orange line). Black line is the 1:1 line. Regression for P is significantly different from the 1:1 line and shows about a 7% loss of P in rinsed samples. Regression for Cd is not statistically different from 1:1 line. . 15
2.3 Particulate Cd:P, Cd, and P profiles from (a) the oligotrophic BATS site as part of the GEOTRACES Intercalibration I cruise, (b) 55 °S in an HNLC region during the SOFEX cruise, and (c) the Santa Barbara Basin as part of the GEOTRACES Intercalibration II cruise, where symbols show 3 size fractions: >51 µm (green triangles), 1-51 µm (red circles) and <1 µm (black squares). 17
2.4 Overlay of all open ocean upwelling MULVFS 1-51 µm size fraction profiles to show trend of subsurface peaks (excludes oligotrophic sites SAFe, ALOHA and BATS as well as the coastal anoxic Santa Barbara Basin which show different trends). Each profile offset so that base of the euphotic zone is at 0m. Symbols show Cd:P measurements made in the euphotic zone (light gray markers) and below the euphotic zone (black markers). 19
2.5 Particulate Cd (light blue bars) and P (dark blue bars) in the 1-51 µm size fraction normalized to profile-maximum values (bottom axis). Connected dashed black lines with black squares: dissolved oxygen (top/upper axis). Connected blue dotted lines: Cd:P ratio in the 1-51 µm size fraction (top/lower axis). Data above thick black lines are in the euphotic zones; data below line is below euphotic zone. Data are from Ocean Station Papa on March 3, 1996 (a), May 26, 1996 (b) and August 29, 1996 (c), SOFeX at 56.5 °S, 172 °W on January 12, 2002 (d) and 2.1°N, 141 °W on August 26, 1992 (e). 20
2.6 (a) Euphotic zone average Cd: P values in the combined <1 and the 1-51 µm size fractions along line P transect during the four cruises. Different shapes represent the different seasons. During the May and August 1996 cruises, day and night profiles were taken at OSP [Bishop et al., 1999]. 21

2.7 Average euphotic silicate (a), nitrate (b), temperature (c) and euphotic zone (d) depth vs. latitude at MULVFS sites. Open circles represent waters with < 0.3 µM surface dissolved phosphate; filled in circles >0.3 µM surface dissolved phosphate. 27
2.8 Regressions of actual to predicted euphotic zone Cd:P <51 µm particles for equation 1 (A) and equation 2 (B). 28
2.9 Seasonal euphotic zone predictions of particulate Cd: P from equations 1 and 2. The predicted maps are overlain with actual euphotic zone depth integrated average Cd: P data from the seasons they were collected during. The overlain data comes both from the MULVFS casts and the GEOTRACES McLane pump casts. The South Pacific transect in (D) is independent data not used in the creation of equation 1 or 2. 30
2.10 Seasonal euphotic zone predictions of particulate Cd: P from equations 1 and 2. The predicted maps are overlain with actual euphotic zone depth integrated average Cd: P data from the seasons they were collected during. The overlain data comes both from the MULVFS casts and the GEOTRACES McLane pump casts. The South Pacific transect in (D) is independent data not used in the creation of equation 1 or 2. 31

3.1 Left: CFE-Cal during deployment from R/V Revelle in 2017. The sampling system for particles is interfaced between the Optical Sedimentation Recorder (left) and SOLO float (right). Right: Map of CFE-Cal deployment and drift locations overlaying map of sea surface temperature. Sea surface temperature data averaged from June 10-17 from NASA Ocean Color Aqua Modis 4km resolution (https://oceancolor.gsfc.nasa.gov/). Blue dots within location boxes represent CFE-Cal 002 and red dots represent CFE-Cal 004 positions. 35
3.2 A) Typical deployment trajectory of a CFE-Cal. The x-axis is time in days (Jan 1 2017 at 1200UTC = day 0.5). The filled black circles are depths as the CFE-Cal is diving, open black squares denote depths as the CFE drifts and takes images of settled particles. The open black diamonds represent times when the sample stage was cleaned and particles directed into a sample bottle. B) Graph B shows the corresponding ATN for each photo taken. Particles build-up over time and then periodically the glass stage will be rinsed off and particles directed into the sample bottles. 37
3.3 (A) Sampler on CFE-Cal. Suction action of a pump draws water and particles down a poly tube to the sampler (shown disconnected). (B) Detail of particle retention system within sample bottles. Inlet is cone shaped to decelerate incoming flow. Outlet is formed to accommodate 51 µm mesh which is retained by two o-rings at the top. (C) Closeup of bottle with Mesh filter in place; Filter area is 130 cm^2. (D) CFE-Cal recovery after 24-hour deployment showing collected samples. Bottle 2 is shown in C. In this case, bottle 4 was a blank (i.e. no particles directed to it). 38

3.4 Sampler elements: (a) sample selector rotator; (b) main structural element of the sampler. Flow paths (1-4) direct water and particles into sample bottles or (0) to bypass sample bottles; and (c) particle retention system which bridges inflow channels and common exhaust manifold channel (5). Sample rotator is shown open at position 4. When not sampling, the rotator is sealed to closed positions. 39
3.5 Representative images of sampled particulates from locations 1-4. The process of sampling retains morphology of cohesive aggregates. Turbulence on transit from imaging stage to bottle does disrupt the integrity of loosely aggregated millimeter sized particles such as represented in Figure 3D. (a) Location 1. CFE 002 dive 42 - Days 160.623 to 160.791 - Depth 119.4 ± 7.8 m. (b) Location 2. CFE 004 dive 71 - Days 167.034 to 167.202 - Depth 157.6 ± 3.4 m. (c) CFE 002 dive 90 - Days 171.190 171.369 - Depth 126.9 ± 4.8 m. (d). Location 4. CFE 002 dive 101 - Days 174.479 to 174.646 - Depth 139.9 ± 3.0 m. 42
3.6 Representative images from four locations. The particle size classes present varied widely at the four different locations. (A) In location 1, flux was dominated by large 1 mm diameter anchovy fecal pellets. (B) Flux was dominated by small ovoid pellets 200-300 microns in diameter. (C) Location 3 was characterized by very low flux. Flux was dominated by small particles with the occasional large aggregate. (D) Flux was dominated by large aggregates. 45
3.7 Cumulative normalized volume attenuance vs. equivalent circular diameter curves representative of the 4 locations. Approximately 95% of flux was carried by aggregates >1.5 mm in size at locations 1 and 4. Location 2 had 50% of flux in >1.5 mm fraction. 46
3.8 Comparison counts of ovoid pellets in images versus on filters. (A) CFE-CAL002 Deployment 3 (first deployment at location 2) (B) CFE-CAL002 Deployment 4 (second deployment at location 2). 47
3.9 Data and regressions of sample POC (A), PN (B) and PP (C and D) vs. cumulative volume attenuance. Fits are forced through zero. Smaller symbols in all plots denote samples excluded from the POC regression analysis; these had C/N values >20 and were likely contaminated for carbon and not nitrogen. No data was excluded from PN or PP regressions. P regressions (C and D) include and exclude, respectively the high P enriched sample which was dominated by anchovy fecal pellets. In either case, the low R^2 for the VA:PP relationship implies that VA cannot be used to predict PP. 49
3.10 Regressions of ATN-POC (mATN-cm2 cm-2 d-1) to POC (mmol C m2 d-1) for this study (orange; y = 1.03x , R2=0.874), Estapa et al. (2017, blue, y = 1.56x + 0.434, R2 = 0.632; light blue, y = 2.191x, R2 = 0.47). Bishop et al. 2016 estimated slope (green) is 0.357 (1.0/2.8). Alldredge (1998) estimated slope (purple) = 6.25. As this study's calibration is created using samples collected at 150m, we separate out Estapa's (2017) data collected in 150m by marking in light blue for comparison. (A) shows the entire range of VAF and POC flux from this study. (B) zooms in to flux less than 3 so flux from Estapa et al. (2017) is highlighted. 50

4.1 CFE and CTD Locations. CTD cast locations are plus symbols. CFE1 (yellow), CFE-Cal 2 (red), CFE3 (cyan) and CFE-Cal 4 (dark blue). The CTD stations were close to a drifting surface drogued productivity array. For the majority of stations, the CTD and CFE are close to one another. However at location 2, the CFEs strongly diverge to the Northwest. A CFE-Cal is shown to the right. . . . 54
4.2 Martin curves reproduced from Martin et al., (1987), Buessler et al., (2007) and Bishop et al., (2016). B values of lines from left to right are: -1.33, -0.86, -0.51, -0.19 and -0.3 for stn. ALOHA, Martin et al., (1987), stn. K2 and Bishop et al., (2016) respectively. These values led to export efficiencies to 500m from 20% to 80% 56
4.3 Scenarios which could lead to flux not systematically decreasing with depth. (A) depicts constant flux at the reference depth over time, with differing values of "b". B values for the T=0, T=1 and T=2 lines are -0.6, -0.83 and -1.6 respectfully. (B) depicts decreasing flux at the reference over time with constant "b". Red marks indicate sampling points, illustrating how temporal delay could lead to observations of increasing flux with depth. Circles indicate sampled flux. 57
4.4 Different mechanisms which could lead to flux profiles which do not decrease with depth: (A) vertical migrators (B) temporal delay (C) physical subduction and (D) lateral advection 58
4.5 Surface chlorophyll evolving from late May to the end of June (A,C,E,G) and sea surface temperature over the same time period (B,D,F,H). All data is 8 day averaged 4 km resolution data from NASA Ocean Color from SNPP VIIRS. The stars represent the four locations. Stars are filled in maps from time periods during which sampling occurred. 60
4.6 Raw attenuance time series for location 1. The depth intervals for location 1 shown here - 70, 125 and 250m are different than the intervals from the other location because the water column was only 500m deep at location 1 and CFEs did not reach their target depths at most dives. Orange marks with black lines represent data collected by CFE1, green marks with green lines are collected by CFE2, blue lines with blue dots represent CFE3 and red lines with red dots are CFE4. Dotted line through time series represents time when CFEs were redeployed in a new area within the same location. See figure 4.1 for details. Italicized numbers are the dive numbers corresponding to the data. The mATN timeseries scales with flux as timing is constant. 62
4.7 Raw attenuance time series for each location 2. Orange marks with black lines represent data collected by CFE1, green marks with green lines are collected by CFE2, blue lines with blue dots represent CFE3 and red lines with red dots are CFE4. See figure 1 for details. Italicized numbers are the dive numbers corresponding to the data. The mATN timeseries scales with flux as timing is constant. 63

4.8 Raw attenuance time series for each location 3. Orange marks with black lines represent data collected by CFE1, green marks with green lines are collected by CFE2, blue lines with blue dots represent CFE3 and red lines with red dots are CFE4. Dotted line through time series represents time when CFEs were redeployed in a new area within the same location. See figure 1 for details. Italicized numbers are the dive numbers corresponding to the data. The mATN timeseries scales with flux as timing is constant. 64
4.9 Raw attenuance time series for each location 4. Orange marks with black lines represent data collected by CFE1, green marks with green lines are collected by CFE2, blue lines with blue dots represent CFE3 and red lines with red dots are CFE4. See figure 1 for details. Italicized numbers are the dive numbers corresponding to the data. For CFE002, dive 111, the milli-attenuance does not go back to zero on cleaning because of the presence of a swimming jelly. The mATN timeseries scales with flux as timing is constant. 65
4.10 Sensitivity of attenuance and particle enumeration to threshold level. In order to find the best threshold, a number were tested. The best threshold was determined to be 12 as lower than that, some individual particles would blend together, and above that, actual particles could be removed from the image. 67
4.11 Average Temperature (A), Salinity (B), Potential Density (C), Beam Attenuation Coefficient (D) and Nitrate (E) for each location. Profiles have been linearly interpolated for 1 meter resolution. Error bars represent 1 sigma standard deviation of casts. POC concentrations in units of µM may be derived by multiplying beam attenuation coefficient by 27 (Bishop and Wood, 2009). 69
4.12 Average current velocities in u and v. Data in the contour plots has been averaged in 30 minute bins for clarity. The CFE depth locations are plotted over the contours. Data to right of contour plot shows average velocities measured by the ADCP over the entire time span represented with black astericks. Red points represent average CFE velocities over the course of a dive. Filled blue triangles are the averaged CFE velocities for all dives at a given depth. Averaged CFE velocities closely correspond to time averaged ADCP velocity, as expected for a lagrangian instrument. Part A, B, C, D and E represent Locations 1, 2a, 2b, 3 and 4 respectively 71
4.13 Continuation of figure 4.12. Average current velocities in u and v. Data in the contour plots has been averaged in 30 minute bins for clarity. The CFE depth locations are plotted over the contours. Data to right of contour plot shows average velocities measured by the ADCP over the entire time span represented black astericks. Red open circles represent average CFE velocities over the course of a dive. Filled blue triangles are the averaged CFE velocities for all dives at a given depth. Averaged CFE velocities closely correspond to time averaged ADCP velocity, as expected for a lagrangian instrument. Part A, B, C, D and E represent Locations 1, 2a, 2b, 3 and 4 respectively 72

4.14 A. Average sea surface height from June 1-5, 16-20 and 21-25. In the beginning of June, sea surface height is low near the shore due to Ekman transport, and higher off the coast. As the filament develops and moves out to the west, a sea surface depression about 200 km offshore forms and is first apparent in the June 16-20 map, and deepens in the 21-25 map, indicating the formation of a cyclonic eddy. Anti-cyclonic eddies are present to the north and south. Stars represent positions of each location. B. Velocities of all CFE dives, from depths down to 500m. The CFE trajectories are fastest at locations 2 and 3, where the CFEs are deployed near the edges of the eddies and slowest at location 1, where overall velocity is affected by fluctuating tides, and at location 4, near the center of the eddy. 73
4.15 SEM image of anchovy fecal pellet. Contains mostly diatom frustules. 74
4.16 Size distribution with depth. Right hand side of the axis is cumulative normalized particle distribution. The majority of particles at all sites and depth are small. The left side of the axis represents cumulative normalized attenuance. Images on the right hand side are representative images at each location and depth. 75
4.17 Size distribution with depth. Panels same as for figure 4.16 76
4.18 Size distribution with depth. Panels same as for figure 4.16 77
4.19 Size distribution with depth. Panels same as for figure 4.16 78
4.20 Volume attenuance flux at each location. At location 1 and 4, export is nearly constant with depth and at cycle 2 and 3, export levels increase with depth. Martin curve fits have b values of 0.97 and 0.69 for locations 2 and 3 respectfully. 80
4.21 Flux of small (red) vs large (black) particles with depth at location 2. Small particle flux does decrease with depth whereas large particle flux (>1mm) increases with depth. Martin curve fits have b values of -1.07 and 1.34 for small and large particles respectfully. 81
4.22 Transects along filament of potential density (a), chlorophyll fluorescence(b) and non-sinking POC (c). The bottom at location 1 is about 500m. At location 2 and 4 it is greater than 2000m deep. Vertical black lines separate the four locations. 82
4.23 (A) Carbon flux for June climatology predicted by model in Siegel et al., 2014 (B) Extrapolating flux from Siegel et al., 2014 down to 150m using equation 4.1. The b value found at the nearby VERTEX I location (-0.83) was used (Martin et al., 1987). The euphotic zone base depth (Z_{eu}) used was June climatology data from NASA VIIRS (https://oceancolor.gsfc.nasa.gov/l3/order/) The contour plot is overlain by CFE flux data collected between 100 and 200m. (C) Carbon flux extrapolated down to 250m using the same method. The contour plot is overlain by CFE flux data collected between 200 and 300m. 84

Acknowledgments

The pursuit of a doctorate degree is a long journey. It is impossible to achieve without the support of colleagues, friends and family. I would first and foremost like to thank my advisor, Professor Jim Bishop. Throughout my dissertation, he pushed me to achieve the highest quality research. I am grateful to Jim for guiding me through graduate school, and for his support and encouragement throughout. I have learned much from him over the past 5 years and greatly appreciate his mentorship.

I would also like to thank my dissertation committee members, Professor Inez Fung, Professor Alice Agogino and Professor Phoebe Lam. Their feedback and guidance greatly expanded my growth as a scientist. They were all exceptional role models for me throughout graduate school.

To my colleagues at Lawrence Berkeley National Laboratory, I would first like to thank Todd Wood for all of his help both in the lab and at sea. Todd taught me many programming and problem solving skills. I'd also like to thank Tim Loew for his design work on the CFE-Cal samplers. Thank you also to Alejandro Morales and Michelle Robertson.

Thank you to the faculty, graduate students and staff in the Earth and Planetary Science Department, it was a wonderful community to be part of these past 5 years.

I would like to thank Mark Ohman (chief scientist), members of the science party, and captain and crew of the R/V Revelle for facilitating CFE-Cal deployments during the June 2 - July 1 2017 California Current Ecosystem Long Term Ecological Research process study. Thank you also to Ralf Goericke for his help and nutrient analysis of CTD samples from the CCE-LTER cruise discussed in Chapter 4 (available at https://oceaninformatics.ucsd.edu/datazoo/catalogs/ccelter/datasets). Thank you to Mark Ohman and Mike Stukel for sharing their expertise on the coastal California ecosystem.

Thank you also to Christopher Parsell and the Jacobs Institute for Design Innovation at UC Berkeley (UC Berkeley), Christopher Myers (UC Berkeley), Mike McLune (SIO), and Rob Franks (UC Santa Cruz).

I'd also like to thank the many UC Berkeley undergraduates who have worked with me at sea and in the laboratory; Beth Connors, Xiao Fu, Yizhuang Liu, Casey Fritz, Sylvia Targ, Louis Claxton, Imari Walker, Jessica Kendall-Bar, and William Kumler.

This work was funded by the US National Science Foundation grant OCE 0936143 which supported Carbon Flux Explorer development; OCE 1528696 which supported the development and at sea work with the CFE-Cal systems. The CCE-LTER is supported by US NSF grant OCE 16-37632. The MULVFS particulate sampling was supported by NSF OCE

grants 0826335, 0826514 and 0930064 (GEOTRACES); NSF OCE 9022308 (EqPac) and NSERC Canada (LineP). NAZT GA03 was funded by OCE-0963026 and EPZT GP16 was funded by OCE-1ata518110.

Lastly, I would like to thank my family: my mother, father, grandparents, Chloe and Lee, thank you for all of your support along the way. I would not be able to accomplish this without you.

Chapter 1

Introduction

Oceans remain one of the last frontiers on the planet as a majority of the ocean, which covers 71% of the Earth's surface remains largely unexplored. The vertical distribution of elements such as carbon, nutrients and trace metals is driven by the utilization of these elements by phytoplankton in the surface ocean, and then the subsequent export of organic matter into the deep ocean. The process by which photosynthetically derived biomass is exported out of the euphotic zone into the deep ocean is known as the biological carbon pump. The biological pump moves not just carbon, but also nutrients through the water column.

The biological pump leads to lower concentrations of such elements in the surface ocean, and progressively higher concentrations going down the water column as organic matter is respired back to the dissolved pool. How these elements are taken up at the surface, the amount of biomass exported and the depth of remineralization is important for a number of reasons.

For elements which do not have a gas phase, such as macronutrients like phosphorous and micronutrients like iron, their availability affects plant growth. Many areas in the ocean are growth limited by either a macro or micronutrient.

For elements such as carbon which have a gas phase, this process affects their atmospheric concentrations. Atmospheric carbon dioxide concentrations are set by the ocean (Sabine et al., 2004). This is in part controlled by the depth at which sinking organic matter is dissolved (Kwon et al., 2009). As carbon dioxide is an important greenhouse gas whose concentrations are rapidly increasing due to anthropogenic activities, it is of crucial importance understand the current processes driving the biological pump in order to predict future climate change.

The ocean plays a pivotal role in the global carbon cycle. Each year, plants growing in the surface ocean fix about the same amount of carbon during photosynthesis as land plants do, about 50 Pg C yr^{-1}. If we were to weigh all the plant biomass living in the surface ocean

at this moment, it would only be about 1 Pg C (Bar-On et al., 2018). This means that plankton populations turn over every week or two.

Currently, we live in an age of big data. The launch of the NASA Coastal Zone Color Scanner (CZCS) in 1978 and then Sea-viewing Wide Field of view (SeaWIFs) in 1997 precipitated a rapid expansion in knowledge of upper ocean processes as high frequency spatial and temporal data of phytoplankton biomass was made readily available.

Satellite observations give us a high frequency view of chlorophyll production so we can globally measure how plants are taking up CO_2 and see spatial and seasonal variation as well as long term trends. We can clearly observe where production is low, such as in our ocean gyres and where it is high such as in coastal regions using satellite imaging.

However, that same level of data resolution has not been possible in chemical oceanography. Samples need to be collected at sea, and then those samples need to be processed and analyzed in a lab. Chemical distribution data for the ocean is more limited, though rapidly expanding through programs such as Geotraces. What is more difficult to observe, and therefore more difficult to understand, is how carbon fixed by plants at the surface is transported to depth.

This leads to one of the central questions of this dissertation, how do we relate surface ocean properties, observable at high resolution by satellites, to chemical processes occurring both at and beneath the surface?

The current estimate for the strength of the biological pump, in other words, how much carbon it moves each year from the surface to the deep ocean, is about 10 Pg C each year (Li and Cassar, 2011). This rate of 10 Pg C yr^{-1} is about equal to what we know human activities, mainly the burning of fossil fuels, emit each year.

How much material is exported out of the surface layer, and how deep the material reaches before dissolution is important for two reasons. One is that the biological carbon pump is an important regulator of atmospheric CO_2. Typically, the deeper POC reaches in the water column before it is respired back to aqueaous CO_2, the longer it will be sequestered from the atmosphere. The timescale for sequestration in the deep ocean can be hundreds of years.

The second reason is that the only place in the ocean where photosynthesis occurs is the very thin strip at the surface where sunlight reaches, this layer is only on average 100m deep, depending where you are. All metabolic activity in the water column and on the seafloor is ultimately fueled by this vertical flux of material out of the surface layer.

We know that the BCP is an important process to the global cycling of nutrients and that its strength affects our atmospheric CO_2 levels. However, there are still a number of large uncertainties associated with this important process. One is that different models estimate

the strength of the BCP to be anywhere from 5 to >12 Pg C y^{-1}(Boyd and Trull, 2007; Henson et al., 2011; Li and Cassar, 2016; Dunne et al., 2005; Siegel et al., 2014, 2016; Yao and Schlitzer, 2013). This range is almost as large as our current anthropogenic emissions.

The other current issue with biological pump estimates is that, as sinking material derived from the surface is the ultimate food source for all microbes and animals living deeper in the water column and on the sea floor, the influx of sinking organic substrates has to be enough to meet the metabolic demands of organisms below. However, recent global budgets and intensive field studies suggest that there is higher metabolic demand than can be met by the measured amount of sinking material (Banse, 2013; Burd et al., 2010; Ebersbach et al., 2011; Passow, 2012; Stanley et al., 2012).

This imbalance indicates that there are unaccounted for mechanisms by which sinking organic matter is exported to the deep ocean that our conventional techniques for measuring are not detecting. If we don't know the all the mechanisms by which organic material is moving into the deep ocean, and we don't have a strong estimate for the current strength of the BCP, we can't predict how those mechanisms may change in response to climate change, and how that will affect the overall strength of the BCP.

In order to understand how material moves vertically through the water column, oceanographers deploy sediment traps in the water column. Traditionally, surface tethered traps are used. In the past two decades, there has been a move toward neutrally buoyant traps as these avoid hydrodynamic biases (Buessler et al., 2007; Stanley et al., 2004; Owens et al., 2013; Bishop et al., 2016).

What is typically observed at open ocean sites is a decreasing amount of sinking material with depth. The amount of material that makes it to depth compared to the amount of material that makes it to depth is referred to as the export efficiency of the pump. Export efficiency can vary regionally. Typically, in warmer, less productive waters export efficiency is lower, whereas in cooler, more productive waters efficiency is higher (Buessler et al., 2007).

John Martin found that a simple mathematical way to describe his flux observations was a power law function, so we call such profiles Martin Curves (Martin et al., 1987). Such power law functions, based on best fits of sediment trap data are widely used to extrapolate fluxes to different depths and also to model flux attenuation in ocean carbon models.

The vertical movement of material through the water column is controlled by a complex web of processes. Each of these pathways can be thought of as a mechanism important to the vertical transportation of carbon. The vertical flux of particles is due to a combination of mechanisms including sinking fecal pellets produced by zooplankton, sinking aggregates, lateral advection, vertical mixing and transport of organic material by animals (Turner, 2015). The relative contribution of these different mechanisms to overall flux can vary both regionally and seasonally.

To understand these processes requires high frequency observations as plankton life cycles are so rapid. Manually collected profiles captures only a brief snapshot in time. In two different ways, this dissertation seeks to create a broader understanding of biogeochemical processes.

1.1 Dissertation Roadmap

1.1.1 Overview Chapter 2

Cadmium is an acutely toxic element with few known biological functions. However, dissolved Cd has a nutrient like profile in the water column, closely following that of phosphorous, an essential element to all life forms. The fact that a toxic element exhibits a nutrient like profile is somewhat perplexing. Though the mechanistic reasoning for this remained largely unknown, the quasi-linear relationship between dissolved cadmium and phosphate has been utilized to infer paleo-deep water phosphate distributions and ocean circulation patterns of the Atlantic through analyses of Cd:Ca ratios in the shells of benthic foraminifera in marine sediments (Boyle, 1988).

In order to understand the mechanism of Cd uptake into organic matter, concentrations of Cd and P were determined in particle samples collected using the Multiple Unit Large Volume in-situ Filtration System (MULVFS) from 50 profiles at 34 different locations throughout the Atlantic, Pacific and Southern Oceans since 1991. Consistent methodology was used. This dataset of Cd:P in size fractionated particles gives insight into the processes that lead to differences in regional Cd:P particle values as well as how the formation and remineralization of these particles lead to dissolved deep-water ratios that increase from the North Atlantic to the North Pacific. With large spatial and temporal variation, this dataset allows us to study the effects of an El Nino, upwelling, large scale in-situ Fe fertilization, low oxygen conditions, and seasonal variation on the Cd:P in particles.

Overall, Cd:P tends to be higher (1-2 mmol/mol) in particles gathered in biologically dynamic waters and is much lower (typically 0.1 mmol/mol) in oligotrophic regions. Using multiple linear regression analysis, I investigate how euphotic zone parameters important to photosynthesis including nitrate, phosphate, silicate, temperature, and euphotic zone depth affect the Cd:P ratio in particles. Using the results of the analysis, I create global seasonal maps of predicted particulate Cd:P distributions. Three factors - local dissolved nitrate and silicate concentrations and euphotic zone depth can predict 59% of the variation in particulate Cd:P. I verified these projections using in-situ filtration samples collected during GEOTRACES expeditions GA03 (North Atlantic) and GP16 (South Pacific). I have published this study in Global Biogeochemical Cycles (Bourne et al., 2018a).

Major findings

- Global euphotic particle Cd:P varies greater than order of magnitude with highest values found in low silicate, high nitrate environments

- 59% of surface Cd:P variation can be explained by factors important to photosynthetic rates and ecosystem state
- Vertical particle Cd:P variation due to P being present in two pools, one more labile to remineralization than Cd and one more refractory

1.1.2 Overview Chapter 3

The magnitude and controls of particulate carbon exported from surface waters and its remineralization at depth are poorly known. The Carbon Flux Explorer (CFE), a Lagrangian float-deployed imaging sediment trap, was designed to optically measure the hourly variations of particle flux to kilometer depths for months to seasons while relaying data in near-real time to shore via satellite without attending ships.

The main optical proxy of particle load recorded by the CFE, volume-attenuance (VA; units of mATN-cm^2), while rigorously defined and highly precise, has not been robustly calibrated in terms of particulate organic carbon (POC), nitrogen (PN), and phosphorus (PP).

In this chapter, a novel 3D printed particle sampler using cutting edge additive manufacturing was developed and integrated with the CFE is presented. Two such modified floats (CFE-Cals) were deployed a total of 15 times for 18-24-hour periods to gain calibration imagery and samples at depths near 150 meters in four contrasting productivity environments during the June 2017 California Current Ecosystem Long Term Ecological Research (LTER) process study. Regression slopes for VA: POC and VA:PN (units mATN-cm^2: mmol; R^2 in parentheses) were 10.07×10^3 (0.86), 10.05×10^4 (0.87) respectively and was not sensitive to environment or classes of particles sampled. PP was not strongly correlated with VA. At the time of this dissertation submission, this study is in review in the open source journal Biogeosciences (Bourne et al., 2018b).

Major findings

- Successful sampler designed for deployment on free-drifting robot
- Strong calibration of volume-attenuance to POC (r^2=0.86) and PN (r^2=0.87)
- Broad range of particle sizes and fluxes

1.1.3 Overview Chapter 4

Export dynamics in Eastern boundary current upwelling regimes are poorly understood as most sediment trap profiles reaching greater than 500 m depth have been made in open ocean environments. Complex current systems and productivity fluctuations make collection and

interpretation of export difficult. Beneath a highly productive filament evolving over time, we observe a diverse array of export mechanisms with fairly high flux. High flux at depth was not always correlated to high chlorophyll at the surface. While export higher in the water column was very diverse, at all locations export 250m and below was dominated by large aggregates. Export measured at 150, 250 and 500 m was either fairly constant with depth, or, as we found in two cases, increased with depth. This is likely not due to physical subduction of non-sinking particles or an effect of temporal delay but rather the combined result of migrating organisms and lateral transport. At the time of this dissertation submission, I am preparing this study for submission to Global Biogeochemical Cycles (Bourne et al., in prep).

Major findings

- Particle type dominating export varied greatly spatially at 150m, but was similar at 250m and below
- Export increased with depth, contrary to expected
- Higher export than predicted

Chapter 2

Global Spatial and Temporal Variation of Cd:P in Euphotic Zone Particulates

2.1 Introduction

Dissolved cadmium exhibits a nutrient-like profile with strong surface depletion and maximum concentrations in the 1000-1500 m depth interval and closely follows the profile systematics of dissolved phosphate [Boyle et al.;1976; Bruland et al., 1978]. Cadmium, however, is an acutely toxic element with few biological functions, while phosphate is an essential macronutrient element. The quasi-linear relationship between dissolved cadmium and phosphate and corresponding analyses of Cd:Ca ratios in the shells of benthic foraminifera in marine sediments has been used to extrapolate paleo-deep water phosphate distributions and ocean circulation patterns of the Atlantic [Boyle, 1988]. More recently, it has been used to study changes in phosphate utilization during the last glacial-interglacial in the Southern Ocean [Elderfield and Rickaby, 2000].

Although dissolved Cd has a residence time of 50,000 years, it exhibits strong biological cycling, thus deep-water Cd concentrations increase from the North Atlantic (0.3-0.4 nM) to the North Pacific (1 nM) [Bruland, 1980, Bruland and Franks, 1983; Danielsson et al., 1985, Mawji et al., 2015, Xie et al., 2015, John et al., 2017]. The ratio of dissolved Cd to P (units of mmol:mol) follows a parallel trend, increasing from 0.2 in the North Atlantic to 0.35 mmol:mol in the North Pacific [Waeles et al., 2013]. These inter-basin differences can be explained by an enhanced accumulation of Cd relative to P over time as deep water flows from the Atlantic to the Pacific over the thousand-year time scale of deep water circulation. Mechanistically, this could suggest regional differences in Cd:P fixation in surface waters and/or the differential remineralization of the elements from sinking particles.

Regardless of mechanism, however, the deep dissolved element pools can be presumed to represent the integrated signature of Cd:P uptake and remineralization over a great span of time. Particles, on the other hand, turn over on the timescale of 1 week in surface waters

and 1 year timescales in the deeper water column [eg. Bishop et al., 1999]. Hence direct analyses of particles allows investigation of local processes at or near to the time and location of sampling.

2.1.1 Mechanisms for Drivers of Particulate Cd:P Variation

The main processes driving variable Cd uptake in marine phytoplankton are not definitively known. Over the past two decades, several mechanisms have been proposed that could lead to uptake and accumulation of Cd by biota and thus its nutrient-like vertical dissolved distribution. These mechanisms can be split into two main groups: deliberate, in which Cd is actively taken up by phytoplankton for specific physiological functions; and passive bioaccumulation, generally associated with the active uptake of other bioactive trace metals. In our analysis of the spatial and seasonal differences in the Cd:P of our euphotic zone particulate samples, we explore six such mechanisms, described in detail below.

Passive uptake driven by relative abundance of metals (M1)

Phytoplankton uptake of dissolved Cd has been shown to be positively correlated with free dissolved Cd(II) concentrations and inversely correlated with free dissolved Zn(II) and Mn(II) concentrations in both shipboard incubation [Cullen et al., 1999; Cullen and Sherrell, 2005] and laboratory experiments [Price and Morel, 1990; Sunda and Huntsman, 1998, 2000]. This relationship likely arises from competition by these ions for cellular uptake sites [Sunda and Huntsman, 1996, 1998, 2000]. It has been suggested that Cd (II) may be taken up by the same transport receptors as Fe(II); when Fe (II) levels are lower, the cell then takes up higher levels of Cd(II) [Lane et al., 2009]. Laboratory isotope site-specific fractionation experiments have shown that Cd is likely taken up passively with other divalent metals [Horner et al., 2013], and then bound within the cell to prevent toxicity. Therefore, in areas with relatively high dissolved Cd:Zn, Cd:Fe or Cd:Mn concentrations, phytoplankton will take up more Cd.

Deliberate Cd uptake under low Zn conditions (M2)

The nutrient-like profile of dissolved Cd was first attributed to abiotic processes as no biological use for Cd had been demonstrated [Price and Morel, 1990]. In 1990, Price and Morel found that the diatom, Thalassiosira weissflogii, when grown in Zn limiting conditions, could grow at 90% of their maximum rates when supplied with Cd. Later, it was shown that marine diatoms use Cd in carbonic anhydrase (CA), an enzyme that catalyzes the formation of carbon dioxide from bicarbonate and vice versa [Lane and Morel, 2000]. Xu et al. [2008] reported the crystal structure of cadmium carbonic anhydrase (CDCA1) and showed how CDCA1 is a cambialistic enzyme that can use either Zn or Cd. Therefore, substitution of

Cd for Zn in diatoms for CA can relieve stress of Zn limitation [Price and Morel, 1990; Lee et al., 1995; Lane and Morel, 2000; Baars et al., 2014]. This mechanism would especially affect Cd:P in regions dominated by diatoms.

Biodilution (M3)

Dissolved iron levels have been shown to affect uptake of Cd by phytoplankton [Martin et al., 1989; Sunda and Huntsman, 2000; Cullen, 2006; Lane et al., 2009]. In HNLC regions where iron is the limiting factor in phytoplankton growth, Cd:P in phytoplankton in these regions tends to be higher than phytoplankton in iron replete conditions [Cullen, 2006; Lane et al., 2009]. The higher Cd:P of phytoplankton in HNLC regions was attributed to growth rate or biodilution [Sunda and Huntsman, 2000; Cullen, 2006]. In other words, while Cd uptake is relatively constant, the accumulation of biomass can vary depending on nutrient availability and growth conditions. As a result, in HNLC areas where growth is limited by iron availability, biomass and P accumulation is slower while Cd uptake is constant, leading to higher Cd:P ratios in plankton [Cullen, 2006]. Oligotrophic regions, where growth is limited by macronutrients, would have lower Cd:P.

Species composition (M4)

Biological variability of metal quotas of phytoplankton is large and poorly constrained. There can be great variations of P-normalized metal quotas between taxonomic groups and also between different species within a taxonomic group. There is especially high variability in Cd quotas; while other P-normalized trace metal quotas among different species were within a factor of 20, the Cd quotas for different species ranged over two orders of magnitude [Ho et al., 2003].

Laboratory cultures grown in nutrient replete conditions show that Cd:P content varies in different phytoplankton taxonomic groups. For example, diatoms on average have Cd:P ratios three times lower than coccolithophores when grown in a lab in nutrient replete conditions [Finkel et al., 2007]. A different culture study found in both Fe-sufficient and Fe limited conditions that open ocean diatoms had a relatively low Cd:P compared to coccolithophores [Lane et al., 2009]. The difference within the taxonomic group can be quite large as well. In the Southern Ocean, Fe-limited pennate diatoms had about 4 times lower Fe:P ratios than centric diatoms [Twining and Baines, 2013]. Cyanobacteria, which likely evolved during a time of sulfidic or ferruginous oceans when Cd bioavailability would have been low, have amongst the lowest Cd quotas [Saito et al., 2003, Finkel et al., 2007]. The differences in Cd quotas among different species, and how those species quotas change with nutrient availability can therefore affect the Cd:P in particles.

CdS formation (M5)

A proposed abiotic mechanism for accumulation of particulate Cd formation is authigenic cadmium sulfide (CdS) precipitation in euxinic microenvironments of sinking aggregate particles in oxygen minimum zones (OMZ). The fragmentation of aggregates as they sink enriches the small sized particle pool with CdS particles [Janssen et al., 2014].

Uptake proportional to dissolved concentrations (M6)

A simple mechanism, first suggested by Elderfield and Rickaby (2000), argues that preferential uptake of dissolved Cd relative to P by cells in surface waters occurs with a fractionation factor of about 2.5. Therefore, particles will be enriched in Cd:P compared to the dissolved Cd:P of surface waters. Dissolved Cd:P increases with latitude [Elderfield and Rickaby, 2000; Roshan et al., 2017]. Following this mechanism, in high latitude environments where both dissolved P and Cd:P are high, the Cd:P of particles will be high.

2.1.2 Systematics of Cd:P in the ocean

Compared to the compilations of dissolved Cd profiles, published datasets of particulate Cd are few, and the ratios of Cd:P in phytoplankton have been indirectly estimated only at select sites or in laboratory cultures [Ho, 2003; Twining and Baines, 2013]. In this study we look at the Phosphorus - normalized Cd content in euphotic zone particulates collected using Multiple Unit Large Volume Filtration (MULVFS) from the world's oceans[Bishop et al., 2012]. We aim to quantify the wide range of cellular Cd:P in phytoplankton, and to identify which of the above biotic and abiotic uptake processes may explain the observed variations. The ratio of cadmium to phosphorous was measured in 50 profiles (Table 2.1). The sampling has wide spatial coverage - including polar regions, and to our knowledge represent the only case of seasonal sampling over thousand-kilometer long transects. Together these attributes allow us to study the effects of an El Nino, upwelling, large scale in situ Fe fertilization, Zn limitation, anoxic conditions, a phytoplankton bloom decline and seasonal variation. By comparing at each site how euphotic zone Cd:P varies with spatial, hydrographic and biological variables such as latitude, euphotic zone depth, nitrate, phosphate, silicate, and temperature, we can evaluate whether there is a statistically significant association between these conditions and Cd vs. P uptake in particles. This information is then used to predict how Cd:P varies spatially and temporally around the world. We test our empirical model by comparing particle data collected during two GEOTRACES expeditions. We also investigate how Cd:P varies in particles to kilometer depths to infer the relative lability of Cd and P.

Stn.	**Date**	**Latitude**	**Longitude**	**Depth**	**Temperature**	**Silicate**	**Nitrate**	**Phosphate**	**Cd: P** $<51\,\mu m$	**Cd: P** $>51\,\mu m$
EP 3	2/8/92	9.00	-140.01	109	20.99	12.74	12.77	1.03	0.76	0.63
EP 6	2/15/92	3.00	-140.01	118	28.06	3.48	3.33	0.55	0.68	0.57
EP 8	2/21/92	1.42	-140.48	124	27.45	5.33	6.31	0.73	0.85	0.46
EP 9	2/24/92	0.00	-140.41	140	23.96	6.19	9.40	0.95	0.77	0.47
EP 10	2/27/92	-1.07	-140.3	116	27.97	2.92	5.33	0.74	0.40	0.42
EP 11	3/1/92	-1.95	-140.8	140	26.85	6.11	10.89	1.09	0.67	0.53
EP 12	3/3/92	-5.07	-140.04	124	28.06	1.88	3.38	0.51	0.37	0.51
EP 13	3/7/92	-12.03	-135.02	136	26.43	0.82	0.46	0.62	0.29	0.30
EP 16	8/11/92	12.01	-140.1	120	22.07	4.85	6.09	0.57	0.74	3.61
EP 17	8/13/92	8.97	-139.99	114	23.29	10.11	12.90	1.07	0.74	0.76
EP 18	8/17/92	7.05	-139.85	122	23.67	3.57	2.74	0.32	0.90	0.61
EP 19	8/20/92	4.95	-139.84	112	27.19	4.87	3.76	0.44	0.83	0.59
EP 20	8/22/92	2.80	-140.48	100	25.11	2.82	5.14	0.45	0.60	0.83
EP 21	8/26/92	2.10	-141.35	98	22.35	5.85	10.21	0.80	2.00	1.25
EP 22	8/27/92	1.27	-140.03	92	23.84	4.29	8.38	0.70	1.41	0.74
EP 23	8/30/92	0.33	-139.56	92	23.68	4.49	9.24	0.69	1.18	0.74
EP 24	9/1/92	-1.13	-139.98	118	22.29	5.25	10.13	0.91	1.36	0.59
EP 25	9/4/92	-2.45	-140.47	98	25.23	3.53	7.00	0.75	0.96	0.58
EP 26	9/6/92	-3.39	-140.46	108	24.90	1.69	5.75	0.47	1.04	0.69
EP 27	9/9/92	-5.35	-139.78	98	25.62	1.38	4.88	0.52	0.79	
EP 28	9/14/92	-11.85	-134.95	138	25.73	0.27	0.55	0.38	0.41	0.40
M96 OSP	3/1/96	50.00	-145	80	5.95	19.09	12.61	1.25	1.36	1.38
M96 P4	5/9/96	48.66	-126.67	20	10.52	7.32	1.55	0.43	0.52	
M96 P16	5/13/96	49.30	-134.7	40	8.31	9.07	6.97	0.88	0.71	0.57
M96 P20	5/16/96	49.60	-138.7	35	7.45	10.65	8.97	1.01	1.08	0.56
M96n OSP	5/19/96	50.00	-145	60	6.56	18.24	11.78	1.18	1.05	1.02
M96d OSP	5/21/96	50.00	-145	60	6.56	18.24	11.78	1.18	1.06	0.85
M96 12	5/26/96	49.00	-130.7	60	9.12	7.42	4.39	0.74	0.76	0.43
A96 P4	8/16/96	48.66	-126.67	20	14.37	3.80	0.10	0.39	0.73	0.55
A96 P12	8/19/96	49.00	-130.7	40	13.79	2.43	0.61	0.43	0.55	0.44
A96 P16	8/22/96	49.30	-134.7	40	13.08	2.15	1.17	0.48	0.46	0.38
A96 P20	8/25/96	49.60	-138.7	35	12.32	11.93	5.54	0.77	1.06	
A96n OSP	8/29/96	50.00	-145	40	10.44	14.67	9.26	1.03	1.38	1.30
A96d OSP	8/30/96	50.00	-145	40	10.44	14.67	9.26	1.03	1.67	1.34
F97 P4	2/14/97	48.66	-126.67	30	8.46	11.20	8.19	0.92	0.82	0.53
F97 P16	2/16/97	49.30	-134.7	60	7.35	12.80	8.50	0.97	0.90	0.71
F97 P12	2/24/97	49.00	-130.7	60	8.57	8.77	6.31	0.81	1.17	0.75
F97 P12	2/25/97	49.00	-130.7	60	8.57	8.77	6.31	0.81	1.10	0.72
Sofex S55 1	1/12/02	-56.50	-172	90	5.54	3.81	22.57	1.47	2.32	0.87
Sofex S55 2*	1/18/02	-55.8	-171.9	90	5.97	3.73	22.37	1.54	3.00	2.22
Sofex S66 3	1/23/02	-66.40	-171.5	60	-1.01	64.81	28.45	1.91	1.45	1.08
Sofex S66 4	1/27/02	-66.47	-171.9	60	-1.00	64.81	28.49	1.90	1.13	0.86
Sofex S66 6	2/2/02	-66.37	-171.73	60	-0.73	62.89	28.94	1.90	1.07	0.91
Sofex S66 7	2/4/02	-66.20	-172.03	45	-0.75	62.91	28.81	1.90	1.31	0.80
Sofex S55 8	2/9/02	-54.21	-169.24	60	7.52	1.06	19.74	1.30	1.32	1.26
Aloha	6/25/04	22.77	-158	125	24.20	1.00	0.19	0.05	0.09	0.002
K2	8/1/05	47.00	161	50	9.35	19.49	14.00	1.27	1.16	1.20
Bats	7/2/08	31.78	-64.1	125	20.06	0.00	0.00	0.04	0.11	0.16
Slope*	7/10/08	37.02	-74.41	65					0.40	0.24
Safe	5/14/09	30.00	-141	150	17.58	1.52	3.06	0.12	0.13	0.17
SBB*	5/26/09	34.27	-120.04	25					1.13	0.26

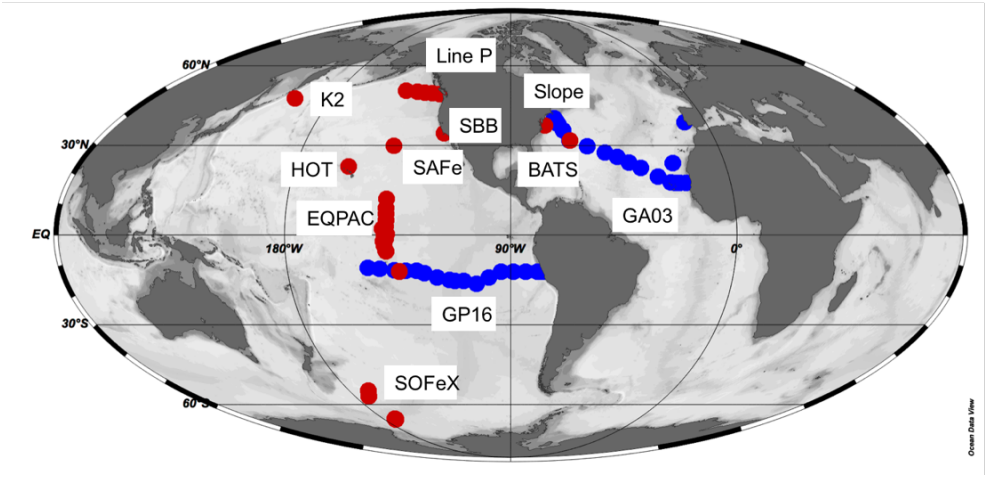

Figure 2.1: Map of sampling locations. MULVFS profiles are marked in red. GEOTRACES transects GA03 and GP16 (McLane samples) are marked in blue.

2.1.3 Study Areas

MULVFS samples originating from 11 sampling campaigns are described below in chronological order of their collection Figure 2.1.

The Equatorial Pacific Process Study (EqPac) of the Joint Global Ocean Flux Study Program (JGOFS) from 12 °N to 12 °S made 21 MULVFS casts during February and August 1992 Figure 2.1. The EqPac Survey I (TT007) and II (TT011) cruises captured the extremes of the 1991-1992 El Nino. Survey I samples were collected during the strong El Nino (in February of 1992), and Survey II samples were collected six months later during "normal" conditions (in August of 1992).

As part of the Canadian JGOFS, there were four MULVFS transects in the subarctic North Pacific from the continental slope off Vancouver Island to Ocean Station PAPA (OSP). In total, 20 MULVFS profiles were collected along Line P in February/March, June and August 1996 and in May 1997 [Bishop et al., 1999]. OSP (50 °N, 145 °W) has been a regularly monitored site since 1956 [Freeland, 2007].

The MULVFS was deployed during the 2001 Southern Ocean Iron Fertilization Experiment (SOFeX) [Lam and Bishop, 2007]. Particle samples were collected both north and south of the Antarctic Polar Front (APF), at 55 °S and 66 °S, respectively. At both locations, casts were taken prior to the addition of iron and several days subsequent to iron fertilization within the iron-fertilized patch. Control casts were also taken after fertilization from outside the iron-fertilized patch. During the Vertical Flux in the Global Ocean (VERTIGO) project, four profiles each were collected at station ALOHA (22.75 °N 158 °E), an oligotrophic station near Hawaii in June-July 2004 and at station K2 (47 °N 161 °E), a biologically productive area in the Oyashio current, in July- August of 2005.

During the first GEOTRACES inter-calibration cruise in June-July 2008, four MULVFS profiles were collected near the Bermuda Atlantic Time Series station (BATS 31.78 °N 64.1 °W) in the oligotrophic Sargasso Sea and two profiles were made at a station in the Slope Water (37.02 °N 74.41 °W) in mesotrophic waters 30 kms to the west of the north wall of the Gulf Stream.

During the second GEOTRACES inter-calibration cruise in May 2009, four profiles were taken at the SAFe site (37.02 °N 74.41°W) located at the edge of the oligotrophic North Pacific subtropical gyre. Two profiles were taken in the Santa Barbara Basin (34.27 °N 120.04 °W), a productive regime with a strong subsurface zone of oxygen deficient water. Particulate Cd and P measured independently on two GEOTRACES transects is then used to compare to predictions made using our MULFVS data. The two GEOTRACES transects utilized McLane pumps modified with MULVFS-style filter holders [Bishop et al., 2012]. The Atlantic cruises (GA03) were collected in October/November 2010 and November/December 2011. The South Pacific cruise (GP16) was collected in November/December 2013.

2.2 Methods

2.2.1 Particulate Sampling and Analysis

The particle profiles presented in this paper were collected using the MULVFS [Bishop and Wood, 2008; Bishop et al., 2012]. Briefly, the MULVFS uses a ship's electricity to power 12 pumps deployed along a 1000m long electromechanical cable. Action of the pumps draws water through a filter series. The standard MULVFS filter suite consists of a 51 µm polyester mesh prefilter that is supported by a 150 µm polyester mesh, followed by two (paired) Whatman QMA quartz fiber filters which are also supported by a 150 µm polyester mesh [Bishop and Wood, 2008]. The three resultant size fractions from this filter suite are >51 µm, 1-51 µm and <1 µm. The <1 µm fraction represents particles greater than 0.8 µm, in size [Bishop et al., 2012]. McLane pumps, which were used during the GEOTRACES transects GA03 and GP16, were modified according to Bishop, Lam and Wood [2012] and captured >51 µm and 0.8-51 µm size fractions. The McLane 0.8-51 µm samples are measured on Supor filters, not QMA. The sum of 1-51 and <1 µm fractions from MULVFS closely mimics the 0.8-51 µm samples from the McLane pumps [Bishop et al., 2012].

Immediately after recovery of the MULVFS pumps from the ocean, a portion of the 1-51 µm and <1 µm QMA filters were misted with Milli Q water to aid our analyses by removing some of the salt. It was known that treatment of samples with distilled water can cause a loss of P and possibly Cd from our samples [Collier and Edmond, 1984]. During the GEOTRACES 2009 intercalibration cruise, a portion of the QMA filters from each fresh sample was protected from misting using acrylic tubes to investigate the loss of labile elements. We sampled from both misted and un-misted areas of the filter from two MULVFS casts from the SAFe site.

The 1-51 and <1 µm QMA filters were sampled using sharpened acrylic tubes and/or stainless-steel biopsy punches. The >51 µm samples were scalpel cut using an acrylic template. Filter subsamples were then leached for 16 hours in 10 mL 0.6N HCl solution at 60řC. After leaching, the solution was filtered and diluted 5-fold with Milli Q water then further diluted with 1% HCl and spiked with 25 ppb In before being analyzed. We used a Thermo Instruments Element II magnetic sector Inductively Coupled Plasma Mass Spectrometer (ICP-MS) at Lawrence Berkeley National Laboratory (LBNL) for the majority of the samples; samples from EqPac cruises were analyzed using a VG Plasmaquad II ICPMS. All analyses followed the same protocol described in detail by Bishop and Wood [2008]. Samples were run in batches of about 70 samples per run including standards and blanks. In each run, samples were run in replicate along with several samples from previous runs. Run-to-run variability, uncertainty in blank corrections, and instrument reproducibility are included in our analysis of errors. Samples exposed at depth during MULVFS casts, but not used during filtration, were used as process blanks.

The particulate elemental concentrations in each of the three size fractions were derived by multiplying solution concentrations by the ratio of total filter area to subsample area, subtracting filter blank, and dividing by the volume of water filtered. The Cd, P, and Cd:P ratio at each sample depth was calculated, and results integrated through the euphotic zone at each site to arrive at a depth integrated average. As there was typically not a particle sample taken directly at the euphotic zone depth, values were calculated for those depths by linearly interpolating between surrounding samples.

Misting Experiment

No statistically significant loss or gain of Cd was found in the comparison of rinsed vs. unrinsed filters collected at the SAFe station during the GEOTRACES Intercalibration Cruise II Figure 2.2. In contrast, particulate P showed a small but statistically significant 7% loss between the misted and unmisted regions of the filter. As all MULVFS samples in this study were misted, this 7% difference does not affect the systematic comparison of P concentrations. The ratios of Cd:P in our MULVFS samples as well as the misted GA03 McLane samples will differ from reality by 7%, therefore reported values in Table 2.1 have been multiplied by 1.07 to account for this effect. Most GEOTRACES data collected from GP16 with the McLane pumps were not treated with distilled water, thus those samples are not adjusted in any way.

2.2.2 Environmental Data

Euphotic zone depth, Z, the depth where PAR is 1% of its surface value, was calculated from surface irradiance, I_o, using the following:

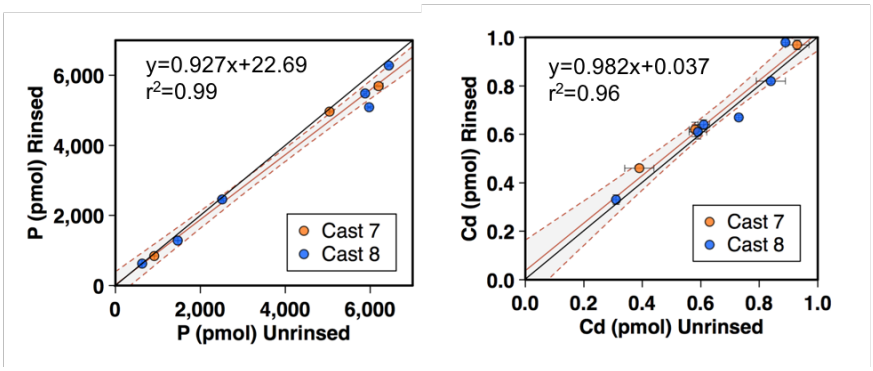

Figure 2.2: Comparison of rinsed (y-axes) and unrinsed (x-axes) P (left) and Cd (right) concentrations from combined 1-51 µm and <1 µm size-fractions taken at the SAFe site. Gray shading within the dashed lines represents 95% confidence interval of a single linear regression (solid orange line). Black line is the 1:1 line. Regression for P is significantly different from the 1:1 line and shows about a 7% loss of P in rinsed samples. Regression for Cd is not statistically different from 1:1 line.

$$Z = \frac{\ln(\frac{I_Z}{I_O})}{-K_{PAR}} \tag{2.1}$$

Where Z is depth at which PAR is 1%, Iz irradiance at depth Z, Io is irradiance at the surface and kPAR is the diffuse attenuation coefficient for PAR. Where PAR was not measured, we used the formula,

$$K_{PAR} = 0.027 + C_p 0.27 \tag{2.2}$$

where cp is beam attenuation coefficient derived from transmission at 660 nm [Bishop and Wood, 2009].

Dissolved phosphate, nitrate and silicate as well as temperature for each site were downloaded from the BCO-DMO database or obtained from unpublished cruise records. Average nutrient concentrations and temperatures were calculated by integration for the euphotic zone at each site. StatPlus software package was used to perform multiple linear regression analysis of the relationships between particulate Cd:P content with latitude, euphotic zone

depth, and water column euphotic zone nutrients (phosphate, nitrate, and silicate) and temperature averages. Derived simple empirical equations were used to map first-order global patterns of surface particulate Cd:P.

To create the global maps of predicted Cd:P, global profiles of objectively analyzed mean values for seasonal temperature, silicate, phosphate and nitrate data were downloaded from the World Ocean Atlas V2 2013 in a 1°latitude/longitude grid (https://www.nodc.noaa.gov). A global 1°by 1°seasonal climatology of euphotic zone depth was derived from the 9 km resolution MODIS Aqua satellite data product. In our final calculation, each grid location was used only if data for all variables was available. Our map covers approximately 90% of the ocean area (3.33×10^8 km^2 for the spring map; with area varying seasonally). The 10% loss is due to the unavailability of data in high-latitude regions in certain seasons due to seasonal ice cover and low sunlight.

2.3 Results and Discussion

Particulate Cd:P ratios spanned three orders of magnitude, from 0.01 to >2 mmol/mol, in all size fractions. There was great variability both seasonally and spatially. In order to better understand the causes of this large variability, we examine environmental conditions at each site and the potential relationship between these conditions and Cd:P. After analyzing variability in individual regions, we then examine the dataset as a whole using multiple linear regression to see if we can explain local trends as part of a predictable global pattern.

2.3.1 Oligotrophic vs. HNLC Cd dynamics

One of the most striking findings from the 50 locations is a marked distinction among oligotrophic, HNLC, and nutrient-replete environments. Figure 2.3 shows representative profiles from oligotrophic waters near Bermuda (Figure 2.3(a)), HNLC Southern Ocean waters at 55 °S (Figure 2.3(b)), and nutrient replete waters of the Santa Barbara Basin (Figure 2.3(c)). Both particulate Cd and P have typical nutrient-like particle profiles in that they are relatively high at the surface where they are taken up by phytoplankton, increase towards the chlorophyll maximum and then decrease below the euphotic zone as particles are remineralized.

The 1-51 µm particulates constitute the largest amount of material of the three size fractions and consequently this size fraction typically has the highest concentrations of both Cd and P Figure 2.3. In both the HNLC and oligotrophic profiles (Figure 2.3(b) and 2.3(c)), Cd:P is lower in the >51 µm size fraction than in the smaller size fractions. When comparing the average euphotic zone Cd:P values for the >51 µm versus the <51 µm size fractions using a paired t-test, there is a significant difference between the two groups (p=0.015). The mean Cd:P of the large size fraction is 0.2 less than the mean of the smaller particles. We focus on the <51 µm fraction due to it's dominance by phytoplankton.

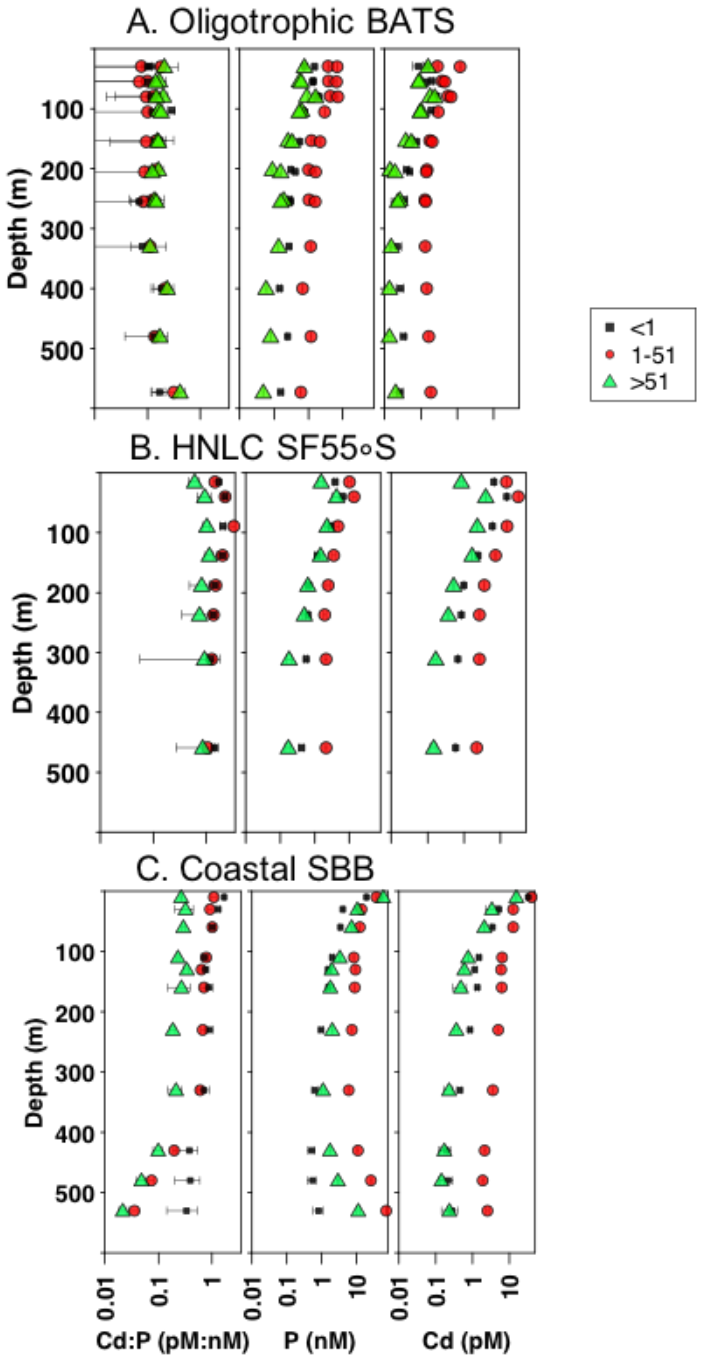

Figure 2.3: Particulate Cd:P, Cd, and P profiles from (a) the oligotrophic BATS site as part of the GEOTRACES Intercalibration I cruise, (b) 55 °S in an HNLC region during the SOFEX cruise, and (c) the Santa Barbara Basin as part of the GEOTRACES Intercalibration II cruise, where symbols show 3 size fractions: >51 µm (green triangles), 1-51 µm (red circles) and <1 µm (black squares).

2.3.2 Remineralization of Cd vs. P

In many profiles of Cd:P ratios from open ocean upwelling environments, there is a relatively shallow subsurface maximum in Cd:P at or just below the base of the euphotic zone, seen in the compilation of profiles in Figure 2.4. The particulate Cd and P peaks are shallower than the Cd:P peak as seen in figure 5. The maximum concentrations of both elements are always found in the euphotic zone. Near the euphotic zone base, particulate P concentrations decrease rapidly (Figure 2.5). Concentrations of Cd also decrease with depth, but at a much slower rate than P. We hypothesize that this is the result of processes that preferentially remineralize P in waters shallower than 150 m. This would agree with our misted versus non-misted experiments where there was no significant loss of Cd from shallow samples when filters were lightly misted, but there was about a 7% loss of P. It is notable however that Cd:P decreases in waters below the Cd:P maximum implying that in the mesopelagic zone, the remaining P is less labile than Cd. This trend is seen in profiles at HNLC areas throughout the worlds ocean (Figure 2.5).

Intracellular Cd is typically bound in 4S-coordination sites in stable tetrahedral formation, such as in metallothionein and phytochelatins, which are both thought to prevent metal toxicity [Cox, 2011; Cox and Saito, 2013]. Although the function of metallothionein is still not definitively known, it may be used as an antioxidant to scavenge oxygen radicals, as a metal resistance protein for detoxifying Zn, Cd and Cu, or for storage of excess Zn and Cu [Palmiter, 1998; Cox and Saito, 2013].

Phosphorous is located in ATP, DNA, phospholipid membranes and others. We hypothesize that the more labile portion of bound P, such as that bound in ATP and DNA, is remineralized faster than Cd at shallow depths. The lability of Cd, we hypothesize, lies between that of the labile P and the more refractory P pool (such as phospholipids). The maximum in the Cd:P profiles, frequently observed at the base of the euphotic zone, is consistent with remineralization differences in Cd vs. P in the water column (Figure 2.5). Differences in the remineralization rates of Cd and P could be a factor contributing to low dissolved Cd:P near the surface, and high dissolved ratios at depth in HNLC regions.

CdS crystals have been hypothesized to form in euxinic microenvironments in large aggregates as they sink due to rapid respiration rates within the aggregates [Janssen et al., 2014]; these CdS particles are delivered to the small particle fraction as aggregates are broken up. Ratios of Cd:P in our profiles peak in highly oxygenated productive surface waters of the upper 100m (Figure 2.5). Furthermore, dissolved oxygen begins to rapidly decline below the Cd:P particle peak. It is therefore unlikely that the precipitation of CdS crystals in euxinic microenvironments leads to these particulate Cd:P enrichments. If the Cd:P peaks were caused by authigenic formation of CdS, we would expect the gradient of oxygen loss to correspond with the particle Cd increase. No hints of this process are seen in the $>51\,\mu m$ fraction (Figure 2.3). We believe the peak Cd:P in our profiles is caused by differences in remineralization rates of Cd vs. P rather than formation of CdS (M5).

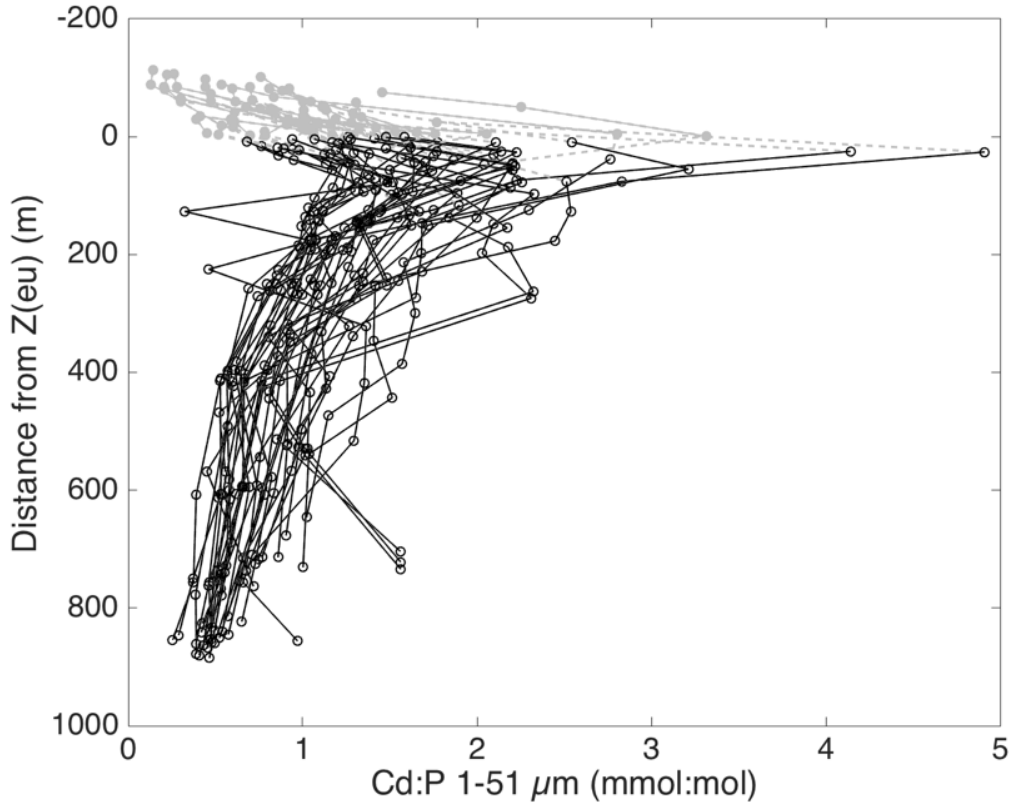

Figure 2.4: Overlay of all open ocean upwelling MULVFS 1-51 µm size fraction profiles to show trend of subsurface peaks (excludes oligotrophic sites SAFe, ALOHA and BATS as well as the coastal anoxic Santa Barbara Basin which show different trends). Each profile offset so that base of the euphotic zone is at 0m. Symbols show Cd:P measurements made in the euphotic zone (light gray markers) and below the euphotic zone (black markers).

2.3.3 Seasonal Changes

Of the 50 sites examined here, the majority of the casts come from two regions: the equatorial Pacific (21 casts) and the North-East Pacific (17 casts). These samples permitted an investigation into the effects of seasonality.

Line P

Between March 1996 and May 1997, the MULVFS was deployed during four expeditions along the Line P transect. The Line P transect runs from the coast of southern Vancouver Island out to ocean station PAPA (OSP: 50 °N, 145 °W). Macronutrient levels are never limiting along line P [Whitney and Freeland, 1999]. Station 4 (48.7 °N, 126.7 °W) is in an Fe

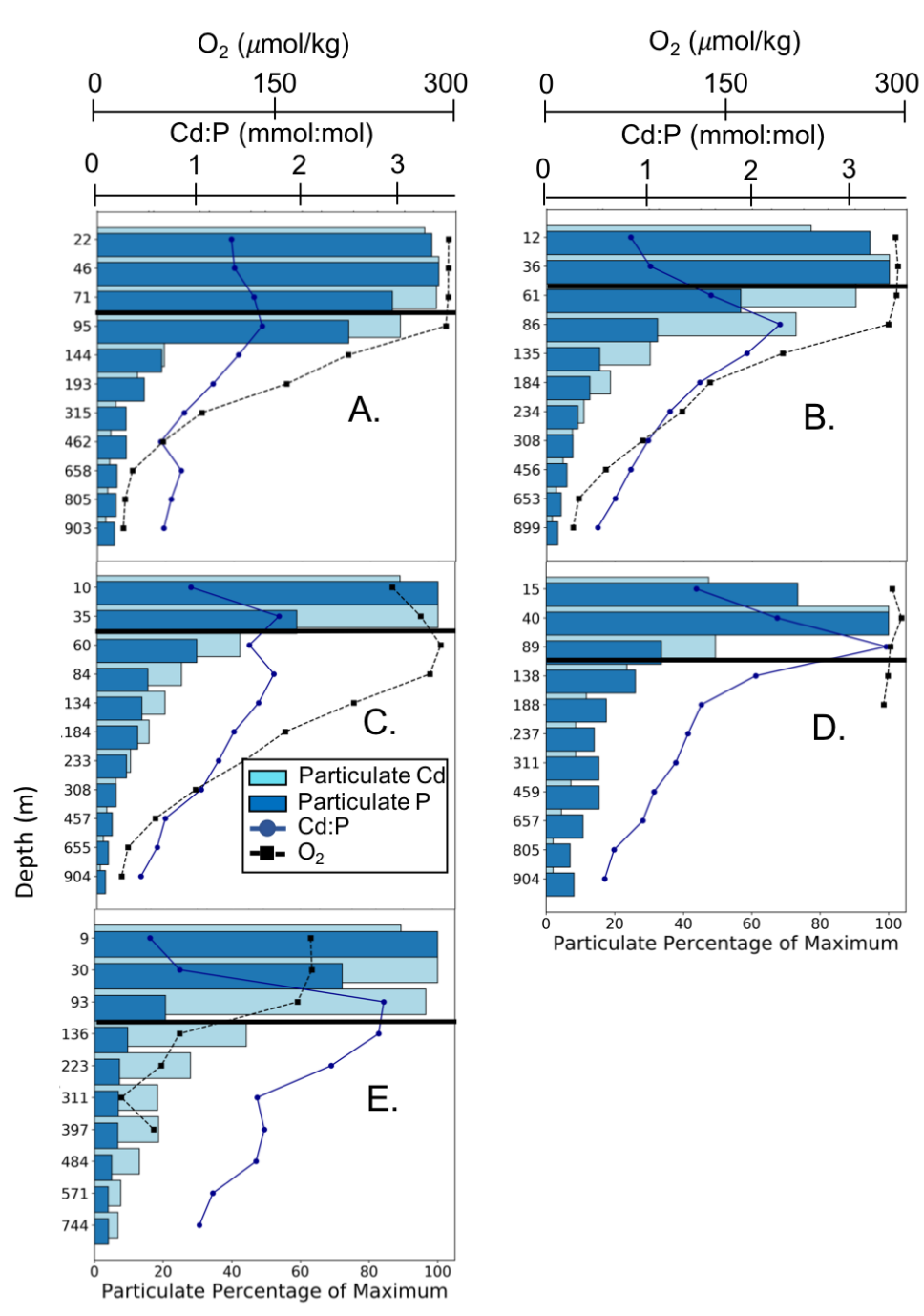

Figure 2.5: Particulate Cd (light blue bars) and P (dark blue bars) in the 1-51 µm size fraction normalized to profile-maximum values (bottom axis). Connected dashed black lines with black squares: dissolved oxygen (top/upper axis). Connected blue dotted lines: Cd:P ratio in the 1-51 µm size fraction (top/lower axis). Data above thick black lines are in the euphotic zones; data below line is below euphotic zone. Data are from Ocean Station Papa on March 3, 1996 (a), May 26, 1996 (b) and August 29, 1996 (c), SOFeX at 56.5 °S, 172 °W on January 12, 2002 (d) and 2.1°N, 141 °W on August 26, 1992 (e).

replete coastal region while Station PAPA is typically an HNLC region as levels of dissolved iron along Line P generally decrease from the coast out to Station PAPA. Dissolved Zn levels also decrease along the line and are extremely low at OSP [Lohan et al., 2002, 2005].

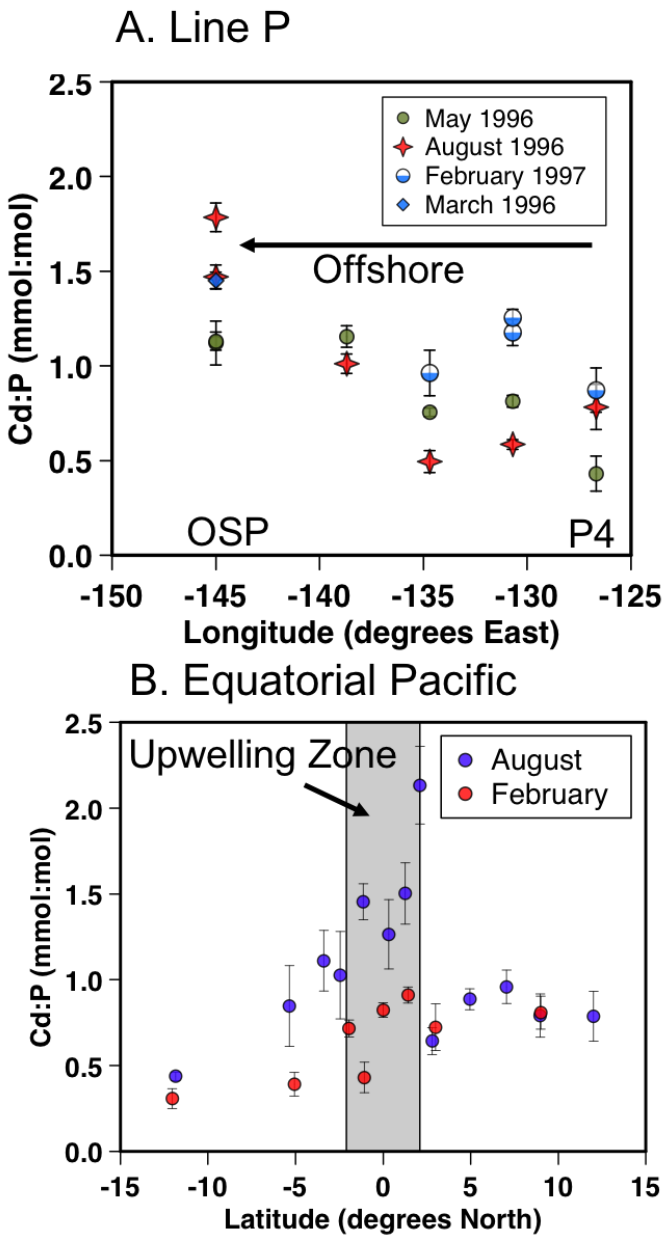

Figure 2.6: (a) Euphotic zone average Cd: P values in the combined <1 and the 1-51 µm size fractions along line P transect during the four cruises. Different shapes represent the different seasons. During the May and August 1996 cruises, day and night profiles were taken at OSP [Bishop et al., 1999].

Throughout this one-year time span, particulate Cd relative to P in the combined <1 and 1-51 µm size-fraction varied by a factor of two at individual sites and by a factor of three across the transect (Figure 2.6). In general, particulate Cd:P ratios increase with distance from shore, as conditions become progressively more micronutrient limited. In Fe-replete conditions closer to the coast, mean Cd:P of particles is lower. This trend supports the theory that Cd:P tends to be higher in HNLC regions due to either biodilution (M3) or by passive uptake along with other divalent metals (M1). At the time of the first MULVFS Line P cruise in February/March 1996, an iron-stimulated bloom was present at OSP. This iron likely originated from the continental margin off the Aleutian Islands [Lam and Bishop, 2008]. Diatoms Fragilariopsis sp. and Chaetoceros sp., dominated the large size fraction during the February/March bloom and coccolithophores dominated the 1-51 µm fraction [Lam et al., 2006].

Coccolithophore (E. huxleyi) concentrations were insignificant in May [Lam et al., 2006]. The February/March particulate organic carbon levels integrated to 100 m were twice as high in February/March than in May, though the surface POC levels were similar. Integrated chlorophyll levels were also twice as high in February/March than in May [Lam et al., 2006]. Lam hypothesized that more bioavailable iron reached OSP in February/March than in May because the isopycnal tagged with Fe supplied from the continental shelf had outcropped at the surface early in the year and was isolated by stratification later [Lam et al., 2006]. Si levels in the >51 µm fraction, from diatoms, were three times as high in March 1996 (0.22 µM) than in May and twice as high as in August.

The highest euphotic particulate Cd:P of the Line P dataset is from OSP during August 1996 (Figure 2.6), followed closely by OSP during Feb./March 1996. Though the Cd:P is very close at these two times, the environmental conditions were very different. During Feb/Mar cruise the mixed layer and euphotic zone were approximately the same depth; during the August cruise both the mixed layer (24 m) and euphotic layer (40 m) were far shallower than the isopycnal carrying the iron. The levels of bioavailable iron present in the euphotic zone were thus likely far lower during the August cruise than during the Feb./March cruise [Lam et al., 2006].

The variation in depth-integrated average euphotic Cd:P throughout these locations over three seasons is consistent with variation due to the following mechanisms: biodilution (M3), dissolved divalent metal availability leading to either specific or non-specific uptake of Cd (M1 and M2) or community composition (M4).

Equatorial Pacific

The two US-JGOFS Equatorial Pacific cruises in February and August 1992 allowed for the comparison of the chemistry of euphotic zone particulates during conditions of suppressed

upwelling caused by an El Nino with that of normal equatorial upwelling conditions. The upwelling equatorial region is an HNLC region; two of the possible hypotheses for the low phytoplankton stocks are iron limitation and microzooplankton grazing [Chavez and Barber, 1987]. During the February-March cruise, water temperatures were warmer and dissolved nutrients were lower; there was evidence of growth limitation. The SST recorded during Survey I and II were the warmest and coldest respectively of the JGOFS record at the time [Archer et al., 1996]. The mean SST between 10 °N and 10 °S was about 2 degrees warmer during Survey I than Survey II [Archer et al, 1996]. The equatorial upwelling zone is defined to be between 2 °N-2 °S [Murray and Leinen, 1996; Dunne et al., 1999].

The euphotic zone particulate Cd:P in the equatorial upwelling zone during the August cruise is significantly higher (1.1 mmol:mol) than observed during the El Nino period (0.55 mmol:mol) ($p=0.006$). The highest particulate Cd:P ratio(1.99 mmol:mol), was at the 2 °N site during the August cruise Figure 2.6. This station was taken in a strong frontal feature visible from space designated "the line in the sea", which was a highly productive ocean front region [Yoder et al., 1994] associated with high abundances of the diatom Rhizosolenia [Yoder et al., 1994].

The observed Cd:P difference could be due to the different phytoplankton communities (M4) present during the two cruises. Very small-celled organisms, Prochlorococcus and Synechococcus, were dominant during the El Nino cruise, while diatoms were dominant during the second cruise. Diatoms are typically more sensitive to iron levels than pico- and nano-plankton [Landry et al., 1995]. As noted above, cyanobacteria, such as Synechococcus and Prochlorococcus, have been shown to have a lower Zn content than other phytoplankton, and an extreme Cd sensitivity [Saito et al., 2003; Robbins et al., 2013]. Finkel [2007] found that when grown under nutrient replete conditions, cyanobacteria have a lower Cd:P ratio than diatoms, dinoflagellates, green algae and coccolithophorids. Cd:P of our particle samples was lower during the Feb.-March cruise when cyanobacteria were dominant than the August-Sept. cruise when diatoms were dominant which is consistent with the species differences mechanism (M4) leading to differences in Cd:P uptake.

Under typical conditions, the Equatorial Pacific upwelling region is growth-limited by Fe and is classified as an HNLC region as there are excess macronutrients available. During El Nino conditions, when upwelling is suppressed, the region becomes more oligotrophic. The 2x-elevated Cd:P ratios observed during the regular upwelling season as opposed to the El Nino conditions could therefore also be explained as an effect of biodilution in an HNLC area (M3), preferential fractionation of Cd from high dissolved Cd:P of upwelled intermediate water leading to higher particle Cd:P (M6) or low concentrations of other divalent metals leading to an upregulation of Cd uptake (M1 and M2).

2.3.4 Southern Ocean

During the Southern Ocean Iron Fertilization Experiment, MULVFS casts were collected north and south of the Antarctic Polar Front (APF), both before and following iron fertilization experiments. Both locations were iron limited; north of the APF, diatom growth was believed to be limited by silicate as concentrations (1-5 µM) were significantly lower than the levels south of the APF (>60 µM) [Coale et al., 2004]. Both sites had 20 µM nitrate concentrations. Because of the silicate differences, it was hypothesized that added iron would stimulate diatoms to bloom at the 66 °S site while non-siliceous organisms would bloom at the 55 °S site [Coale et al., 2004]. Diatoms dominated waters at the 66 °S site. At 55 °S, there was a more diverse phytoplankton community with dinoflagellates and coccolithophores. Though silicate levels were low here, they were high enough to also support diatoms [Lam and Bishop, 2007]. The Southern Ocean, both north and south of the APF is an HNLC environment.

Southern Ocean euphotic zone particulate Cd:P exceeded 1 mmol:mol both north and south of the APF (table 2.1). The high Cd:P in the HNLC environments both north and south of the APF could, as in the case of OSP and the upwelling equatorial Pacific HNLC regions, be due to biodilution (M3) or low concentrations of divalent metals leading to an upregulation of Cd either specifically targeted or taken up obligatorily (M1 and M2).

The highest particulate Cd:P was at 55 °S, north of the APF. This was true for both the >51 µm and <51 µm size fractions (table 2.1). Along with dissolved Si concentrations, Zn concentrations are typically higher south of the polar front. In a Southern Ocean cruise in 2008, Croot et al. [2011] found that Zn concentrations in the upper 200m South of the APF were always greater than 1 nM whereas the lowest Zn concentration was found North of the APF (0.21 nM); they also found a significant correlation between Si and Zn. Low concentrations of dissolved Zn at the 55 °S site could lead to increased Cd uptake (M1).

Modeled dissolved Cd in the Southern Ocean increases across the polar front zone to higher latitudes [Roshan et al., 2017]. Actual dissolved Cd:P ratios in surface waters also similarly increase [Elderfield and Rickaby, 2000]. The fact that our particulate Cd:P concentrations peak at the 55 °S and decrease to 66 °S argues against Cd:P being purely driven by proportional uptake to dissolved Cd (M6). It is likely that in this location, the low concentrations of dissolved Zn North of the APF lead to higher particle Cd:P than South of the APF.

2.3.5 Global View

Cullen and Maldonado (2013) estimated surface particulate Cd:P based on analysis of the gradient of dissolved Cd and P concentrations in the nutricline at the numerous locations where both elements have been measured. They predicted particulate Cd:P ratios ranging from 0.09 to 1.9 mmol/mol. In this case, they defined HNLC conditions as stations having an

annual average surface phosphate above 0.3 µM. Results gave particulate Cd:P in oligotropic and HNLC regions as 0.24 and 0.54 mmol/mol respectively. More recently, Quay et al. [2015] augmented these calculations with recent GEOTRACES and CLIVAR cruises yielding a revised particulate Cd:P for oligotrophic and HNLC regions of 0.21 ± 0.09 and 0.49 ± 0.23 mmol/mol, respectively.

In our particulate data, euphotic zone particles for the combined 1-51 and the <1 µm size fraction Cd:P ranged from 0.09 to 3.0 mmol:mol (table 2.1). The lowest ratio was found at oligotrophic station ALOHA (0.09) while the highest value was found in the Southern Ocean at 55 °S (3.0) in particles collected 6 days after the iron fertilization event. It must be noted that while collection for this cast began within the Fe fertilized patch, the ship drifted outside the fertilized region for much of the pumping, so this may represent an iron limited sample. The highest Cd:P ratio found in purely non-fertilized conditions was 2.32, also at 55 °S and the second highest in upwelling Equatorial Pacific waters at EP20 (2.00). In the >51 µm size fraction, the lowest Cd:P ratio was found at the oligotrophic station BATS (0.16) and the highest ratio was found at EP16 (3.61), and the second highest at 55 °S (2.22) in particles collected in 6-day old iron amended waters (table 2.1).

Particulate Cd:P for oligotrophic and HNCL regimes (following Cullen and Maldonado 2013) was 0.11 ± 0.02 (1 s.d.) and 0.98 ± 0.42, respectively. Only three of our stations had average euphotic zone phosphate concentrations less than 0.3 µM. The majority of our sites were therefore classified as not oligotrophic.

The two GEOTRACES cruises GA03 and GP16 in the North Atlantic and South Pacific, respectively, are used below as an independent point of comparison of our results and greatly expands the number of oligotrophic sites with Cd:P particulate data. The sites in the North Atlantic gyre had low surface Cd:P ratios compared to the South Pacific GP16 cruise (table 2.1). The North Atlantic transect had lower nitrate levels than the South Pacific transect which skirted the southern boundary of the Eastern Pacific equatorial upwelling region, consistent with the trend of lower Cd:P in oligotrophic regions (M3). Further, the North Atlantic transect had higher dissolved Zn and Mn levels than the South Pacific transect [Hatta et al., 2014, Resing et al., 2015]. If Zn and Mn share a divalent metal transporter with Cd, the higher levels of Zn and Mn in the North Atlantic could therefore have suppressed the uptake of Cd (M1), explaining the lower Cd:P.

2.3.6 Linear and Multiple Linear Regressions

Linear regressions were calculated using Cd:P ratios using the combined <1 and 1-51 51 µm MULFVS fractions. Cd:P was scaled to correct for the 7% phosporus loss from misting as described in section 2. All data used in the regression are shown in Table 2.1. The euphotic depth used for each sample is the depth where PAR is 1% of the surface value during the day of sampling. With each variable treated independently, the most significant relationship was between particulate Cd:P and euphotic zone phosphate (p=2.19E-6,

r^2=0.38), closely followed by Cd:P and euphotic zone nitrate (p=3.60E-6, r^2=0.36). Relationships between particulate Cd:P and euphotic zone temperature (p=0.00188, r^2=0.17), euphotic zone depth (p=0.01624, r^2=0.10) and euphotic zone silicate (p= 0.0233, r^2=0.09) were also significant.

Multiple linear regressions were calculated with Cd:P ratio from the MULVFS dataset as the independent variable and the hydrographic and nutrient data as independent variables. By comparing the adjusted r^2 values of different variable combinations, we found the best prediction of Cd:P variation:

$$Cd : P = 0.8917 - (0.0041 * Z_{(eu)}) - (0.0216 * Si_{(eu)}) + (0.0703 * NO_{3(eu)}) \quad (2.3)$$

where eu denotes euphotic zone The adjusted r^2 for this equation was 0.56. The range of independent variables used in the MLR can be seen in Figure 2.7. The magnitude of the contribution of euphotic zone depth (depths ranged from 20-150 m; table 2.1) to Cd:P is -0.08 to -0.60; similarly contributions of Si (range 0-65 µM) are from 0 to -1.4. Both the increase of euphotic depth and Si concentrations lead to lower Cd:P ratios. In contrast, increases in NO3 (range 0-29 µM) leads to an increase in Cd:P, with a proportional contribution to Cd:P ratio ranging from 0 to 2.0.

Equation 1 was used to predict seasonal global euphotic zone particulate Cd:P using the 1°by 1°gridded euphotic zone depth, nitrate and silicate data (Sec. 2.2) and mapped in Figure 9. The 50 MULVFS data points are also overlain on the maps fore their respective seasons. We then compared our seasonal particulate predictions with independently collected particulate Cd:P data from GEOTRACES cruises which were not used in creating the multiple linear regression. Those data points are shown overlaying the global maps in Figure 2.9 (September, October, November panel). As mentioned above, the GEOTRACES 2013 transect (GP16) in the south-east Pacific and the 2010/2011 North Atlantic transect (GA03) (Fig. 1) were collected using McLane pumps [Ohnemus and Lam, 2015; Lee et al., in press]. Though the global map predicted general trends (Figure 2.9), there are some notable differences. For one, in the Autumn transect in the North Atlantic, all the McLane particulate data had lower Cd:P values than the map based on Equation 1. One reason for the data-model difference is that we had far more nutrient-replete stations than oligotrophic stations in our MULVFS dataset. To see if having more oligotrophic stations in our data would improve the Cd:P prediction for oligotrophic regions, we added in the sites from the North Atlantic GEOTRACES GA03 cruise and recalculated the regression. When these stations were added, the r^2 of the model increased to 0.59 with the new model better capturing Cd:P ratios in oligotrophic environments (Figure 2.8).

$$Cd : P = 0.7629 - (0.0041 * Z_{(eu)}) - (0.0192 * Si_{(eu)}) + (0.0722 * NO_{3(eu)}) \quad (2.4)$$

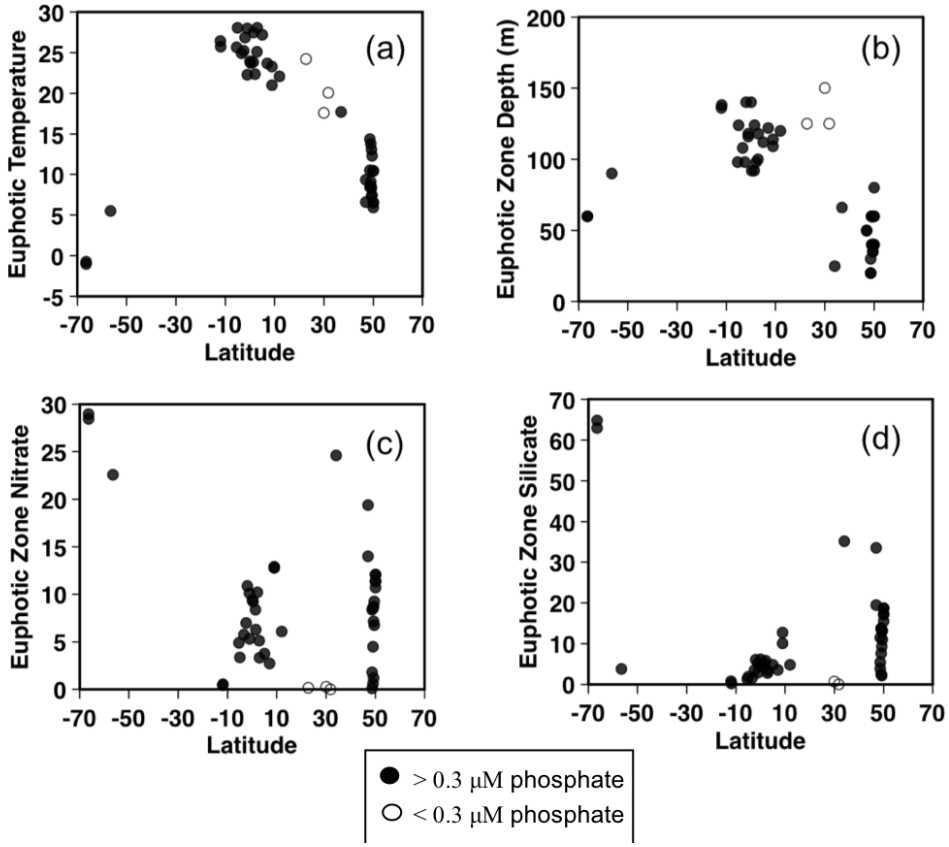

Figure 2.7: Average euphotic silicate (a), nitrate (b), temperature (c) and euphotic zone (d) depth vs. latitude at MULVFS sites. Open circles represent waters with < 0.3 µM surface dissolved phosphate; filled in circles >0.3 µM surface dissolved phosphate.

Inclusion of the GA03 results led to a 0.13 decrease of the intercept. Weighting for euphotic zone depth, Si, and NO3 was changed slightly. Statistics for equation 1 and 2 are shown in Table 2 and regression shown in Figure 2.8.

We note that there will be some departure of our instantaneous observations compared to decadal averaged fields used for the maps. For example, effects of ENSO are averaged in WOA13 V2 data but seen in our results.

2.3.7 Why do hydrographic variables predict Cd:P?

Over the past four decades there have been a number of proposals to explain why Cd:P ratios vary in dissolved profiles throughout the oceans (Sec. 1.1). Using multiple linear regression techniques, we are able to describe 59% of the variance of Cd uptake of particles in the euphotic zone using variables that are known to be important parameters governing phytosynthesis such as dissolved nitrate, silicate and euphotic zone depth. Using these variables,

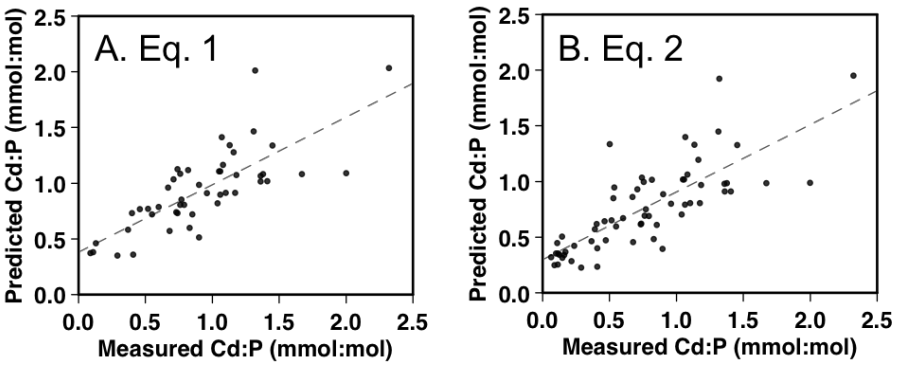

Figure 2.8: Regressions of actual to predicted euphotic zone Cd:P <51 µm particles for equation 1 (A) and equation 2 (B).

which are broadly available and have higher spatial and temporal resolution than particulate data, we are able to make predictions of how global particulate Cd:P varies spatially during different seasons. This exercise allows us to examine which of these parameters exert the greatest control on Cd uptake. Our statistical model used to predict Cd:P variation provides insights towards a mechanistic understanding of what processes cause this variation.

We found that the single strongest predictors of euphotic zone Cd:P were macronutrient nitrate and phosphate concentrations. In the MLR, higher nitrate concentrations drive higher particulate Cd:P ratios. High macronutrients are likely to indicate low Fe or another limiting trace metal which would support either biodilution (M3), dissolved divalent metal availability leading to passive or active uptake of Cd (M1 and M2). This finding supports previous field and lab studies that show variation of Cd uptake in phytoplankton with varying nutrient limitation.

In contrast, higher concentrations of dissolved Si drive particulate Cd:P lower. As Zn and Si are typically well correlated [Wyatt et al., 2014], Si may be a proxy for Zn. This supports the theory of dissolved divalent metal availability driving Cd:P differences (M1 and M2). Deeper euphotic zone depths led to lower Cd:P ratios in the MLR. Euphotic depths are typically deepest in oligotrophic gyres, which is where we found our lowest Cd:P ratios. Macronutrients are therefore proxies for trace element concentrations that affect two of the key hypotheses for regulation of particulate Cd:P: biodilution (M3) and dissolved divalent metal availability (M1 and M2).

2.4 Conclusions

Since the mid 1990s, it has been noted that there must be a mechanism that preferentially removes Cd relative to phosphate in the surface ocean [Boyle, 1988]. Evidence from our observations of particulate Cd and P concentrations in MULVFS profiles as well as from our misted vs. un-misted filter experiments support the hypothesis that P occurs in two forms with different labilities. One phase, for example, phosphorus bound in ATP and DNA, is more labile than Cd whereas the second phase, such as phosphorus in phospholipids, is less labile than Cd. The Cd:P exported out of the euphotic zone at these sites has a higher ratio due in part to these remineralization differences. This finding is consistent with a previous study by Waeles et al. [2016] who investigated the systematics of both dissolved and particulate Cd and P off the coast of Morocco. These differences in remineralization rates would be a factor contributing to low dissolved Cd:P at the surface and high dissolved Cd:P ratios at depth in HNLC regions. We hypothesize that it is these differences in remineralization rates, rather than formation of CdS, that lead to subsurface particulate Cd:P peaks.

We see seasonal and spatial variation over an order of magnitude in particulate Cd:P ratios. In previous studies, it has both been found and predicted that particles from HNLC regions would have higher Cd:P ratios [Cullen, 2006; Lane et al., 2009]. Cd:P in HNLC environments from our study also had a much higher Cd:P then particles from oligotrophic regions. Our data supports the mechanisms that under Fe limitation, slower growth rates can lead to higher Cd:P (M3) and that low concentrations of dissolved Fe, Zn and Mn can lead to increased uptake of Cd (M1 and M2). While M6 (the differential uptake of Cd and P driven by availability) would explain first order variations we observe, this mechanism does not hold in all locations, especially the Southern Ocean. We do not have associated dissolved trace metal data for Cd and other divalent metals such as Zn and Fe(II) at our stations. Future work examining the relationship between dissolved and particulate trace metal:P would allow for further insight into the roles of the six mechanisms.

Examining variation of these 50 casts has helped to better understand the range in particulate Cd:P both seasonally and spatially and form a predictive framework for further analysis and experimentation. This first global collection of euphotic zone Cd:P in particles follows trends predicted in previous studies and found in regionally localized studies. The contribution of this work is that we found direct links to parameters important to phytoplankton production (nitrate and silicate concentrations and euphotic zone depth) that can be used to predict broad patterns in Cd:P uptake. In understanding variation in the modern day, we can better understand what factors may have impacted Cd:P distribution in the past.

This chapter presented a method by which to predict Cd:P on widely available satellite and surface nutrient data. The next chapter focuses on developing a calibration for a robotic instrument with the ultimate goal of collecting high frequency flux measurements which can be used to inform global flux models.

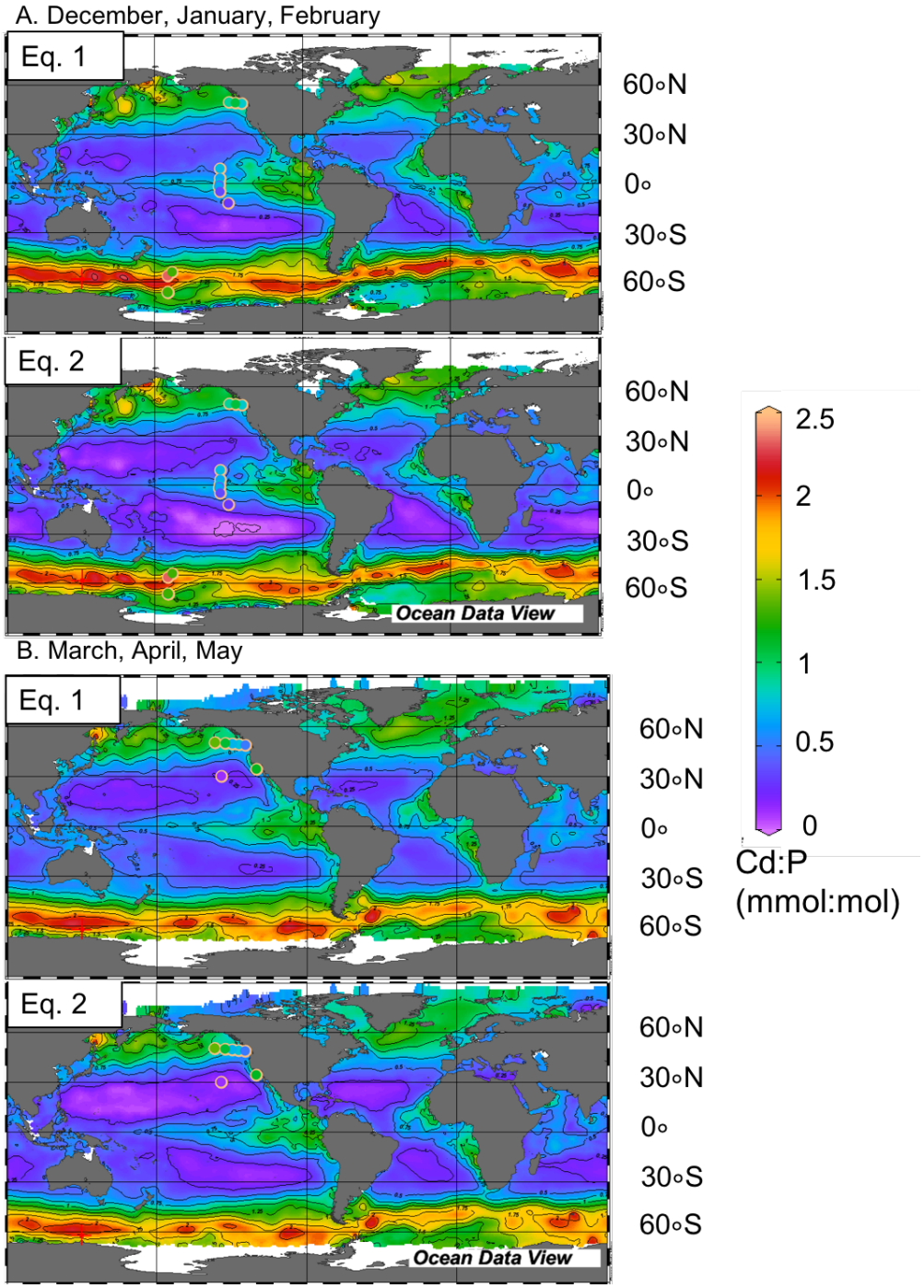

Figure 2.9: Seasonal euphotic zone predictions of particulate Cd: P from equations 1 and 2. The predicted maps are overlain with actual euphotic zone depth integrated average Cd: P data from the seasons they were collected during. The overlain data comes both from the MULVFS casts and the GEOTRACES McLane pump casts. The South Pacific transect in (D) is independent data not used in the creation of equation 1 or 2.

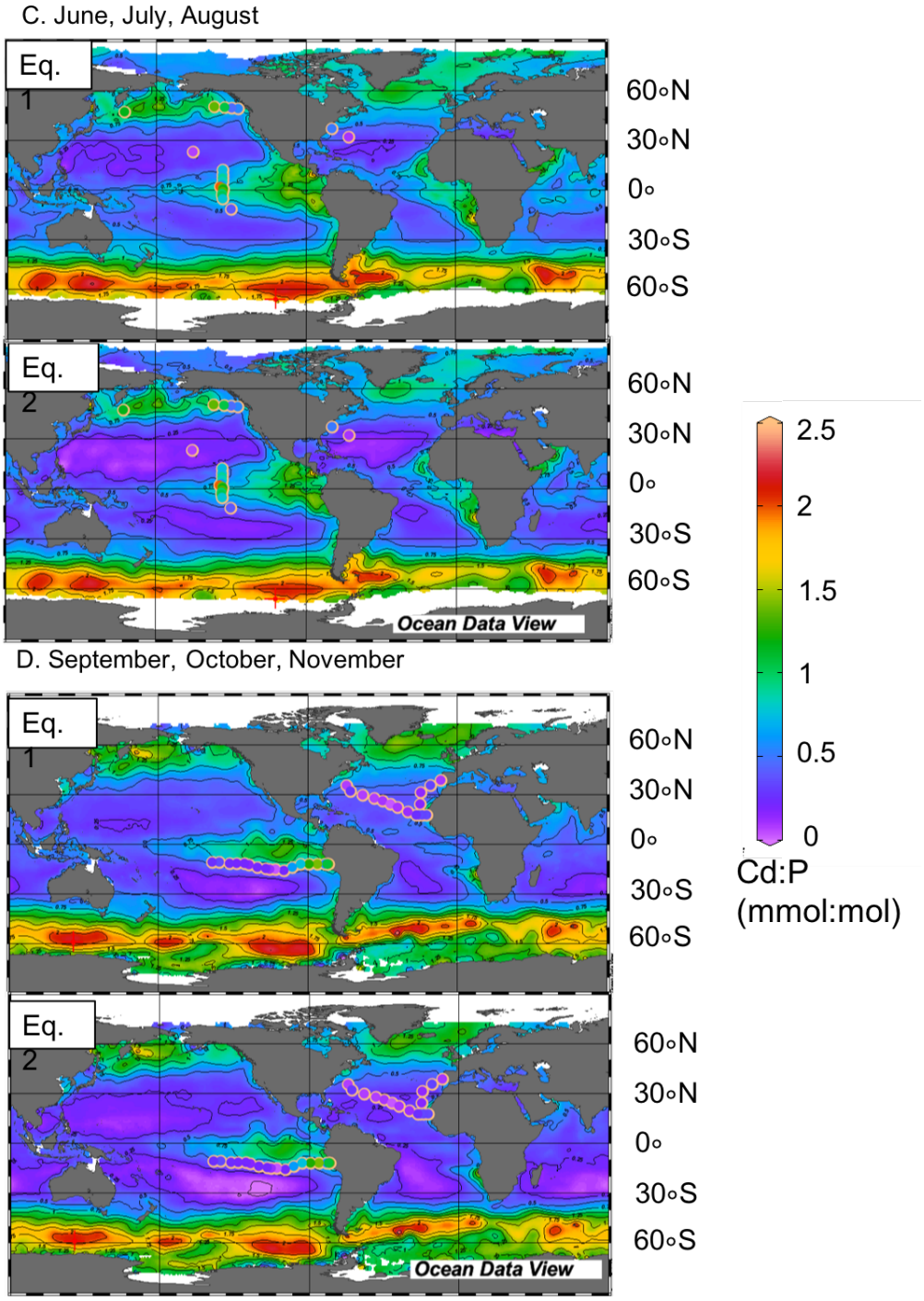

Figure 2.10: Seasonal euphotic zone predictions of particulate Cd: P from equations 1 and 2. The predicted maps are overlain with actual euphotic zone depth integrated average Cd: P data from the seasons they were collected during. The overlain data comes both from the MULVFS casts and the GEOTRACES McLane pump casts. The South Pacific transect in (D) is independent data not used in the creation of equation 1 or 2.

Chapter 3

Carbon Flux Explorer Optical Assessment of C, N and P Fluxes

3.1 Introduction

Marine phytoplankton account for about half (or 50 Pg C y^{-1}) of global primary productivity and live for one week on average before being consumed by zooplankton (Falkowski et al., 1998). Approximately 10 Pg C y^{-1} is exported from the surface layer as sinking aggregates containing both particulate organic and inorganic carbon (POC and PIC). The carbon that reaches the deep ocean remains isolated from the atmosphere for centuries. This process, the "biological carbon pump" (BCP), is a fundamental player in the global carbon cycle. The stability of the BCP and its future in the face of climate forced circulation changes and ocean acidification are currently unknown. A number of recent studies have noted discrepancies in reconciling meso- and bathypelagic activity with current euphotic zone flux estimates (Banse, 2013; Burd et al., 2010; Ebersbach et al., 2011; Passow, 2012; Stanley et al., 2012). Recent estimates of carbon flux out of the euphotic zone range from 6 to 12 Pg C y^{-1} (Dunne et al., 2005; Siegel et al., 2014; Yao and Schlitzer, 2013). More traditional methods of measuring particle flux in the ocean rely on sediment traps or geochemical sampling that require ship time (Buesseler et al., 2007). As ship time is expensive both in terms of funding and labor, flux measurements conducted this way are temporally and spatially limited. In recent years, there have been a number of developments towards autonomous instruments capable of measuring particle flux (Bishop et al., 2004, 2016; Briggs et al., 2011; Estapa et al., 2013, 2017).

The attenuation of light by particles has long been used by oceanographers as a measurement of particle concentration in the ocean water column, beginning with development of underwater transmissometers in the early 1970s (Zaneveld, 1973). Transmissometer beam attenuation coefficient (at 660 or 650 nm) has been shown to strongly correlate with measurements of particulate organic carbon (POC) concentration in the water column (Bishop et al., 1999; Bishop and Wood, 2008; Boss et al., 2015; Gardner et al., 2000). Transmissometers

were first deployed vertically mounted on Lagrangian profiling floats (called the Carbon Explorers, CEs) in 2001 in the North Pacific (Bishop et al., 2002). These deployments revealed a systematic loss of transmission as the CEs drifted at depth between profiles. A trend of increasing transmission was seen in the deepest 200-300 m as the float rose from 1000 m to the surface, implying that particles had accumulated on the upward looking transmissometer window during drift and were being washed off during initial stages of profiling. CE's deployed in the Southern Ocean in 2002 were modified to measure transmittance before and after exhaust flow from the float's CTD pump was used to clean particles off the transmissometer window during drift and thus a Carbon Flux Index (CFI) was derived as a systematic measure of particle flux over time (Bishop et al., 2004). Estapa et al. (2017) advanced the quantitative use of float-deployed transmissometers to estimate particulate carbon flux and more properly derived a flux proxy based on beam attenuance change over the 1-2 days that their neutrally buoyant traps drifted at depth. The Estapa et al. (2017) method does not involve optics flushing.

The Carbon Flux Explorer (CFE), which combines an imaging Optical Sedimentation Recorder (OSR) and profiling Sounding Ocean Lagrangian Observer (SOLO) float, periodically images particles as they accumulate on a glass sample stage. It thus builds upon the concept of optically measuring particle flux by quantifying particle attenuance at each pixel (Bishop et al., 2016; Bishop and Wood, 2009). The imaging instrument also fully resolves particle classes from 20 µm to cm scale. As transmissometer beam attenuation coefficient was found to be highly correlated to POC concentration, a reasonable assertion would be that light attenuance of particles integrated across an image (volume attenuance) would also be highly correlated to POC load. Image attenuance (ATN) is the combined effect of both light scattering loss and light absorption by particles. It is calculated by taking the $-\log_{10}$ of a transmitted light image normalized by an in-situ blank composite image of the particle free sample stage (Bishop et al., 2016). Integration of ATN across the sample stage area yields Volume Attenuance (VA, units: mATN-cm^2), a measure of particle load. Normalizing by trap opening and time deployed yields Volume Attenuance Flux (VAF, units: mATN-cm^2 cm^{-2} d^{-1}).

Successful calibration of VAF in carbon units would allow for far greater temporal, and spatial resolution of carbon export than possible with ships and thus inform current models of biological carbon flux as CFEs have the capability of observing hourly variation of particle flux at depth for months to seasons (Bishop et al., 2016). An earlier attempt to calibrate the CFE in 2013 used a surface tethered OSR and sampler (shown in Mcdonnell et al., 2015 Fig. 3F). This method failed as it was discovered that simultaneously deployed surface-tethered OSRs and Lagrangian CFEs collected far different particle types, size distributions, and quantities of material (Bishop et al., 2016). The surface-tethered OSR was biased low by as much as a factor of 20 and collected almost no material larger than 1.5 mm. These larger aggregates encounter the cm sized openings of the trap in a near horizontal trajectory and thus bounce back into the flow rather than accumulating in the trap. Lacking calibration

samples, Bishop et al. (2016) utilized aggregate size - POC weight estimates from Bishop et al. (1978) to derive a factor of 2.8 for scaling VAF (mATN-cm^2 cm^{-2} d^{-1}) to POC flux (mmol C m^{-2} d^{-1}); they note that applying the Alldredge (1998) volume-POC formula for marine snow particles collected by scuba in shallow waters yielded a conversion factor of 0.16, about 17 times smaller than the estimate based on Bishop et al. (1978).

Estapa et al. (2017), working in oligotrophic waters near Bermuda, compared sediment trap POC flux with transmissometer attenuance drift (at 650 nm); conversion of their results (Fig. 7 in Estapa et al., 2017) yielded factors ranging from 0.46 to 0.74 (in our units of VAF: POC), four to six times lower than the 2.8 conversion factor (a conversion error in Estapa et al., 2017 implied a greater difference). Multiple optical reasons for differences include: (1) beam collimation (CFE uses a diffuse LED light source and camera (Bishop et al. 2016) whereas transmissometers are highly collimated but can vary by a factor of two in sensitivity based on differences of beam geometry and receiver acceptance angle (Bishop and Wood, 2008; Estapa et al., 2017), (2) effects of particle size distribution on attenuance, (3) wavelength dependence of attenuance (CFE uses the green image plane (550 nm) vs. red transmissometer (650 nm)), and (4) stray light. Estapa assumed 100% collection efficiency of particles on the vertically facing transmissometer window and zero contribution of optics biofouling to her measurements. The difference in slopes may be also method dependent as Estapa et al. (2017) analyzed only the particulate carbon in 350 µm screened material from the neutrally buoyant sediment traps whereas the Bishop et al. (2016) factor includes larger aggregates up to cm size.

Given our finding of a factor of 20 under collection of samples by the surface-tethered OSR, a great uncertainty of literature-based calibration factors, the few environments sampled, and the multitude of lighting and methodological factors affecting the relationship of attenuance and carbon, we needed to develop a particle sampling device which could operate on the CFE. The new integrated system is referred to as "CFE-Cal" (Figure 3.1(a)).

Below we describe important design advances that led to the CFE-Cal and report first results from 2 CFE-Cals that were deployed and recovered 15 times at four locations during the June 2 to July 1 2018 California Current Ecosystem Long Term Ecological Research (CCE-LTER) process study cruise aboard R/V Revelle. The aim of the CCE-LTER expedition was to characterize food web processes and particle export at different places within and outside of an offshore-flowing phytoplankton-rich filament of upwelled water near Point Conception, CA (Figure 3.1(b)). The diverse environments sampled provided an excellent opportunity to collect a calibration sample dataset under high to low particle flux conditions.

3.2 Materials and Methods

3.2.1 CFE, CFE-Cal and Optical Attenuance

Bishop et al. (2016) describe in detail the CFE and the operation of its particle flux sensing OSR. These core elements are identical to those of the CFE-Cal. Briefly, once released

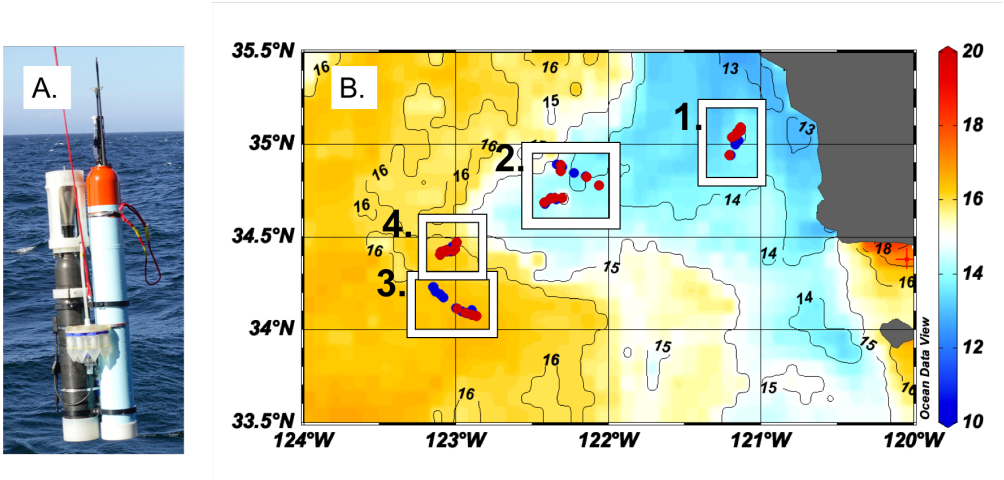

Figure 3.1: Left: CFE-Cal during deployment from R/V Revelle in 2017. The sampling system for particles is interfaced between the Optical Sedimentation Recorder (left) and SOLO float (right). Right: Map of CFE-Cal deployment and drift locations overlaying map of sea surface temperature. Sea surface temperature data averaged from June 10-17 from NASA Ocean Color Aqua Modis 4km resolution (https://oceancolor.gsfc.nasa.gov/). Blue dots within location boxes represent CFE-Cal 002 and red dots represent CFE-Cal 004 positions.

from the ship the CFE dives repeatedly below the surface to obtain OSR observations at up to three target depths as it drifts with currents. The CFE's OSR awakes when the target depth is reached. Particles settle through a hexagonal celled baffle (1 cm opening) into a high-aspect ratio funnel assembly before depositing on a 2.54 cm diameter glass sample stage. Particles are imaged at 13 µm pixel resolution in three lighting modes: transmitted, transmitted-cross polarized, and dark field. In this paper, we focus only on the calibration of POC sample loading vs. volume attenuance determined from transmitted light imagery.

On first wake-up of a given CFE dive, the sample stage is flushed with water and images of the particle-free stage are obtained. At timed intervals (25 min in data described here) the OSR repeats image sets, which register the sequential buildup of particles. After the predetermined number of image sets over 1.8 h, cleaning occurs and a new reference image set is obtained. After 5-6 h at a target depth, the OSR performs a final image set, cleaning cycle and reference image set, and the CFE surfaces to report GPS position, CTD profile data and OSR engineering data, and dives to its next target depth. All target depths in this study were chosen to be at 150 m. We describe in detail below the particle sampler and its integration with the CFE to form the CFE-Cal. In the case of the CFE-Cal, stage cleaning operations direct particles from each dive to a unique sample bottle.

Image attenuance was calculated following Bishop et al. (2016). Briefly, transmitted light images were normalized by a composite in-situ image of the particle free sample stage. The

-$\log_{10}$ of the normalized image was taken to yield ATN values. Pixels with a light attenuance value less than 0.02 were defined to be background. Pixels with attenuance values above 0.02, determined to be particles, were integrated across the sample stage then divided by total number of pixels in the sample stage area yield attenuance. This is multiplied by 1000 to yield mATN and then by the sample stage area to give sample Volume Attenuance (VA, units: mATN-cm^2). As light is reduced exponentially as it passes through particles, as long as the overlapping particles do not 100% obscure the transmitted light, attenuance affects are additive. In our analysis, the transmitted light even in the presence of multiple overlaid large aggregates, never went to zero (in other words, attenuance was never saturating). Therefore, overlapping particles is not an issue in this study.

Depth seeking performance of the CFE-Cal, imaging and sampling times, and derived VA time series are illustrated in Figure 3.2. In order to compare VA to filter loads of POC, PN and PP, the cumulative VA over the course of a dive had to be calculated. During a dive, particles are transferred from image stage to a specific sample bottle between 2 to 6 times. For each cleaning cycle, the VA of a clean image was subtracted from the image with particles prior to transfer to a bottle. This then represented the amount of material directed into the sample bottle after cleaning. VA from each cleaning step was then summed to yield a cumulative VA which should correspond exactly to the particles directed into the sample bottle.

3.2.2 Sampler

Most key components of the sampler for the CFE-Cal were fabricated in the Advanced Prototyping Lab at the Jacobs Institute for Design Innovation at UC Berkeley using a Multi-Material Color Objet260 Connex3 (Stratasys, Israel); some parts were also fabricated using the Carbon model M1 3D printer (Redwood City, CA). We chose these particular additive manufacturing processes because they were fast, low-cost, and enabled improved functional designs that were impossible to machine.

The new sampler incorporates the operation and water flow logic of a sampler built in 2004 for our surface buoy-tethered OSR but improves on it considerably (Fig. 7F in McDonnell et al. 2015; Bishop et al., 2016). The physical layout of the sampler is entirely new as the CFE-Cal had to meet stringent dimensional, buoyancy, compressibility, drag performance, and tilt criteria. Furthermore, as the sampler is intended to collect samples for particulate carbon, nitrogen, phosphorous, calcium carbonate, silica, and trace metals, it needed to be non-contaminating.

Figure 3.3(a) shows detail of the integration of the sampler with 4 mounted sample collection bottles on the CFE-Cal; Figs. 2b and 2c detail the particle isolation system within each sample bottle. A planetary gear motor (2842S024C; Faulhaber Group, Micromo, Florida) and related custom electronics which actuate the sampler are housed in a pressure compensated acrylic tube filled with Fluorinert (3M) fluid and is mated coaxially with the

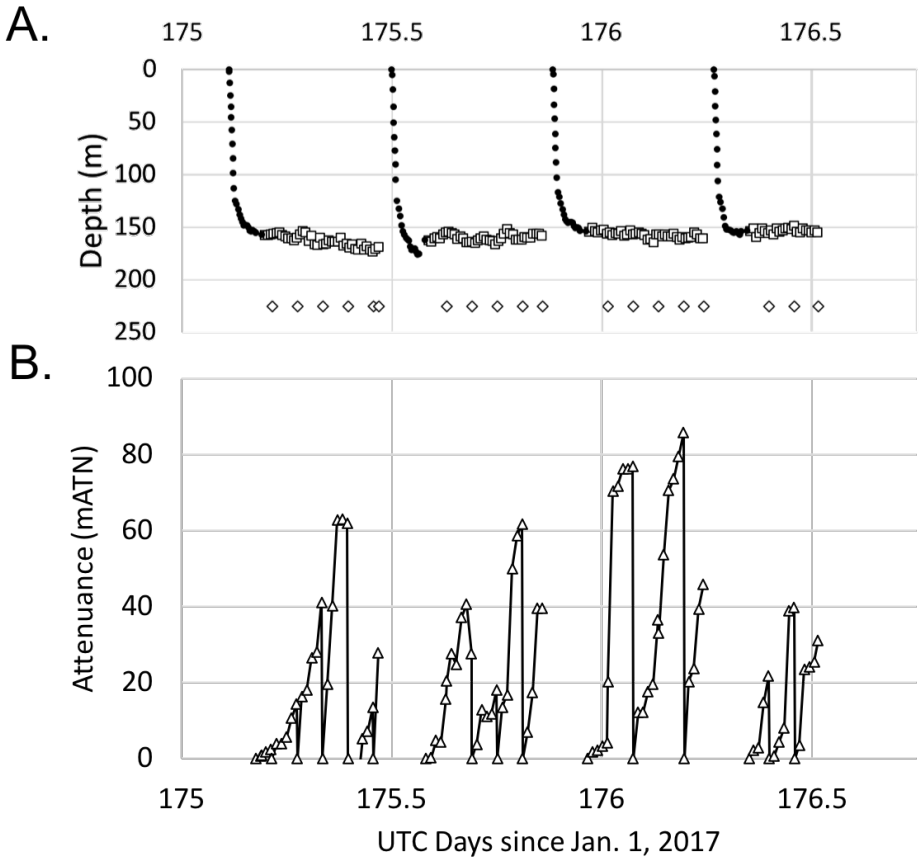

Figure 3.2: A) Typical deployment trajectory of a CFE-Cal. The x-axis is time in days (Jan 1 2017 at 1200UTC = day 0.5). The filled black circles are depths as the CFE-Cal is diving, open black squares denote depths as the CFE drifts and takes images of settled particles. The open black diamonds represent times when the sample stage was cleaned and particles directed into a sample bottle. B) Graph B shows the corresponding ATN for each photo taken. Particles build-up over time and then periodically the glass stage will be rinsed off and particles directed into the sample bottles.

rotor (Figure 3.3(d)). Fluorinert was selected as it is clear (necessary as there was an optical encoder in the pressure compensated chamber), low viscosity (for motor immersion) and inert (necessary as there were electronics in the chamber). The optical encoder provides feedback as to the proper location for the desired sampling bottle. Figure A2 shows details of the design of key 3D printed elements of the sampler. The sampler inlet is connected to the particle settling stage by a 40 cm long 9.5 mm inner diameter (ID) polyethylene tube (seen in Figure 3.3(a)) and its outlet is connected by a second 20 cm polyethylene tube to a SBE Model 5T (2000 RPM) pump (Sea Bird Electroncs, WA). Flow rate during cleaning was 20 mL s^{-1}. When the CFE reaches depth on a new dive, the rotor is moved to select

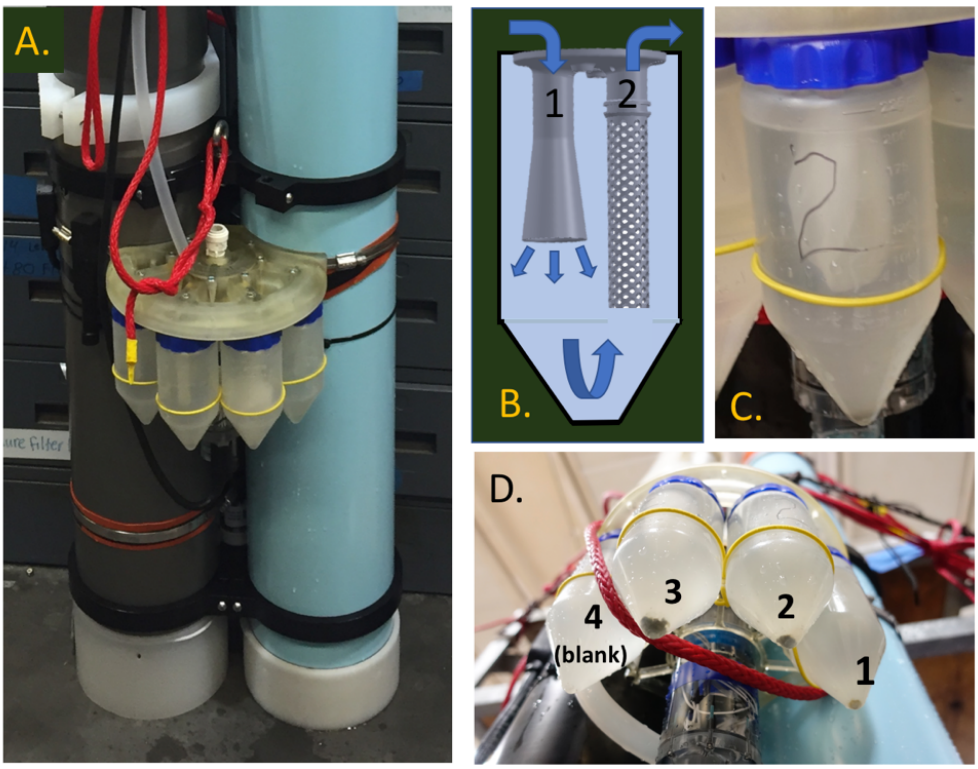

Figure 3.3: (A) Sampler on CFE-Cal. Suction action of a pump draws water and particles down a poly tube to the sampler (shown disconnected). (B) Detail of particle retention system within sample bottles. Inlet is cone shaped to decelerate incoming flow. Outlet is formed to accommodate 51 µm mesh which is retained by two o-rings at the top. (C) Closeup of bottle with Mesh filter in place; Filter area is 130 cm^2. (D) CFE-Cal recovery after 24-hour deployment showing collected samples. Bottle 2 is shown in C. In this case, bottle 4 was a blank (i.e. no particles directed to it).

a water path that bypasses the sample bottles (Fig. A2, port 0) and the flow is directed to the outlet manifold. The bypass cleaning volume is 800 mL. After a cycle of particle accumulation and imaging, the motor driven sampler rotator opens to one of four sample bottle positions (1 - 4, Figure 3.4) and the suction action of the pump draws water and particles from the imaging stage into the selected 250 mL conical clarified polypropylene centrifuge tube (Thermo Scientific, Nunc). A total of 400 mL of water is drawn through the sampling system during each regular cleaning cycle and represents about 30% of the volume of the collection funnel (1460 cm^3). All particle transfers from a dive are directed to the same bottle (diamond points in Figure 3.4). Particles are retained in the bottle by a 14 cm diameter circle of 51 µm polyester 33% open area mesh (SEFAR 07-51/33) wrapped and secured using silicone o-rings around the outlet structure within the bottle (Figure 3.3(c)). The area of perforated outflow cylinder was 30 cm^2; however, when the circular mesh was

secured to the top of the outlet cylinder by an o-ring, the pleated mesh area exposed to flow was 130 cm^2 (Figure 3.3(c)).

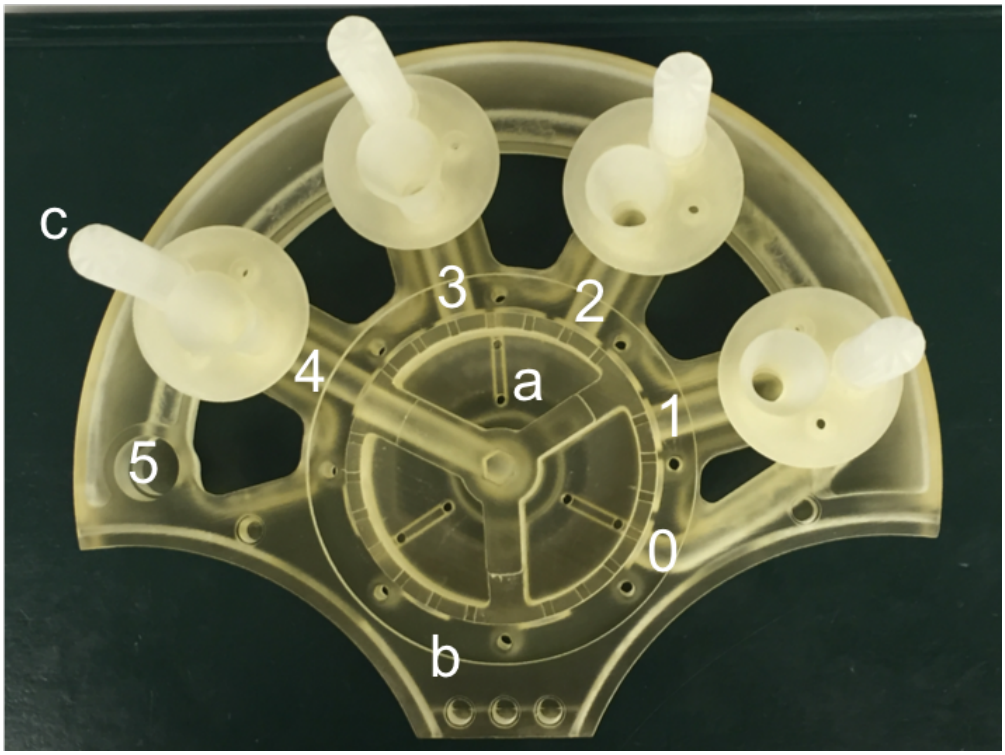

Figure 3.4: Sampler elements: (a) sample selector rotator; (b) main structural element of the sampler. Flow paths (1-4) direct water and particles into sample bottles or (0) to bypass sample bottles; and (c) particle retention system which bridges inflow channels and common exhaust manifold channel (5). Sample rotator is shown open at position 4. When not sampling, the rotator is sealed to closed positions.

The flow from imaging stage to bottle is constricted by the six 3 mm diameter openings that surround the sample stage. Loosely aggregated material is likely broken up into smaller pieces while being transferred. For cohesive aggregates and rigid particles (such as some Pteropod shells), the upper size limit is 3 mm. Though nothing was caught in the CFE-Cals during this study, this can occasionally occur. A larval crab entered one of the profiling CFEs and was not able to fit through the 3 mm diameter opening. This had to be removed after the CFE was retrieved.

3.2.3 Sampler Materials

Little is known about water absorption properties, dimensional stability, and chemical reactivity and contamination potential of the 3D printing resins as most are proprietary. The majority of sampler parts were fabricated using the Connex3 from FullCure 720 resin

(Figure 3.4) and some of the particle isolation assemblies were printed in both FullCure 720 and VeroWhite RGD35 resins. The Connex3 is a fused deposition modeling (FDM) printer which builds parts layer by layer. We fabricated three additional particle isolation assemblies from amber Cyanate Ester, black rigid Polyurethane and black Polylactic (PLA) resins on the Carbon printer; the process uses photopolymerization to form a solid piece as material is drawn from liquid resin. After parts were printed and support material removed, the parts were rinsed with deionized water and then leached in a 1.2 M HCl solution for 16 hours at room temperature. All remained stable to this treatment. Dimensional tests before and after sea trials showed that dimensions of the sampler body (Figure 3.4) printed with FullCure 720 remained stable to within 0.06% of design dimensions.

3.2.4 Field Procedures

Prior to each deployment, the CFE's sample stage and related glass surfaces were cleaned to remove any remaining material collected during the previous deployment. Areas between glass layers were flooded with water to prevent air bubbles being trapped. Each CFE-Cal was outfitted with four clean sample collection tubes and filled with 0.4 µm filtered seawater. On recovery of the CFE-Cals, the sample bottles (Figure 3.3(d)) were either immediately removed from the sampler and filtered or placed in a fridge at 10 °C to minimize sample degradation; in the latter case, samples were processed within 3 hours of collection.

All sample processing and manipulation took place in a laminar flow bench at sea. Each sample was decanted into an open filter funnel loaded with either 47 mm diameter Whatman Quartz Fiber (QMA, pore size 1.2 µm) or Supor (pore size 0.4 µm) filters; transfer took place with filters under mild suction with the aim of evenly covering the filter surface (Fig. A3). Each sample tube and associated 51 µm mesh were further rinsed three times with about 5 mL of 0.4 µm filtered seawater to ensure quantitative transfer of particles. After filtration, the samples were quickly misted with about 3 mL of deionized water (DI) to reduce residual sea salt while still under suction. Samples were then placed in Gelman Petri slides and photographed wet under LED ring light illumination using a 20 Mpixel Sony RX100 V camera (pixel resolution of 19 µm), dried at 50 °C for 24 hours, and photographed again under the same lighting conditions in a laminar clean air bench. Dried samples were then stored in covered petri slides until analyzed in the laboratory. Prior to use, the QMA filters were placed in a muffle furnace at 450 °C overnight to reduce carbon blanks. Both the QMA (after combustion) and the Supor filters were leached in a 1.2 M HCl solution for 24 hours at room temperature and rinsed with deionized water and air dried in a class 100 laminar flow bench prior to use.

Study Loc.	CFE	Latitude	Longitude	Dive	Bottle	Filter	UTC Day Start Dive	UTC Day End Dive	Hours	Depth (m)	Depth stdev	Sample Notes
1	2	35.0739	-121.1281	40	1	Supor	160.064	160.270	4.944	0.2		cfe did not dive
1	2			41	2	Quartz Fiber	160.333	160.500	4.008	70.0	12.3	anchovy fecal pellets
1	2			42	3	Supor	160.623	160.791	4.032	119.4	7.8	anchovy fecal pellets, not analysed
1	2	34.9978	-121.1650	43	4	Quartz Fiber*	160.849	160.851	0.048	186.0		sampler closed after bottle 4
1	4	35.0885	-121.1293	40	1	Quartz Fiber	160.076					sample selector failure
1	4			41	2	Supor	160.297					sample selector failure
1	4			42	3	Quartz Fiber	160.422					sample selector failure
1	4	35.0341	-121.1862	43	4	Supor	160.732					sample selector failure
1	2	34.9396	-121.2031	50	1	Quartz Fiber	162.091	162.294	4.872	131.7	10.9	
1	2			51	2	Supor	162.424	162.536	2.688	31.8	4.4	sample not analysed
1	2				3	Quartz Fiber*						
1	2	34.8962	-121.2032		4	Supor*						
1	4	34.9348	-121.1946	50	1	Supor	162.075	162.280	4.908	189.5	7.7	oil under sample stage reticle
1	4			51	2	Quartz Fiber	162.410	162.412	0.048	286.2		depth unstable
1	4			52	3	Supor	162.549	162.551	0.048			depth unstable
1	4	34.8997	-121.2165		4	Quartz Fiber*						
2	2	34.7771	-122.0572	60	1	Supor	165.047	165.264	5.208	142.9	3.8	
2	2			61	2	Supor	165.406	165.574	4.032	112.8	4.3	
2	2			62	3	Supor	165.716	165.883	4.008	97.7	4.1	
2	2	34.8651	-122.3355		4	Quartz Fiber	166.024	166.026	0.048			sampler surfaced open at position 4
2	4	34.7742	-122.0587	60	1	Quartz Fiber	165.060	165.278	5.232	160.9	4.2	C:N >20
2	4			61	2	Supor	165.430	165.597	4.008	153.1	5.7	not analysed
2	4			62	3	Quartz Fiber	165.739	165.900	3.864	150.2	3.0	
2	4	34.8825	-122.3499		4	Supor*						
2	2	34.7098	-122.3004	70	1	Supor	166.659	166.882	5.352	159.2	5.1	
2	2			71	2	Quartz Fiber	167.034	167.202	4.032	146.2	5.8	
2	2			72	3	Supor	167.350	167.517	4.008	147.8	3.9	
2	2	34.6771	-122.4122		4	Quartz Fiber*						
2	4	34.7091	-122.2998	70	1	Quartz Fiber	166.673	166.897	5.376	164.2	10.3	
2	4			71	2	Supor	167.044	167.211	4.008	157.6	3.4	
2	4			72	3	Quartz Fiber	167.364	167.531	4.008	151.5	2.9	C:N >20
2	4	34.6829	-122.4185		4	Supor *						
3	2	34.2275	-123.1480	80	1	Quartz Fiber	170.192	170.368	4.224	141.5	6.7	
3	2			81	2	Supor	170.472	170.639	4.008	131.4	3.8	
3	2			82	3	Quartz Fiber	170.740	170.879	3.336	143.7	6.7	C:N >20
3	2	34.1717	-123.0758		4	Supor *						
3	4	34.1129	-122.9885	90	1	Quartz Fiber	171.205	171.414	5.016	173.4	3.3	
3	4			91	2	Supor	171.553	171.721	4.032	160.9	0.1	
3	4			92	3	Quartz Fiber	171.860	171.903	1.032	148.8	0.8	
3	4	34.0749	-122.8673		4	Supor *						
3	2	34.1086	-122.9823	90	1	Supor	171.190	171.369	4.296	126.9	4.8	
3	2			91	2	Quartz Fiber	171.468	171.636	4.032	159.7	5.7	
3	2			92	3	Supor	171.737	171.904	4.008	154.7	3.6	
3	2	34.0714	-122.8552		4	Quartz Fiber *						
4	4	34.4070	-123.0958	100	1	Supor	174.180	174.369	4.536	190.6	5.7	
4	4			101	2	Supor	174.489	174.657	4.032	117.3	3.3	
4	4			102	3	Supor	174.767	174.899	3.168	135.0	3.5	
4	4	34.4174	-123.0535		4	Supor *						
4	2	34.4032	-123.0964	100	1	Quartz Fiber	174.294	174.354	1.440	165.8	132.5	depth unstable
4	2			101	2	Supor	174.479	174.646	4.008	139.9	3.0	
4	2			102	3	Quartz Fiber	174.742	174.903	3.864	129.5		
4	2	34.4216	-123.0310		4	Supor *						
4	4	34.4221	-123.0133	110	1	Quartz Fiber	175.187	175.487	7.200	164.0	5.4	
4	4			111	2	Supor	175.599	175.878	6.696	101.7	3.7	
4	4			112	3	Quartz Fiber	175.989	176.267	6.672	158.6	3.9	
4	4	34.4449	-123.0205	113	4	Supor	176.396	176.496	2.400	119.8	1.8	
4	2	34.4218	-123.0168	110	1	Supor	175.173	175.469	7.104	162.8	5.5	
4	2			111	2	Quartz Fiber	175.582	175.859	6.648	159.5	3.4	gelatinous organism
4	2			112	3	Supor	175.965	176.242	6.648	156.9	3.0	
4	2	34.4335	-123.1008	113	4	Supor	176.350	176.516	3.984	153.1	2.3	

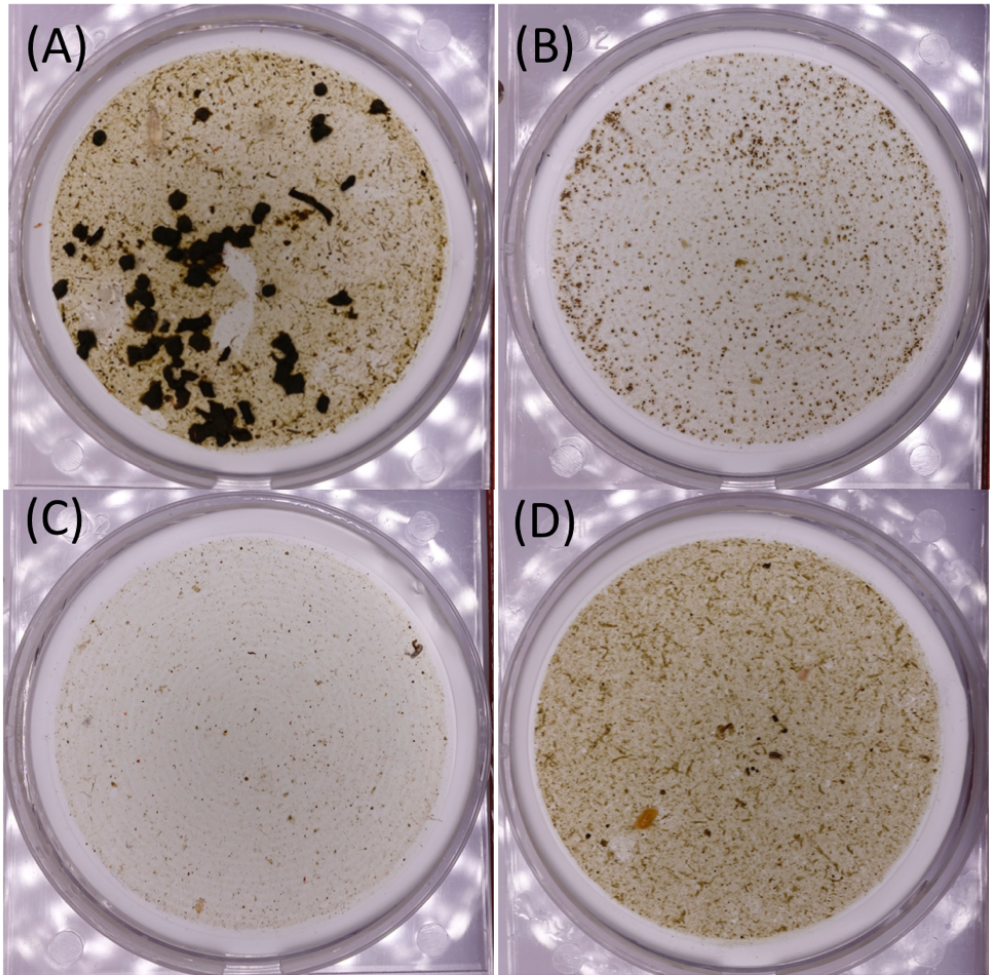

Figure 3.5: Representative images of sampled particulates from locations 1-4. The process of sampling retains morphology of cohesive aggregates. Turbulence on transit from imaging stage to bottle does disrupt the integrity of loosely aggregated millimeter sized particles such as represented in Figure 3D. (a) Location 1. CFE 002 dive 42 - Days 160.623 to 160.791 - Depth 119.4 ± 7.8 m. (b) Location 2. CFE 004 dive 71 - Days 167.034 to 167.202 - Depth 157.6 ± 3.4 m. (c) CFE 002 dive 90 - Days 171.190 171.369 - Depth 126.9 ± 4.8 m. (d). Location 4. CFE 002 dive 101 - Days 174.479 to 174.646 - Depth 139.9 ± 3.0 m.

3.2.5 Laboratory Procedures

Carbon and Nitrogen Analysis

Briefly, half of each QMA filter was placed in a desiccator and exposed to HCl fumes (from 12 M HCL) for 24 hours to remove any carbonate carbon (Bishop et al. 1978) and then dried at 30 °C for 36 hours and subsampled 6 to 8 times using a 3 mm diameter biopsy punch yielding $1/16^{\text{th}}$ of the whole sample. These were loaded into tin capsules and analyzed

for total organic carbon and nitrogen using a Thermo Quest EA2500 Elemental Analyzer at Oregon State University according to Holser et al. (2011). A total of 27 unique cruise samples and process blanks (with 6 replicates), 5 unused QMA filters, and analytical blanks (empty tin capsules) were run. Process blanks were samples where no particles were directed to sample tube during deployment and procesesed as other samples. The other half of the sample was preserved for ICP-MS analysis.

Replicate analysis of 4 samples gave an average RSD of 0.14 and 0.07 for C and N, respectively which we assume is attributed to sample heterogeneity and can be applied to all samples. The RSD for replicate analyses of process blanks was 0.18 and 0.12 for C and N.

Corrected POC was calculated following Eqn. (3.1):

$$\mathrm{POC}_{\mathrm{corrected}} = \mathrm{POC}_{\mathrm{measured}} - \mathrm{POC}_{\mathrm{process\ blank}} \tag{3.1}$$

The sample POC error was calculated following Eqn. (3.2):

$$POC_{error} = \sqrt{(process\ blank\ s.d.)^2 + (sample\ RSD\ X\ POC_{corrected})^2} \tag{3.2}$$

Nitrogen and phosphorous were calculated the same way, replacing POC with PN and PP.

ICP-MS Phosphorous Analysis

Samples on both Supor and QMA filters were analyzed using a Thermo Fisher Element II XR Inductively Coupled Plasma Mass Specrometer (ICP-MS) at the UC Santa Cruz Marine Analytical Laboratory following Bishop et al. (2012). Half of each 47 mm filter was leached in 10 mL of a 0.6 M HCl solution at 60 °C for 16 hours. The leach solution was then diluted with 18.2 mOhm-cm Milli-Q DI water to 50 grams; 1 mL of the diluted solution was then further diluted with 3 mL of 0.12 M HCl and spiked with 0.2 mL of 25 ppb In. Standards were prepared in the same acid matrix.

3.3 Results and Discussion

3.3.1 Samples Collected

Samples were collected from four productivity regimes and environmental conditions yielding a diverse array of particle sizes and classes (Figure 3.6,Figure 3.7). The flux rates between locations also varied widely. At location 1, flux was at times dominated by 1 mm diameter, 5-10 mm long anchovy pellets similar to those described by Saba and Steinberg (2012) with 95% of VA flux (average ∼40 mATN-cm^2 cm^{-2} d^{-1}) being carried by particles $>$ 1.5 mm in size. In contrast, at location 2, numerous small diameter (200-300 µm) olive green ovoid pellets dominated imagery and accounted for about 50% of the ∼15 mATN-cm^2 cm^{-2} d^{-1} VA flux. Location 3, in transitional waters near the filament edge, had a VA flux of ∼2.3 mATN-cm2 cm-2 d-1 and ∼65% of the flux carried by aggregates larger than 1.5 mm. At Location 4, in the most extended part of the filament, VA flux was ∼22 mATN-cm^2 cm^{-2} d^{-1}, and 94% of the flux was carried by aggregates >1.5 mm in diameter.

CFE-Cal malfunction (i.e. instrument not diving to depth, not stabilizing at depth, or sampler not switching target bottles correctly) or swimmers such as a large siphonophore led to some dives not yielding usable samples. The CFE-CALs were deployed 15 times over the course of the June 2017 CCE-LTER study, the CFE was outfitted with 4 bottles for each deployment. Of the 60 possible samples, there were 8 sample collections that failed due to a malfunction (either the float not diving, or the sampler not working). These malfunctions occurred almost entirely at the beginning of the cruise. As all instrument malfunctions were resolved, future deployments will be far more robust. In one dive, a gelatinous swimming organism entered the imaging stage and remained throughout the dive, rendering the sample not useable. Table 1 details all these points as well as noting sampling times, depths and filter type. Process blank samples are labeled with a star.

There was a total of 15 QMA samples which were analysed for POC, PN and PP and a total of 20 Supor samples. Samples ranged from 0.0267 to 0.1570 mmol C/filter (average ± sd: 0.0760 ± 0.0362) and 0.0029 to 0.0155 mmol N/filter (average ± sd: 0.0065 ± 0.0034). Phosphorous in samples ranged 40-fold from 3.9×10^{-5} to 1.5×10^{-3} (average ± sd: 2.0×10^{-4} ± 2.4×10^{-4}).

Blanks were subtracted from the sample values as shown in equation 1. There was a total of 5 QMA process blanks (see Table 1 for detail). As there were only 5 QMA process blanks, an average of all these process blanks was used for POC and PN. This drove one sample negative, though not negative within error. This one sample that was driven negative was collected from location 3. Fluxes at location 3 were very low - an order of magnitude lower than samples collected in other regions. Process blanks contained 0.032 ± 0.008 mmol C/filter and 0.003 ± 0.0003 mmol N/filter. Unused QMA blanks were 0.0037 ± 0.0008 mmol C/filter and were below the detection limit for nitrogen; only 12% of carbon in the process blanks came from the blank filter. Nearly 90% of the process blank carbon is due either to accidental collection of particles during deployment, contamination during initial processing,

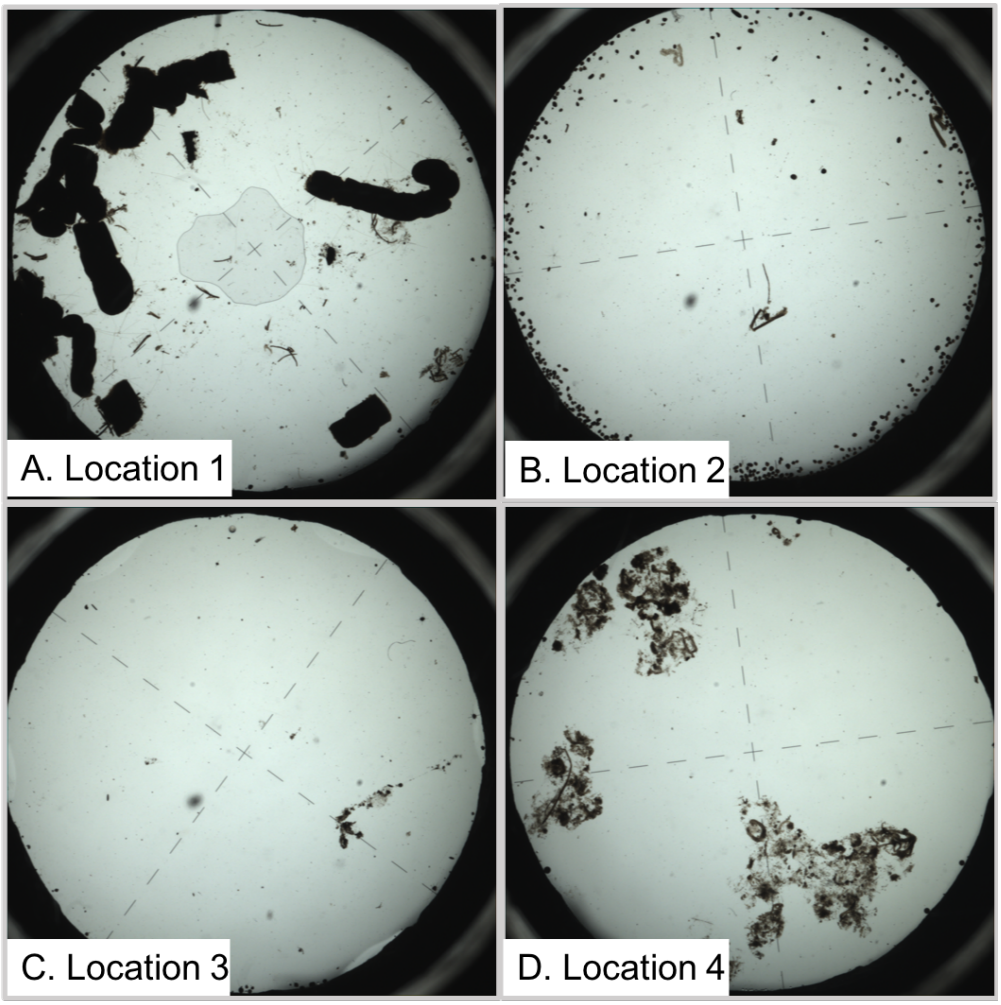

Figure 3.6: Representative images from four locations. The particle size classes present varied widely at the four different locations. (A) In location 1, flux was dominated by large 1 mm diameter anchovy fecal pellets. (B) Flux was dominated by small ovoid pellets 200-300 microns in diameter. (C) Location 3 was characterized by very low flux. Flux was dominated by small particles with the occasional large aggregate. (D) Flux was dominated by large aggregates.

or from DOC adsorption. Particles may enter a sample bottle while the sampler is turning and the selector briefly passes the blank bottle inlet. As there were were at least two process blanks per location for PP, blanks were location specific. The process blanks were location specific with averages of 8.9×10^{-5}, 5.0×10^{-5}, 1.9×10^{-5} and 5.0×10^{-5} mmol P/filter for location 1, 2, 3 and 4 respectively. No samples for PP were negative.

Replicate analysis of 4 samples gave an average RSD of 0.14 and 0.07 for C and N. Punched subsamples are collected evenly distributed across the filter, but inevitably as there

are discrete particles on the filter, there is some heterogeneity between the sub-samples. The RSD of replicate analysis we assume is attributed to sample heterogeneity and can be applied to all samples. The RSD for replicate analyses of process blanks was 0.18 and 0.12 for C and N.

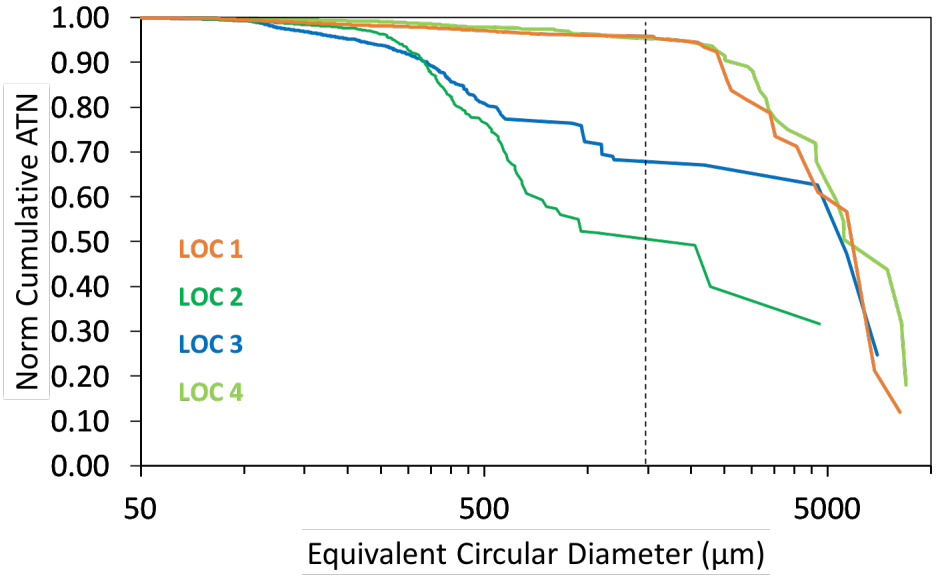

Figure 3.7: Cumulative normalized volume attenuance vs. equivalent circular diameter curves representative of the 4 locations. Approximately 95% of flux was carried by aggregates >1.5 mm in size at locations 1 and 4. Location 2 had 50% of flux in >1.5 mm fraction.

3.3.2 Transfer Efficiency

To validate the efficiency of transfer of particles imaged to sample bottles, ovoid pellets were manually counted (Figure 3.8) in both the CFE's OSR images and of photographs of filters of material sampled at location 2. CFE002 collected close to the same number of particles in the sampler as were imaged. CFE004 collected 1.45 times more ovoid pellets in the sampler than were imaged. The sampler uses an optical encoder to sense a home position from which it advances to select specific bottles. Software is programmed with a time out in the case that the "home" position cannot be found to prevent continuous operation and depletion of the CFE batteries. During pre-cruise tests of the CFE-Cal no positioning errors were registered. However, these tests were done in a lab, with room temperature water and not in 10řC water under pressure. Sampler stopped short of home position, which likely led to the over transfer of particles that were not imaged. To correct for this, the POC, PN and PP numbers for CFE004 at location 1, 2 and 3 were divided by 1.45. We recognized this during deployment operations at cycle 3 and increased the timeout length for cycle 4, which resolved the issue.

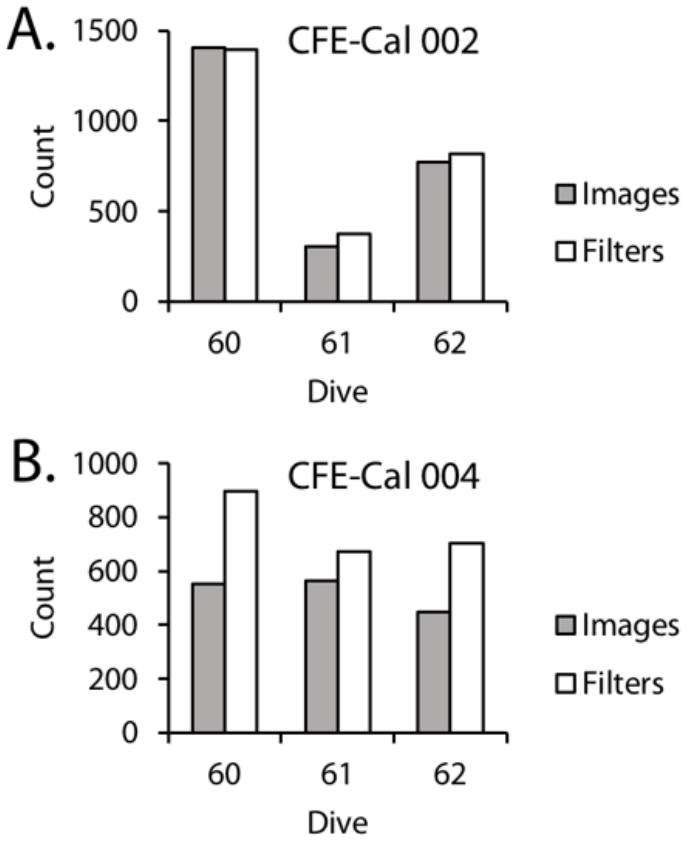

Figure 3.8: Comparison counts of ovoid pellets in images versus on filters. (A) CFE-CAL002 Deployment 3 (first deployment at location 2) (B) CFE-CAL002 Deployment 4 (second deployment at location 2).

Bishop et al., (2012) investigated the effect of filtration rate on aggregate retention during large volume in-situ filtration sampling and found that aggregates were broken up when the flow velocity through 51 µm mesh exceeded 1 cm s^{-1} over a four-hour sampling time. During CFE-Cal stage cleaning, the sample transfer pump is operated for two cycles of ten seconds at a flow rate of 20 mL s^{-1}. The mesh area on the outflow from the sample bottle is approximately 130 cm^2. We thus calculate the flow speed through the mesh to be 0.15 cm s^{-1}, 15% of the threshold speed recommendation by Bishop et al. (2012). Although intact large aggregates were not seen on the sample filters (compare Fig. A3d vs. Fig. 3d), given our limited sample transfer time ($<$ 2 minutes) and low flow velocity, we believe that our transfer efficiency for the particles comprising the loosely aggregated material is similar to that for the more robust pellets.

3.3.3 Calibration Results

Figure 3.9 shows cumulative VA regressed against sample POC, PN and PP. All of our results are forced through zero as both VA and elemental values are blank controlled. Regressions results yielded slopes and R^2 values and number of samples (in parentheses) of 10,066 mATN-cm^2: mmol POC (0.86, n=12) and 100,500 mATN-^{2}: mmol PN (0.87, n=15). Three of 15 samples had C/N ratios above 20 and were not used in the regression for POC as these numbers are not typical of sinking particles (e.g. Bishop et al., 1977, Lamborg et al., 2008, Stukel et al., 2013). Stukel et al. (2013) reported trap POC/PN mole ratios ranging from 5-14 (average, 9.6) at 100 m in the same upwelling regime we have sampled; Lamborg et al. (2008) reported POC/PN ratios ranging from 7.7 to 8.5 in productive waters of the Oyashio and Oligotrophic waters of the North Pacific Gyre. The molar ratio of C/N from our regression slopes is 9.92, in line with Stukel et al., 2013. The high C/N values of excluded samples may have been due to contamination by residual material used as a scaffold to build the 3D printed parts; in one case, a 1 mm sized aggregate of such material was found on our filters. The scaffold material, Stratasys' OBJET Support SUP706 is made of 1,2-Propylene glycol and Polyethylene glycol, Methanone, (1-hydroxycyclohexyl) phenyl-both of which contain carbon but not nitrogen (SUP706 SDS https://store.stratasys.com/medias). The material also contains an unspecified acrylic. Any DOC or DON leaked from the 3D printed part would not be retained in the collected sample. The C/N of the other 12 samples were all consistent with natural populations. These are in line with C/N that have been found in the region previously (Stukel et al., 2013). As the 3D printed material contains no nitrogen, C/N values would elevated if they were contaminated. Including the three high C/N ratios in the VAF:POC regression changes the slope to 8,552 with an R^2 of 0.64 (n=15); we report this even though we do not believe this to be representative of natural particulates.

The data also demonstrate that there is no obvious difference for VA:PN or VA: POC for samples collected from Locations 1 and 4 (Fig. 1, Fig. 4) where aggregates $>$ 1.5 mm in size accounted for 95% of the flux compared to Locations 2 and 3 where smaller material contributed 50 and 30% of the flux, respectively.

The high C/N values of excluded samples may have been due to contamination by residual material used as a scaffold to build the 3D printed parts; in one case, a 1 mm sized aggregate of such material was found on our filters. The scaffold material, Stratasys' OBJET Support SUP706 is made of 1,2-Propylene glycol and Polyethylene glycol, Methanone, (1-hydroxycyclohexyl) phenyl-both of which contain carbon but not nitrogen (SUP706 SDS https://store.stratasys.com/medias). The material also contains an unspecified acrylic. The regression of cumulative VA: POC is less significant than VA:PN. Part of this is due to the greater relative variability of carbon blanks versus nitrogen blanks.

The relationship for VA: PP was scattered with a slope of 1,543,000 mATN-cm^2: mmol PP (-0.07, negative r^2 values denote results worse than horizontal fit). One sample heavily laden with anchovy fecal pellets had a PP content far higher than all other samples (POC/PP

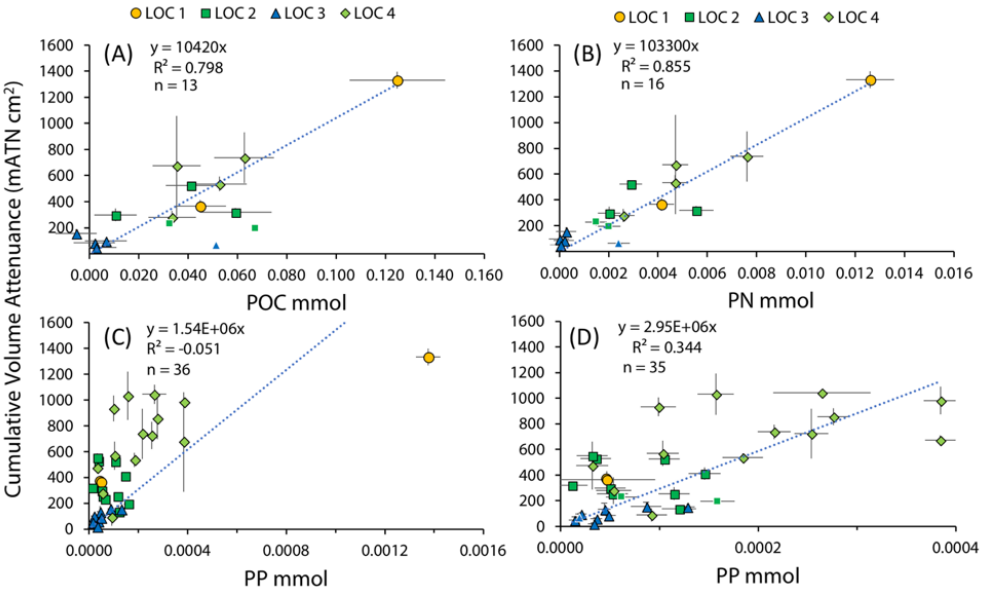

Figure 3.9: Data and regressions of sample POC (A), PN (B) and PP (C and D) vs. cumulative volume attenuance. Fits are forced through zero. Smaller symbols in all plots denote samples excluded from the POC regression analysis; these had C/N values >20 and were likely contaminated for carbon and not nitrogen. No data was excluded from PN or PP regressions. P regressions (C and D) include and exclude, respectively the high P enriched sample which was dominated by anchovy fecal pellets. In either case, the low R^2 for the VA:PP relationship implies that VA cannot be used to predict PP.

ratio 90) and when this point was removed the relationship of VA: PP improved 3,23,000 mATN-cm^2 : mmol PP (0.41). The fact that PP had the lowest correlation with VA is consistent with the strong loss of P relative to carbon and nitrogen as large aggregates sink (e.g. Bishop, 1977; Lam et al., 2007). Scanning electron microscopy showed that the anchovy fecal pellets were stuffed with diatoms and as they are larger and sink at a much faster rate (up to 500m in one day), it follows that this sample should have a higher PP content as there is less time for microbial degradation and remineralization. Even when eliminating that particular point, the relationship between PP and VAF was still far less robust than that of POC or PN. Though the ultimate goal is to allow an estimation of biogeochemical fluxes based on image analysis, because of the highly heterogeneous nature of phosphorous in particles, such as the anchovy pellet, PP cannot be predicted from VA.

The ratio of C/P using the regression slopes is 152 with slope including high P sample, and 321 excluding it. These C/P ratios both agree well with pooled results for >53 µm particles sampled from depth interval 100-200 m in the Eastern Equatorial Pacific (Bishop, Stepien and Wiebe, 1986), Atlantic (Bishop et al., 1977), and waters of the Southern Ocean (Lam and Bishop, 2007) which had an average Corg/P = 211 (range 137 to 360). They

also fall in the range Lamborg et al. (2008) reported for 150 m trapped material at the VERTIGO Aloha (range 238 - 409) and Oyashio regimes (83-180).

3.3.4 Comparison to Previous Studies

Two autonomous flux monitoring systems, the CFE (Bishop et al., 2016) and the OST (Estapa et al., 2017), have now been calibrated to relate the attenuance flux to the flux of particulate organic carbon. This study expands upon Estapa et al. (2017) as samples from a wider range of environments have been collected and a far greater range of aggregate size distributions were observed. The highest POC flux collected in Estapa et al.'s (2017) calibration was under 2 mmol C m^{-2} d^{-1}. The flux environments sampled in our study ranged from <2 to 40 mmol C m^{-2} d^{-1}.

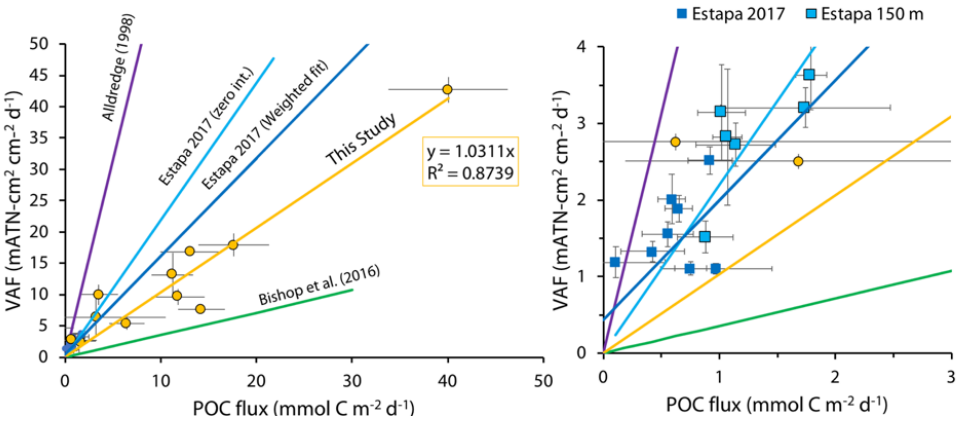

Figure 3.10: Regressions of ATN-POC (mATN-cm2 cm-2 d-1) to POC (mmol C m2 d-1) for this study (orange; y = 1.03x , R2=0.874), Estapa et al. (2017, blue, y = 1.56x + 0.434, R2 = 0.632; light blue, y = 2.191x, R2 = 0.47). Bishop et al. 2016 estimated slope (green) is 0.357 (1.0/2.8). Alldredge (1998) estimated slope (purple) = 6.25. As this study's calibration is created using samples collected at 150m, we separate out Estapa's (2017) data collected in 150m by marking in light blue for comparison. (A) shows the entire range of VAF and POC flux from this study. (B) zooms in to flux less than 3 so flux from Estapa et al. (2017) is highlighted.

Figure 6 compares the relationship between VA flux and carbon flux from this study vs. data from Estapa et al. (2017). When converted to compatible units, the slope for Estapa's VA flux (mATN-cm^2 cm^{-2} d^{-1}) versus POC flux (mmol C m^{-2} d^{-1}) is 2.19 (forced through zero) and 1.50 (allowing for an intercept) while our slope is 1.03 (forced through zero). Estapa et al. (2017) calculates mATN by taking the natural log of transmittance, observations are reported in units of ATN m2 m-2 d-1. Our data are log10 transforms of transmittance as documented in Bishop et al. 2016 and reported in units of mATN cm2 cm-2 d-1. Therefore, Estapa's data has been divided by 2.303 to convert the natural log attenuance to log10

attenuance and multiplied by 1000 to scale to mATN units. The dimensional data do not require scaling. Our observations were for depths near 150 meters and it is unknown if there is a depth dependence to calibration factors. We note that Estapa et al. (2017) combined samples from 150, 300 and 500 meters in their regression. This said, the slopes of our two datasets differ by only a factor of 2. In our data, attenuance of particles in the red image plane is 6% lower than in green, thus wavelength of analysis is a minor factor explaining the differences. Given the large range in particle size distributions, we can rule out particle size effects. Beam geometry and the other factors underlying our different methodologies likely explain the differences found.

Bishop et al. (2016) estimated the factor for conversion of POC flux (C mmol m^{-2} d^{-1}) to VA flux (mATN-cm^2 cm^{-2} d^{-1}) to be 2.8; the reverse conversion factor is 0.357 consistent with slopes depicted in figure 6. Analysis of directly imaged and sampled material in this study yielded a slope of 1.03, which is about 3 times higher than estimated using Bishop et al., (1978) but 6 times lower than inferred from Alldredge's (1998) relationship for marine snow sampled by scuba from shallow depths. Bishop et al. 2016 derive the conversion factor for POC:VAF for Alldredge which is 17 times lower than the Bishop et al. 2016 factor of 2.8. Therefore, since axes in the figure are reversed, 2.8/17=.165 compared to our slope of 1.03. The slope for the Alldredge relationship is 6. Our results are not consistent with the published Alldredge (1998) relationship.

Bishop et al. (2016) reported CFE attenuance fluxes averaging 66.2 mATN-cm^2 cm^{-2} d^{-1} at 150 m in the Santa Cruz Basin in January 2013 and estimated a POC flux of 190 mmol C m^{-2} d^{-1}, about 8 times higher than the highest previously measured flux from surface-tethered sediment traps deployed over a 3-year period at 100 and 200 meters in nearby waters (Thunell, 1998; August 1993 to September 1996). Converting the 66.2 mATN-cm^2 cm^{-2} d^{-1} attenuance flux to POC flux using our new calibration yields 68.19 mmol C m^{-2} d^{-1}, a value which is still three times higher than the highest previously measured flux (Thunell, 1998). In short, the likely discrimination of surface tethered baffled sediment traps against the collection of >1 mm sized particles remains an issue in biologically dynamic regimes dominated by large aggregates.

3.4 Conclusions

The development of a sampling system for the Carbon Flux Explorer has overcome a major barrier to the calibration of our attenuance proxy for organic matter export. The calibration of volume attenuance flux (VAF) against organic carbon, nitrogen and phosphorus flux in this study represents an important step forward in the development of autonomous optical flux measurements. Our regression results yield well-correlated calibrations for POC and PN (POC $R^2 = 0.86$ and PN $R^2 = 0.87$) that apply over a wide range of environments, from highly productive upwelling regions with flux containing large, dense anchovy pellets

to offshore marine snow aggregates. Phosphorus was shown to be poorly correlated, consistent with the highly labile nature of this element relative to either C or N. Our results give us confidence that images collected by the CFE can be used to calculate the fluxes of carbon and nitrogen. In addition, our calibration is shown to be insensitive to particle size distribution and particle classes dominating export. We find less than a two-fold difference in the POC flux vs. Volume Attenuance flux regression slope from Estapa et al. (2017). This is remarkable given the strongly different environments, methodology, and means by which fluxes were sampled. Both these studies reinforce the theory that light attenuation can be used as a proxy for POC and in our case PN flux. For the CCE-LTER, logistics dictated that all samples in this dataset were collected near 150 m. It is important to extend these results to different oceanic regions, environments and ecosystem structures as well as greater depths to answer the question as to whether the calibration relationships are globally applicable. Intercalibration of the CFE attenuance measurements with other autonomous systems should be pursued. Results presented above demonstrate that the magnitude of flux and of food web processes responsible for flux can vary strongly over relatively small spatial and temporal scales in dynamic coastal waters. Thus, the use of high frequency autonomous observations will significantly better inform food web and carbon export simulations. Our successful calibration of VAF in terms of POC and PN justifies further development of instruments such as the Carbon Flux Explorer and longer deployments.

Chapter 4

Carbon Export Beneath a Dynamic Upwelled Filament off the CA Coast

4.1 Introduction

Current estimates for carbon export driven by the biological carbon pump, the process by which photosynthetically derived biomass is transported out of the surface layer, range from 5 to >12 Pg C yr^{-1} (Boyd and Trull, 2007; Henson et al., 2011; Li and Cassar, 2016; Dunne et al., 2005; Siegel et al., 2014, 2016; Yao and Schlitzer, 2013). Atmospheric carbon concentrations are in part controlled by the depth at which sinking organic matter is remineralized (Kwon et al., 2009). Understanding the mechanisms which govern export and its remineralization depth are crucial in order to better inform global carbon cycle and food web models. How carbon is exported to deeper waters beneath highly productive coastal regions is poorly understood. Because coastal upwelling regions are such productive and unique ecosystems with complex current interactions, a question to be asked is: is export of material to depth in these systems different than in open ocean environments. If so, knowing the rules governing particulate carbon export in these regions will significantly advance carbon cycle simulations of CO_2 uptake by the oceans.

The coastal California current system is an eastern boundary current at the edge of the North Pacific gyre that flows south from the sub-arctic North Pacific. Beneath it, the subsurface California Undercurrent flows north at depths between 200 and 500m, with strong seasonal variability (Lynn and Simpson, 1987). Along the coast, the complex interactions of filaments, geostrophic flow, wind-driven Ekman transport and mesoscale eddies distribute coastal waters. This leads to a heterogeneous pattern of productivity in surface waters with some regions having high productivity levels due to coastal upwelling, while others have intermediate productivity spurred by wind stress curl upwelling or low productivity in more oligotrophic waters brought into the coastal region through mesoscale processes and Ekman transport (Gruber et al., 2011; Ohman et al., 2013; Siegelman-Charbit et al., 2018). In the summer, winds blowing south along the coast cause surface waters to divert to the west,

which allows deep nutrient rich cold water to come to the surface. This water coming to the surface moves out to sea in filaments which can develop and stretch several hundred kilometers off the coast.

While ocean color satellites provide temporal and spatial scale of these blooms when clouds permit, flux beneath the euphotic zone is much more difficult to observe and therefore not as well known. A number of recent studies have noted discrepancies in reconciling meso- and bathypelagic activity with current euphotic zone flux estimates (Banse, 2013; Burd et al., 2010; Ebersbach et al., 2011; Passow, 2012; Stanley et al., 2012). Measurements of new production (Eppley and Peterson, 1979) and net community export are typically greater than gravitational export measurements taken at the same time, though these two processes should be equal (Bacon et al., 1996; Estapa et al., 2015; Stukel et al., 2015).

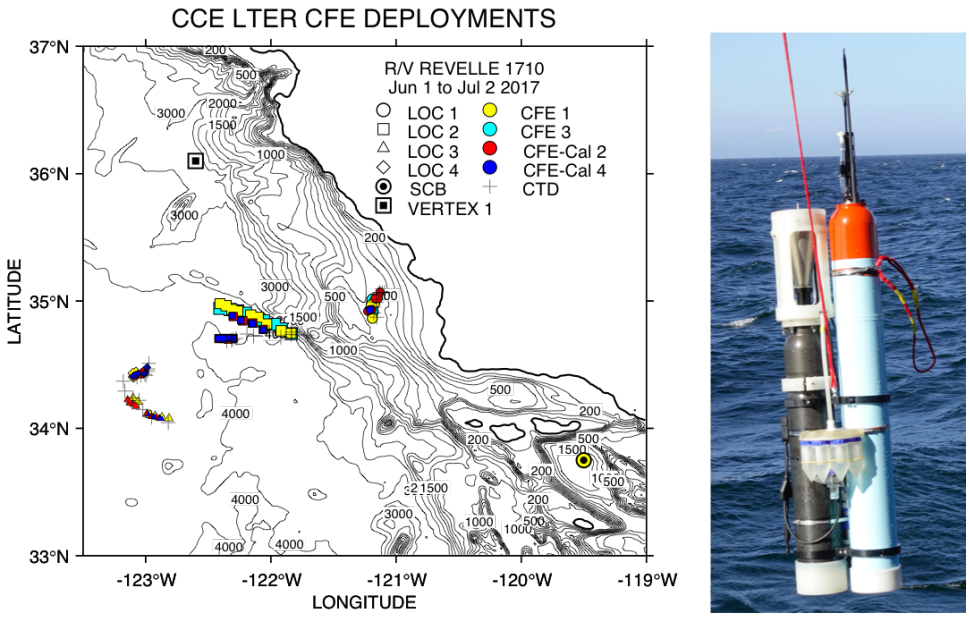

Figure 4.1: CFE and CTD Locations. CTD cast locations are plus symbols. CFE1 (yellow), CFE-Cal 2 (red), CFE3 (cyan) and CFE-Cal 4 (dark blue). The CTD stations were close to a drifting surface drogued productivity array. For the majority of stations, the CTD and CFE are close to one another. However at location 2, the CFEs strongly diverge to the Northwest. A CFE-Cal is shown to the right.

The California Current Ecosystem Long-Term Ecological Research (CCE-LTER) process study (June 1 - July 2 2017) gave us the opportunity to observe flux beneath a rapidly evolving surface filament in an upwelling coastal environment. The overall goal of the 2017 cruise was to understand the magnitude, scales and mechanisms of coastal production and its transport. In order to contribute to that goal, Carbon Flux Explorers (robotic lagrangian

floats which image sinking particles, described in Chapter 3) were deployed at various depths to 500 m to record particle flux, its variability and particle classes contributing to flux over the lifetime of a productive filament. Figure 4.1 shows the locations of CFE deployments as well as the coastal station VERTEX I (Martin et al., 1987) and the Santa Cruz Basin (SCB, Bishop et al., 2016).

The strength and efficiency of the biological carbon pump is governed by complex interactions between phytoplankton, zooplankton and physical mixing. Open ocean sediment trap observations typically show a decrease of sinking material with depth (eg. Martin et al., 1987). The most common mathematical expression used to express such observations is a power law expression (eg. Buesseler et al., 2007; Marsay et al., 2014; Martin et al., 1987).

$$F = F_{ref}(\frac{Z}{Z_{ref}})^{-b} \tag{4.1}$$

The Martin Curve (4.1) was derived from surface tethered sediment trap observations made in the North Pacific during the 1980 VERTEX program (Martin et al., 1987). Bishop (1989) composed 7 formulations for particle flux at depth and found that such power law functions for predicting flux were most robust for open ocean environments. Though studies show varying values of "b," all show a flux decrease with depth (Figure 4.2 (Bishop, 1989; Buesseler et al., 2007; Lutz et al., 2007; Marsay et al., 2014; Martin et al., 1987).

The Martin curve does not fit always fit flux observations, especially in regions that are both physically and biologically dynamic. For example, observations from a seasonal study conducted between 2011 and 2013 in the Santa Cruz Basin (Bishop et al., 2016) and the summer of 2009 in the North Atlantic proceeding the spring bloom (Giering et al., 2017) both exhibit non-Martin behavior. In this study, we do not observe flux attenuating with depth at any of our locations. In some locations we see flux constant with depth. In other locations we observe inverse Martin curves, where flux appears to increase with depth.

If all material collected at depth in sediment traps is assumed to be gravitationally exported material originating from a stable photosynthetically derived source in the euphotic zone, an increase of material with depth should not occur. We present four mechanisms which can explain why particle concentration profiles may diverge from traditional Martin-like behavior. We further explore reasons why the flux profile from the coastal station VERTEX I (Martin et al., 1989) results differ from observations made in this study.

4.1.1 Mechanisms for Drivers of Non-Martin Export

Efficiency of Grazing Community and Active Transport (M1)

Zooplankton are highly important to POC export as their fecal pellets package smaller non-sinking phytoplankton, however flux due to zooplankton fecal pellets is highly dependent

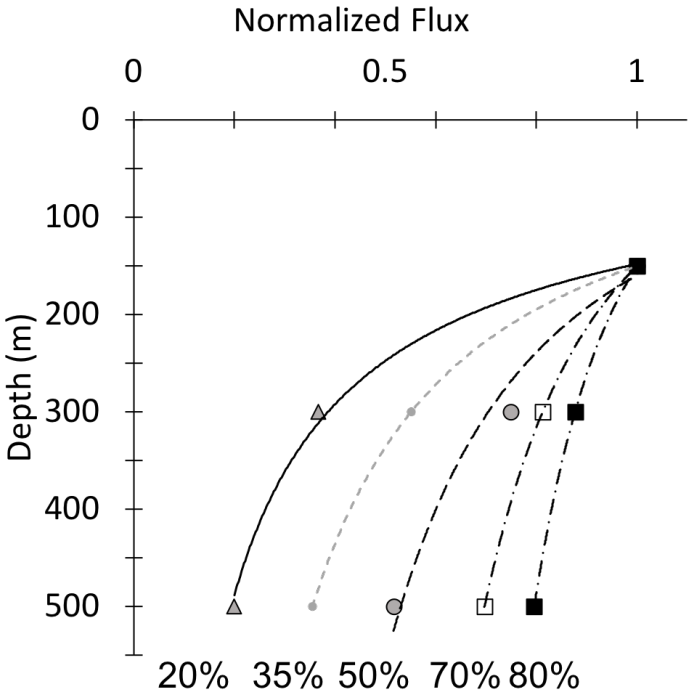

Figure 4.2: Martin curves reproduced from Martin et al., (1987), Buessler et al., (2007) and Bishop et al., (2016). B values of lines from left to right are: -1.33, -0.86, -0.51, -0.19 and -0.3 for stn. ALOHA, Martin et al., (1987), stn. K2 and Bishop et al., (2016) respectively. These values led to export efficiencies to 500m from 20% to 80%

upon the zooplankton community present (Turner, 2015). The community of organisms that develop following a chlorophyll bloom can have great impact on how surface material is exported to the mesopelagic. The diversity of sinking particle classes is illustrated in Bishop et al. (1986).

High levels of production and biomass does not necessarily imply high export (Bishop et al., 2004, 2016; Lam and Bishop, 2007). In a multi cruise study off the coast of California, Bishop et al. (2016) found that highest export levels coincided with lowest levels of surface chlorophyll. None of the flux profiles from the cruises (January, March and May) were traditional Martin curves (Figure 4.2). High levels of productivity, combined with efficient grazing and weak remineralization likely combined to create the conditions observed in January (Bishop et al., 2016).

Vertical migrators can also transport material to depth. Diel vertical migrators such as euphausiids, salps and copepods consume material at the surface during feeding times, and then can excrete material when they retreat to depth. Fish can also transport consumed material to depths below the euphotic zone.

Non-Steady State Flux (M2)

As Giering et al. (2016) points out, there are cases, especially associated with bloom scenarios, where the water column is not in steady state. Conducting flux studies using particle flux profiles from sediment traps deployed at different depths to quantify depth of remineralization assumes that export from the surface does not significantly change during the time it takes sinking matter to reach the deeper traps. If a substantial portion of the sinking organic matter sinks slowly enough, the material reaching the deepest trap in a series may have originated from a different environment and community than the exported material collected in the shallowest trap on the same day (Figure 4.3).

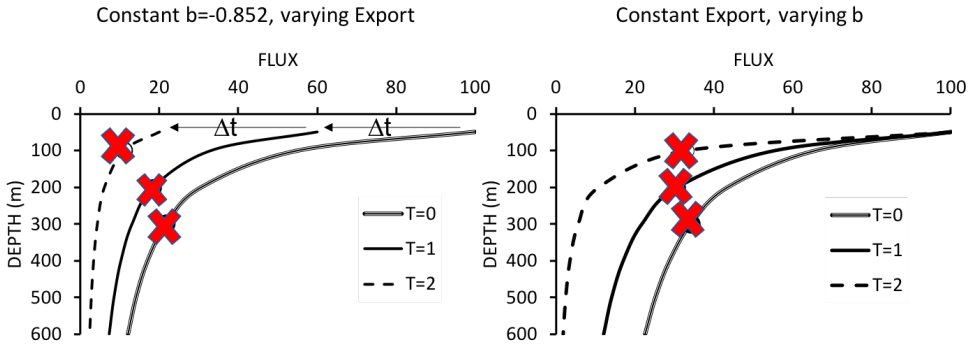

Figure 4.3: Scenarios which could lead to flux not systematically decreasing with depth. (A) depicts constant flux at the reference depth over time, with differing values of "b". B values for the T=0, T=1 and T=2 lines are -0.6, -0.83 and -1.6 respectfully. (B) depicts decreasing flux at the reference over time with constant "b". Red marks indicate sampling points, illustrating how temporal delay could lead to observations of increasing flux with depth. Circles indicate sampled flux.

Coastal Californian waters can be very dynamic. Upwelled coastal water can spawn productive filaments and eddies that are gone within several weeks. If flux sampling was conducted a week after peak bloom conditions, flux near the surface may be fairly low at time of sampling. The products of grazing, or un-grazed aggregated remains, of the peak bloom may still be captured by the deeper sediment traps. Such a scenario could produce Martin fits indicating flux increases with depth (Figure 4.3).

Physical Subduction (M3)

Particles are transported by both gravity and horizontal and vertical advection. The percent contribution of subduction to export is variable depending on currents. Export of particulate organic carbon (POC) to depth is typically primarily contributed to sinking

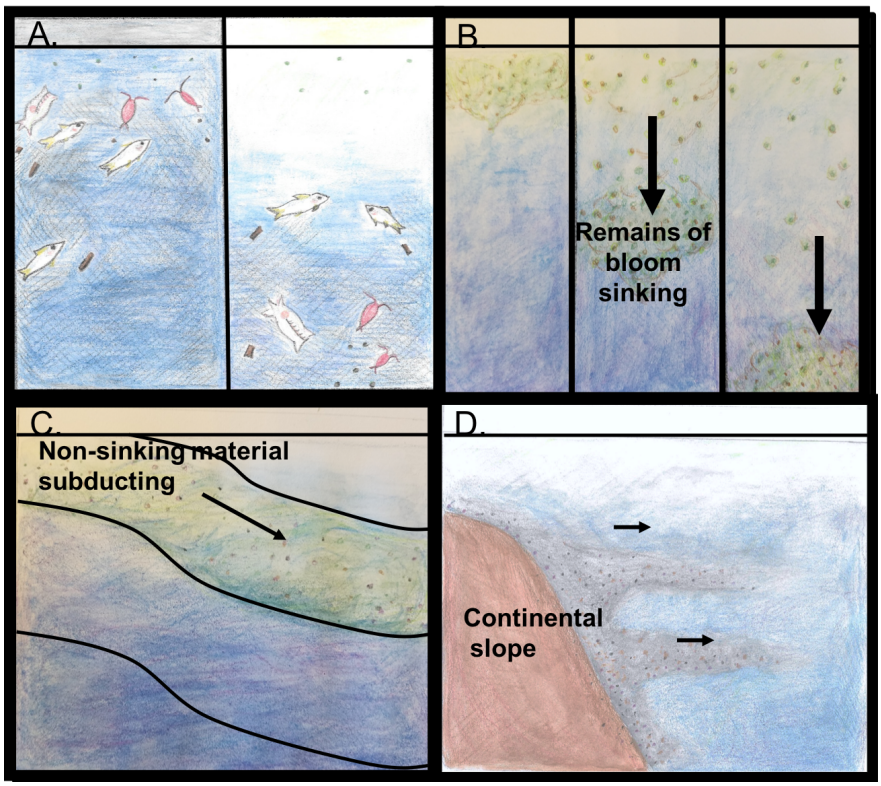

Figure 4.4: Different mechanisms which could lead to flux profiles which do not decrease with depth: (A) vertical migrators (B) temporal delay (C) physical subduction and (D) lateral advection

particles. However, sub-mesoscale eddy driven flux may be responsible for delivering a large percentage of POC to depth (Omand et al., 2015). Stukel et al. (2018) found subduction was responsible for about half of POC export in a frontal region in the CCE; however, subducted particles were primarily remineralized by 150m, whereas 50% of gravitationally exported material reached depths deeper than 500m.

Lateral Advection (M4)

Deep water currents flowing along continental shelves can pick up sea floor sediments and then transport this material out to sea as it flows along isopycnals. This mechanism can bring material out to the mid-layers of the water column, increasing material seen at depth in sediment traps. In a box model study, Alonso-Gonzalez et al. (2009) estimated suspended POC lateral transport in the Canary Current region to be up to 3 orders of magnitude higher than vertical fluxes, carrying material up to 1,000 km offshore. Their results suggest that laterally suspended POC advected from the continental shelf is a significant part of the

mesopelagic carbon current budget in the Canary Current and that if this is true in other boundary regions, this transport may play a crucial role in global carbon cycle.

In the eastern boundary current of the North Pacific, lateral transport has been found to play an important role in a number of processes. Intermediate nefloid layers found several hundred meters below the surface off the coast of Oregon are likely to be the product of lateral advection off the continental shelf (Pak et al., 1980). Intermediate nephloid layers have also been observed forming between 70 and 150m depth on the outer shelf of the northern California continental margin (McPhee-Shaw et al., 2004). The resuspension of sediments, picked up by currents flowing over the continental shelf off CA is known to be an important source of iron to surface waters (Johnson et al., 1999). Flocculants delivered to the wide continental shelf off of Oregon was similarly found to be an important capacitor and source of Fe to surface waters (Chase et al., 2007). Continental shelf width plays an important role in trapping settling material in coastal areas. Resuspension of those materials can spur production if upwelled to the surface, or be transported further into the open ocean. Lam et al. (2008) found that wintertime productivity at Ocean Station Papa in the North Pacific, 900 km from the closest coast, was spurred by particulate iron from the continental margin off the Aleutian Islands.

4.1.2 Study Area

In June 2017, we participated in the CCE-LTER process study (P1706) aboard the R/V Revelle which followed a strong filament of westward flowing water off the coast of California fueled by the movement of upwelled cold, high salinity water. The filament developed during the first week of June between 34-36°N and 124-120°W (Figure 4.5). In late May, cold water upwelled along the coast due to summer winds blowing North to South along the coast (Figure 4.5 A,B). By the first week of June, the recently upwelled water was flowing in a filament out into the Pacific (Figure 4.5 C,D). By mid-June, the end of the filament had developed into a cyclonic eddy, becoming pronounced by the end of June as evident in maps of sea surface height (Figure 4.14). CFEs were deployed at four locations along the filament (Figure 4.1), each location is discussed in detail in the results section. For reasons below, location 2 is further divided into location 2a and 2b.

4.2 Methods

4.2.1 Carbon Flux Explorer (CFE)

The CFE and the operation of its particle flux sensing OSR have been discussed in detail in Bishop et al. (2016). Briefly, once deployed, the CFE dives below the surface to obtain observations at target depths as it drifts with currents. The OSR wakes once the CFE has reached the target depth. On first wake-up of a given CFE dive, the sample stage is flushed with water and images of the particle-free stage are obtained. Particles settle through a 1-cm opening hexagonal celled baffle into a high-aspect ratio funnel assembly before landing

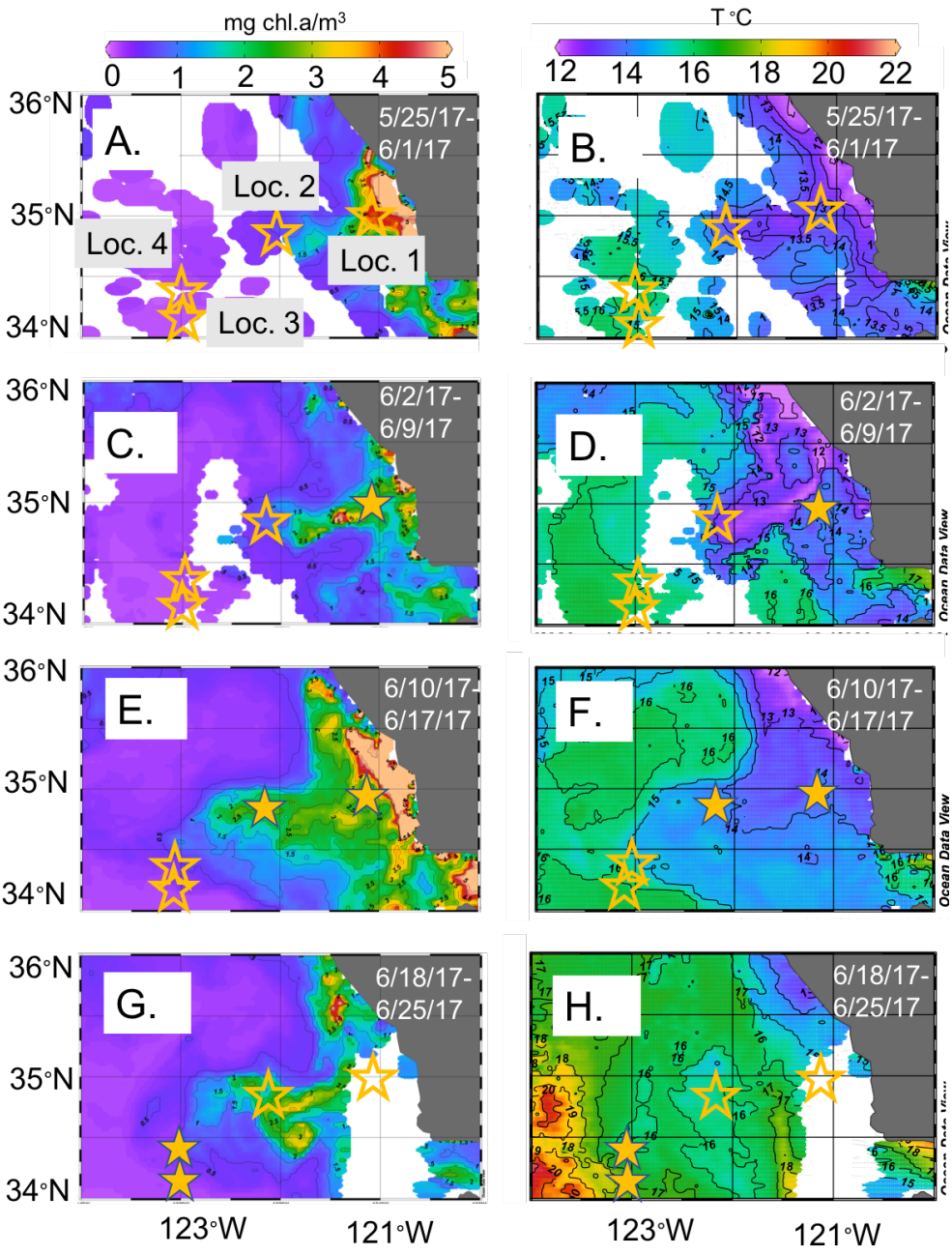

Figure 4.5: Surface chlorophyll evolving from late May to the end of June (A,C,E,G) and sea surface temperature over the same time period (B,D,F,H). All data is 8 day averaged 4 km resolution data from NASA Ocean Color from SNPP VIIRS. The stars represent the four locations. Stars are filled in maps from time periods during which sampling occurred.

on a 2.54 cm diameter glass sample stage. At 25-minute intervals, particles are imaged at

13 µm pixel resolution in three lighting modes: dark field, transmitted and transmitted-cross polarized.

We focus only transmitted light imagery in this paper because this data has been completely analyzed. Particles build up sequentially during the imaging cycle over 1.8 hours until after a predetermined number of images sets at which time another cleaning occurs and a new reference image set is obtained. After 6 h at a target depth, the OSR performs a final image set, cleaning cycle and reference image set, and the CFE surfaces to report GPS position, CTD profile data and OSR engineering data, and then dives again.

Two CFEs were built to collect calibration samples as described in chapter 3 and Bourne et al. (2018). These new CFEs were built with SOLO2 floats, unlike the older model CFEs which were built with SOLO1 floats. These two CFEs, referred to here as CFE-Cals 2 and 4, were always programmed to drift at 150m and were typically deployed for two 24-hour deployments at each location. We found that the concave bladder housing of the new SOLO2 float design trapped air and made it more difficult for the CFE to attain its target depth. Once we realized this issue, before each deployment, the bottom of the float was flushed with water prior to each deployment and care was made to launch the float horizontally to prevent this. Two other CFEs (1 and 3) were programmed to drift at three depths (referred to here as profiling CFEs). At offshore locations 2, 3 and 4 the three depths were 150, 250 and 500m. At location 1, the water column was only about 500m deep so the deepest the CFEs went was 300m. At location 3 outside the filament, one of these two profiling CFEs was attacked by a shark and destroyed. Locations 3 and 4 therefore only have images from 250 and 500m collected by one profiling CFE. The profiling CFEs were deployed at each location for 3 to 4 days.

4.2.2 OSR Transmitted Light Reduction

Transmitted light images were normalized by an in-situ composite image of the clean sample stage. Attenuance (ATN) values were then calculated by taking the -log10 of the normalized image. Pixels with an attenuance value less than 0.02 were defined to be background. Attenuance of pixels above the threshold value of 0.02 were integrated across the sample stage then divided by total number of pixels in the sample stage area to yield attenuance (ATN). As light decreases exponentially as it propagates through particles, attenuance is the best optical proxy for particle loading. ATN is then multiplied by 1000 to yield mATN. Figures 4.6, 4.7, 4.8 and 4.9 depict time series of sample attenuance with depth at the four different locations. Milli attenuance builds up over the course of an image cycle as more particles load onto the imaging stage; cleaning cycles remove particles and bring milli attenuance back down (Figure 4.6). Multiplying by the sample stage area gives sample Volume Attenuance (VA, units: mATN-cm^2).

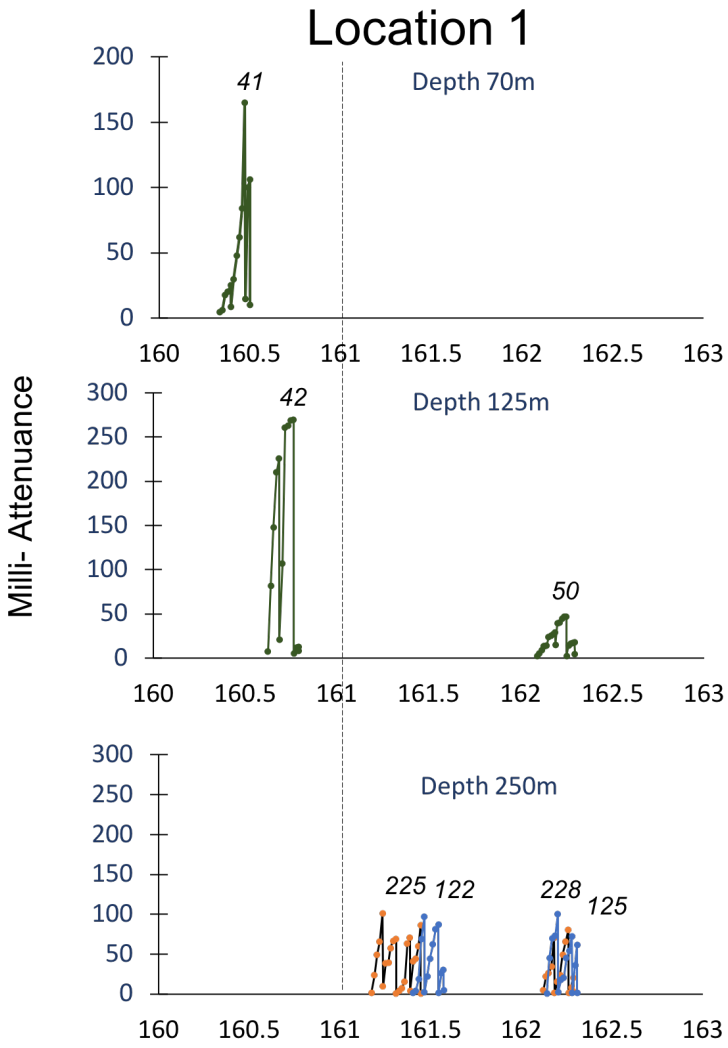

Figure 4.6: Raw attenuance time series for location 1. The depth intervals for location 1 shown here - 70, 125 and 250m are different than the intervals from the other location because the water column was only 500m deep at location 1 and CFEs did not reach their target depths at most dives. Orange marks with black lines represent data collected by CFE1, green marks with green lines are collected by CFE2, blue lines with blue dots represent CFE3 and red lines with red dots are CFE4. Dotted line through time series represents time when CFEs were redeployed in a new area within the same location. See figure 4.1 for details. Italicized numbers are the dive numbers corresponding to the data. The mATN timeseries scales with flux as timing is constant.

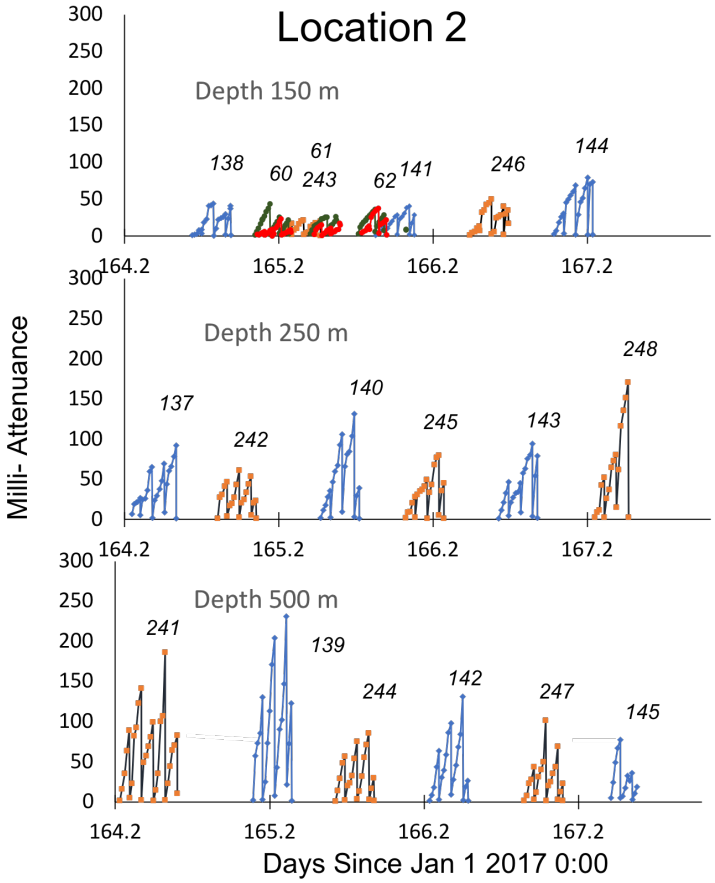

Figure 4.7: Raw attenuance time series for each location 2. Orange marks with black lines represent data collected by CFE1, green marks with green lines are collected by CFE2, blue lines with blue dots represent CFE3 and red lines with red dots are CFE4. See figure 1 for details. Italicized numbers are the dive numbers corresponding to the data. The mATN timeseries scales with flux as timing is constant.

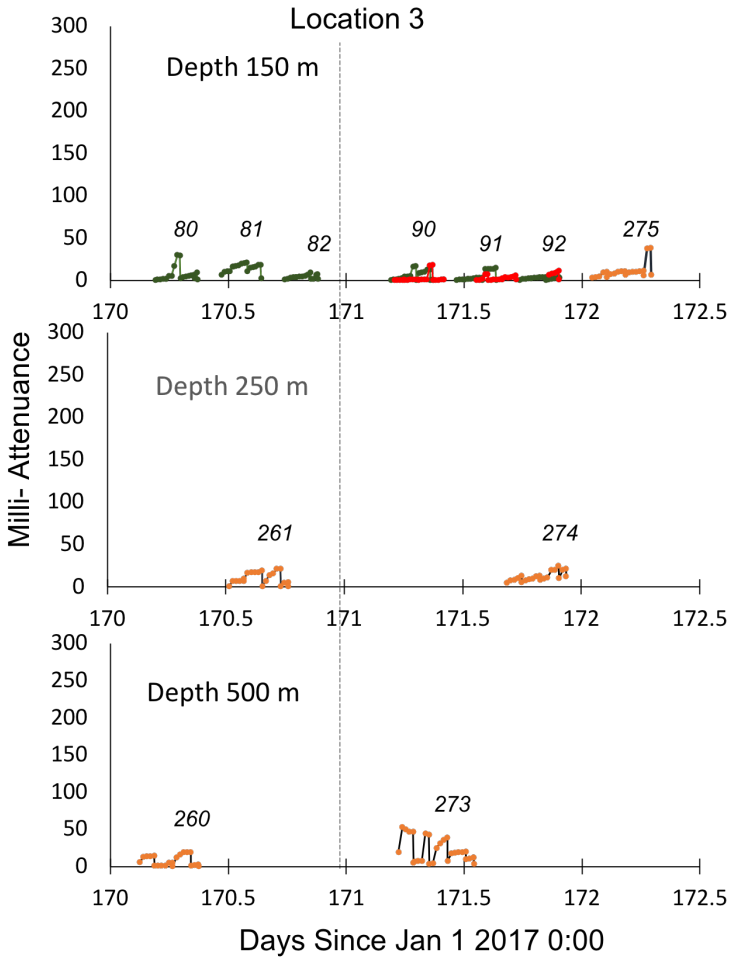

Figure 4.8: Raw attenuance time series for each location 3. Orange marks with black lines represent data collected by CFE1, green marks with green lines are collected by CFE2, blue lines with blue dots represent CFE3 and red lines with red dots are CFE4. Dotted line through time series represents time when CFEs were redeployed in a new area within the same location. See figure 1 for details. Italicized numbers are the dive numbers corresponding to the data. The mATN timeseries scales with flux as timing is constant.

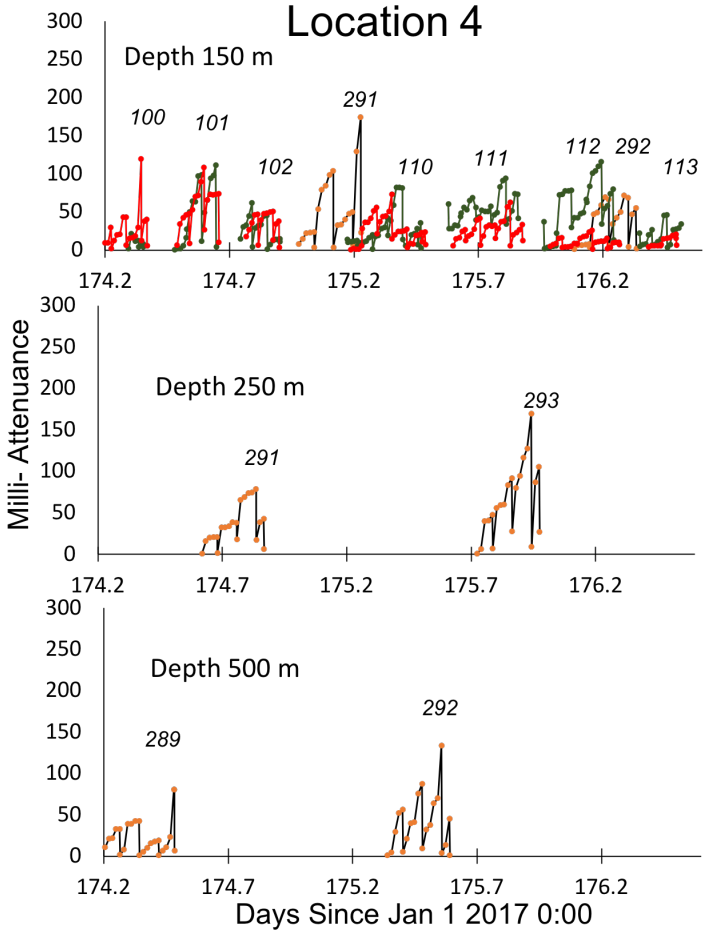

Figure 4.9: Raw attenuance time series for each location 4. Orange marks with black lines represent data collected by CFE1, green marks with green lines are collected by CFE2, blue lines with blue dots represent CFE3 and red lines with red dots are CFE4. See figure 1 for details. Italicized numbers are the dive numbers corresponding to the data. For CFE002, dive 111, the milli-attenuance does not go back to zero on cleaning because of the presence of a swimming jelly. The mATN timeseries scales with flux as timing is constant.

4.2.3 Calibration of POC_{ATN} to POC

VA was calibrated in terms of POC and PN flux, as detailed in Bourne et al (2018) and in the previous chapter. Briefly, during cleaning, imaged particles were directed to sample bottles. The sample bottles were then filtered and analyzed for carbon and nitrogen. Regressions of VA to POC and PN concentrations results yielded slopes of 10,066 mATN-cm^2: mmol POC (R^2 =0.86) and 100,500 mATN-cm^2: mmol PN (R^2 =0.87). The regression was found to be robust in all regimes sampled even though there were variations in total particle abundance and dominant size fractions at each location. There no obvious difference for VA:PN or VA:POC for samples collected from Locations 1 and 4 where large aggregates accounted for 95% of the flux compared to Locations 2 and 3 where smaller material contributed 50 and 30% of the flux, respectively.

4.2.4 Remote Sensing Data

Euphotic depth, sea surface temperature and sea surface chlorophyll data were downloaded from Nasa Ocean Color in 4 km, 8-day averaged resolution from the satellite VIIRS (Visible Infrared Imaging Radiometer Suite). Sea surface height data was downloaded from JPL with 1/6th of a degree, 5-day resolution. The sea surface height data combines measurements from a suite of sensors.

4.2.5 Hydrographic Profiles

Each day at the four locations, CTD profiles were typically taken at 2 AM, 11 AM and 6 PM local time in close proximity to a surface tethered drogued productivity array. Figure 4.11 shows average salinity, temperature and sigma-theta from each location. The profiles have been linearly interpolated for 1-meter resolution. The CTD was also equipped with a Seapoint fluorometer and scattering sensor, Wetlabs transmissometer, Particulate Inorganic Carbon (PIC) sensor and an underwater vision profiler (UVP5). One liter bottle samples from the CTD profiles were collected during the 2 AM and 11 AM casts each day for nutrient analysis. Nutrient data is also linearly interpolated and presented here (Figure 4.11). Current velocities were measured using an Acoustic Doppler Current Profiler. Velocities in u and v were averaged in 30 minute intervals during the time of CFE deployments. Velocities were also calculated based on CFE dive locations and times. Nutrient bottle data, CTD profiles and ADCP data can be found in the CCE LTER data repository (CCE-LTER data can be found at: https://oceaninformatics.ucsd.edu/datazoo/catalogs/ccelter/datasets).

4.2.6 Particle Size Distribution

Particles in each image were counted using a nearest neighbor algorithm. Particles were counted in the last image cycle before the imaging stage was cleaned off. Before particles in a given image were processed, each image was manually examined to ensure that there were few overlapping particles. If overlapping particles were present, the previous image in the

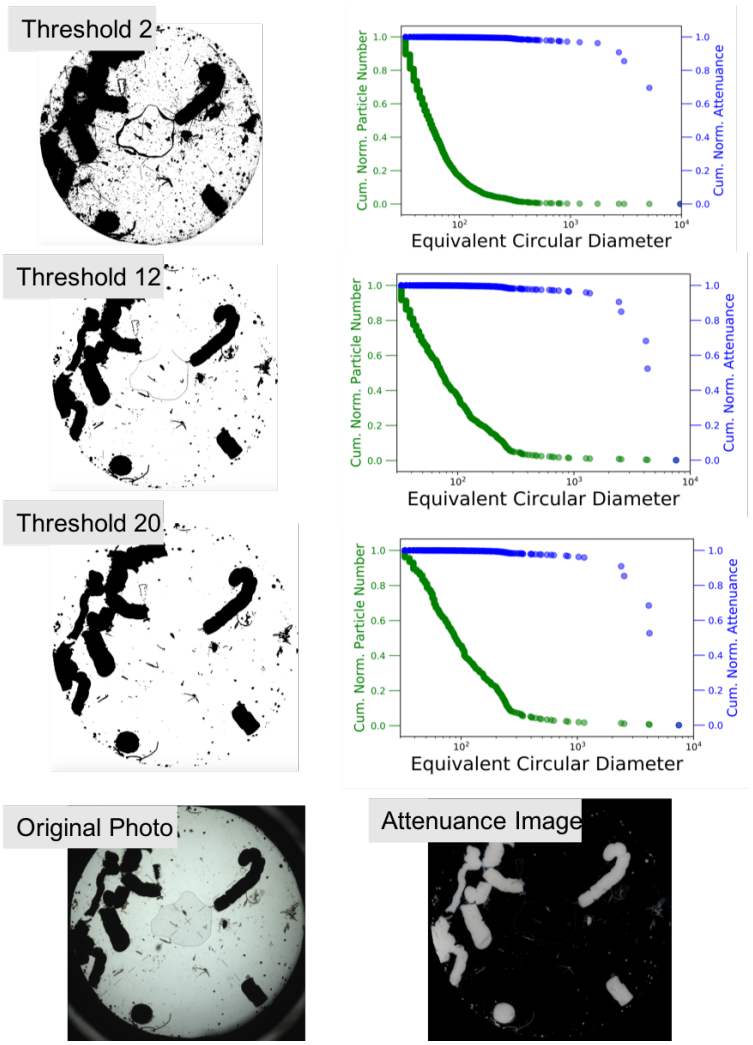

Figure 4.10: Sensitivity of attenuance and particle enumeration to threshold level. In order to find the best threshold, a number were tested. The best threshold was determined to be 12 as lower than that, some individual particles would blend together, and above that, actual particles could be removed from the image.

series would be used instead. In delimiting what pixels are included in particle counts versus background, one important step is choosing a limit of attenuance counts. This can greatly affect the number of particles in an image. The first step before thresholding in processing an attenuance image is to take an RGB bmp and convert it to a 16-bit grayscale image. In gray scaled attenuance images, pixel values range from 0 (black) to 255 (white). Choosing too low of a threshold can cause individual particles to meld together while choosing too high a threshold eliminates actual particles from being included. Too high a threshold can also cause a single aggregate to appear as separate particles. The best threshold was determined to be 12 (Figure 4.10).

4.3 Results

4.3.1 Hydrography

Location 1

Location 1 was closest to the coast of all locations. Water column depth was about 500 m. CFEs were deployed there between June 10th and 12th. During sampling at location 1, upwelling conditions were present, evident in the weak thermocline and halocline (Figure 4.11). The direction of water movement fluctuated with the tides, but overall, there was a net movement toward the southwest at a velocity of 0.06 m/s in the upper 50 m, and slightly slower at depth (0.02 m/s between 100 and 200m, 0.04 m/s between 200 and 300m). Figure 4.12A shows average velocities at location 1. Narrowband ADCP data was only available to about 400m.

The 24-hr mixed layer depth (MLD_{24}, defined by a potential density difference of 0.05 (Bishop and Wood, 2009), ranged from 13 to 25 m with an average of 19 m; slightly shallower than the euphotic zone depth (21m, Aqua Modis 8-day average data). The water conditions in the surface rapidly evolved with a community quickly growing on the high nutrients available. Between June 9th and 11th, dissolved nitrate levels in the mixed layer dropped from 10.2 to 5.4 µM.

Location 2

CFEs were deployed between June 14th and 17th at location 2. At location 2, the water-column had begun to stabilize and stratify as evident by the thermocline and halocline (Figure 4.5). The euphotic depth was slightly deeper (29m Aqua Modis) than the MLD_{24}, which ranged from 18 to 36 m, with an average of 26m.

At most locations, the free-floating CFEs drifted fairly close to locations of CTD profiles during deployments (Figure 4.1). However, at location 2, the CFEs were deployed in a fast-moving jet of water moving to the northwest, evident in their trajectory (Figure 4.1) and in

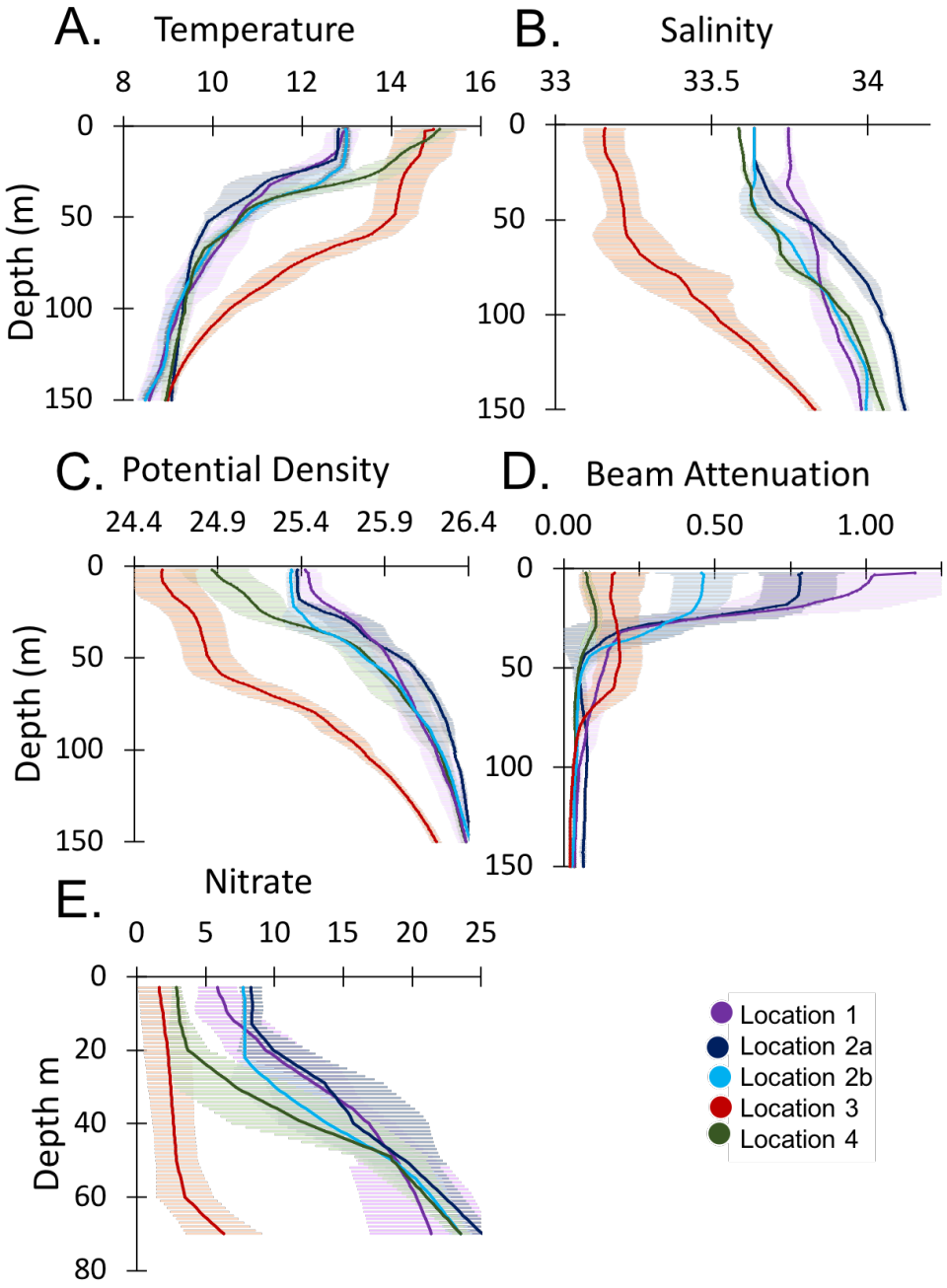

Figure 4.11: Average Temperature (A), Salinity (B), Potential Density (C), Beam Attenuation Coefficient (D) and Nitrate (E) for each location. Profiles have been linearly interpolated for 1 meter resolution. Error bars represent 1 sigma standard deviation of casts. POC concentrations in units of µM may be derived by multiplying beam attenuation coefficient by 27 (Bishop and Wood, 2009).

the strong velocity differences in the ADCP profiles between location 2a and 2b (Figure 4.12 B,C). Though the first several dives of the CFE were close to the first six CTD casts, after that they diverge. We treat the first 6 CTD casts as representative of CFE deployment 2a, and subsequent casts as 2b. Temperature and salinity measurements during the first six CTD casts at location 2 reveal a stronger halocline and pycnocline, with saltier, denser waters between about 25 and 150m than the following 6 casts, indicating upwelling. In figure 4.11, the hydrographic profiles for location 2 are therefore depicted as location 2a and location 2b. By 200m depth, the salinity and density of all locations begin to converge. Further rationale for the split was the concordance of the temperature and salinity data from the CFEs with the CTD's. The CFE-Cals, which were only deployed for 24-hour time periods, were originally deployed in the fast northwest moving water mass along with the profiling CFEs, however were redeployed in water near the productivity drifter.

During deployments at location 2a, there was a net movement toward the northwest at a velocity of 0.17 m/s in the upper 50 m, and faster at depth (0.29 m/s between 100 and 200m, 0.27 m/s between 200 and 300m). At location 2b, current direction was also to the northwest but velocities were lower at all depths (0.04 m/s upper 50m, 0.11 m/s between 100 and 200m, 0.12 m/s between 200 and 300m).

Location 3

Location 3 was located at the edge of the filament in transitional waters between the filament and oligotrophic offshore waters. CFEs were deployed here between June 19th and 22nd. The CFEs were deployed in two different spots at location 3. The second location, about 10km one day later to the southeast (Figure 4.1). The MLD_{24} at location 3 averaged 27m (range 11-69m). The euphotic zone was 77m deep at location 3 (NASA VIIRS). Dissolved nitrate was lowest at location 3. Average nitrate in the upper mixed layer was 1.6 µM, with a substantial decrease from the midday cast on June 19th (3.4 µM) to the midday cast on the 21st (0.1 µM). Current direction was to the southeast at location 3 with faster velocities in the upper 50m (0.30 m/s) compared to deeper waters (0.14 m/s between 100 and 200m, 0.08 m/s between 200 and 300m).

Location 4

Location 4 was located at the western edge of the filament (Figure 4.5 G,H). Based on the salinity signature of location 2b and location 4, the water masses were similar (Figure 4.11). By the time of deployment at location 4, between June 24th and 26th, the filament signature had begun to disappear, as can be seen in both surface chlorophyll as nutrients (Figure 4.5 g) were used up and SST had increased (Figure 4.5 h) due to solar heating. The 24-hr MLD

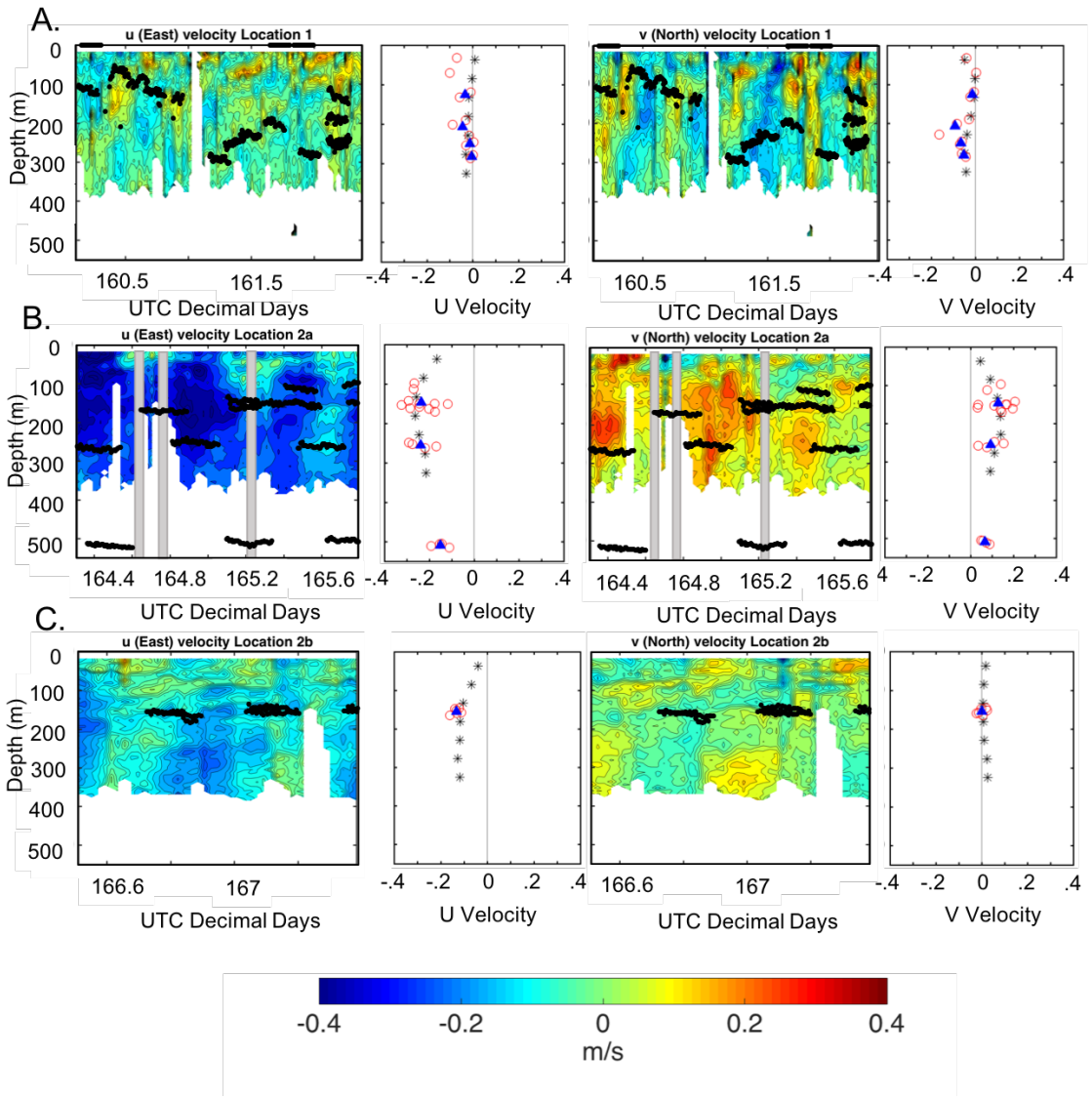

Figure 4.12: Average current velocities in u and v. Data in the contour plots has been averaged in 30 minute bins for clarity. The CFE depth locations are plotted over the contours. Data to right of contour plot shows average velocities measured by the ADCP over the entire time span represented with black astericks. Red points represent average CFE velocities over the course of a dive. Filled blue triangles are the averaged CFE velocities for all dives at a given depth. Averaged CFE velocities closely correspond to time averaged ADCP velocity, as expected for a lagrangian instrument. Part A, B, C, D and E represent Locations 1, 2a, 2b, 3 and 4 respectively

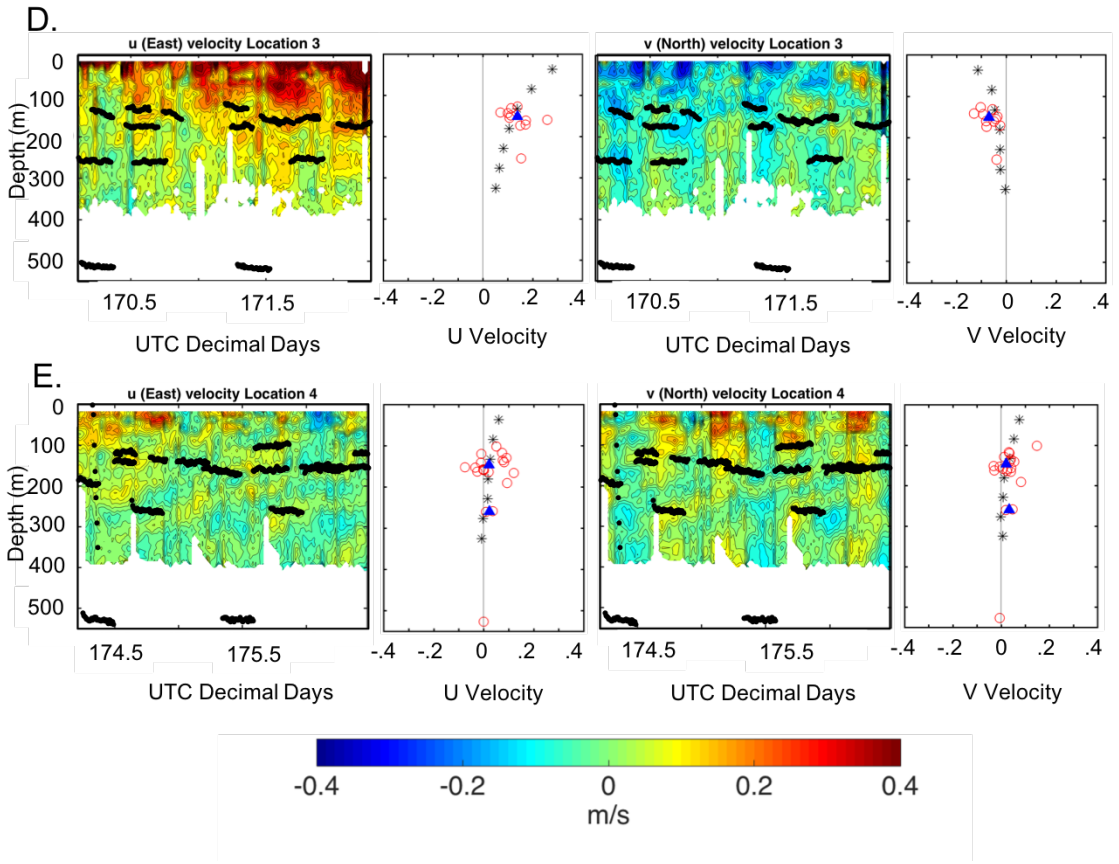

Figure 4.13: Continuation of figure 4.12. Average current velocities in u and v. Data in the contour plots has been averaged in 30 minute bins for clarity. The CFE depth locations are plotted over the contours. Data to right of contour plot shows average velocities measured by the ADCP over the entire time span represented black astericks. Red open circles represent average CFE velocities over the course of a dive. Filled blue triangles are the averaged CFE velocities for all dives at a given depth. Averaged CFE velocities closely correspond to time averaged ADCP velocity, as expected for a lagrangian instrument. Part A, B, C, D and E represent Locations 1, 2a, 2b, 3 and 4 respectively

ranged from 5 to 14 m with an average of 9m. Average nitrate in the $MLD_{24}$was 3.9 µM. Water moved slowly to the northeast at location 4 (0.11 m/s upper 50m, 0.04 m/s between 100 and 200m, 0.02 m/s between 200 and 300m).

Filament Evolution

Over the month of June, as the filament flowed west, interactions with inflowing offshore waters led to the development of a cyclonic eddy (Figure 4.14). Anti-cyclonic eddies formed

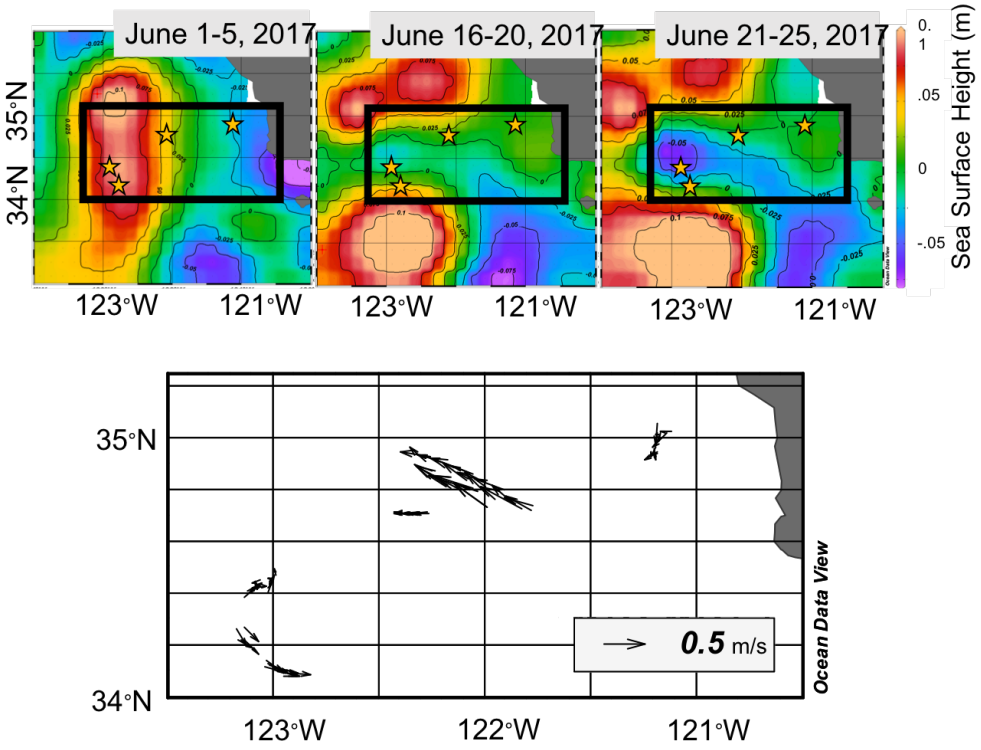

Figure 4.14: A. Average sea surface height from June 1-5, 16-20 and 21-25. In the beginning of June, sea surface height is low near the shore due to Ekman transport, and higher off the coast. As the filament develops and moves out to the west, a sea surface depression about 200 km offshore forms and is first apparent in the June 16-20 map, and deepens in the 21-25 map, indicating the formation of a cyclonic eddy. Anti-cyclonic eddies are present to the north and south. Stars represent positions of each location. B. Velocities of all CFE dives, from depths down to 500m. The CFE trajectories are fastest at locations 2 and 3, where the CFEs are deployed near the edges of the eddies and slowest at location 1, where overall velocity is affected by fluctuating tides, and at location 4, near the center of the eddy.

both to the north and south. At all locations, CFE trajectories matched ADCP velocities (Figure 4.12 and 4.13). The salinity properties of surface water (here defined as upper 20m) at locations 2 and 4 were a result of mixing of recently upwelled water with offshore water. Using location 1 as the upwelled water end member, and location 3 as the offshore water end member, mixture proportions for location 2 and 4 were calculated. Location 2a was a mixture of 81.1% upwelled water and 18.9% offshore water. Location 2b was a mixture of 80.9% upwelled water and 19.1% offshore water. Location 4 was 74% upwelled water and 26% offshore water. As the filament moved further offshore, the recently upwelled surface waters mix progressively more and more with with offshore water.

4.3.2 Export Variation with Location

The magnitude of flux at the four different locations varied greatly. The CFE-Cals were programmed to drift at 150m at all four locations, about 100m below the base of the euphotic zone. The dominant type of export at each location varied in the upper water column. Shallow export at location 1 and 2 was dominated by anchovy and copepod pellets respectively. At locations 3 and 4 further offshore, export was dominated at all depths by aggregates. Large aggregates resembling discarded larvacean houses were common at all sites 250m and below. Such aggregates were also present in samples closer to the surface, though not typically as abundant. Figures 4.16, 4.17, 4.18 and 4.19 shows representative images taken at the 4 different locations at the three depth intervals.

At location 1, export was high with a diverse assemblage of material, driven by large aggregates and anchovy fecal pellets. Previous research has found that on average, anchovy pellets contain about 22 µg of carbon (Saba and Steinberg, 2012). SEM analyses revealed that the anchovies were primarily grazing on diatoms (Figure 4.15). As anchovies grazed directly on primary producers with biogenic silica frustules, the large and dense fecal pellets subsequently produced were very efficient exporters of organic matter from the surface ocean into the deep ocean. Though greater than 90% of particles at 125 m at location 1 were less than 300 µm in diameter, particles greater than 1mm in scale carried 90% of particle loading (Figure 4.16).

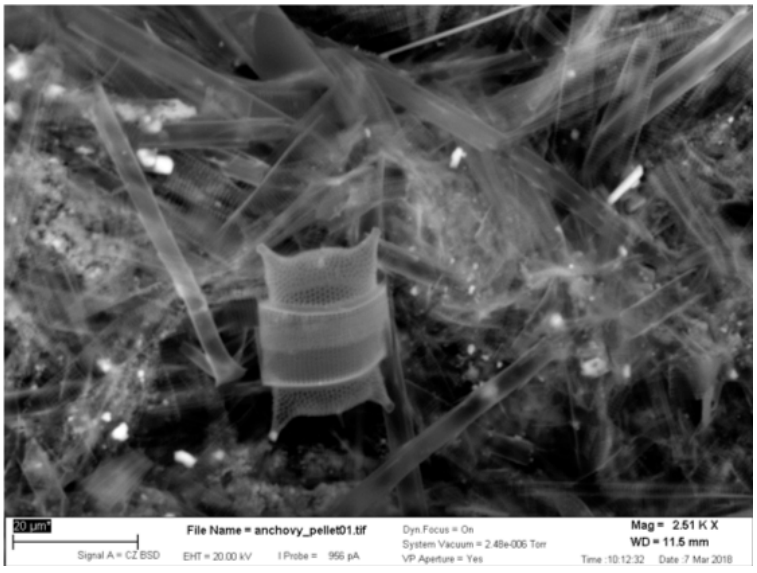

Figure 4.15: SEM image of anchovy fecal pellet. Contains mostly diatom frustules.

Flux at 150m at location 2 was dominated by small ovoid pellets olive in color and about 100-300 µm in diameter. These ovoid pellets were incredibly abundant and fell into the OSR at 150m at a rate of 2.5 ± 1.2 per minute. Particles less than 1 mm at location 2 accounted for 98% of all particles and 40% of particle loading, while particles less than 1mm at location

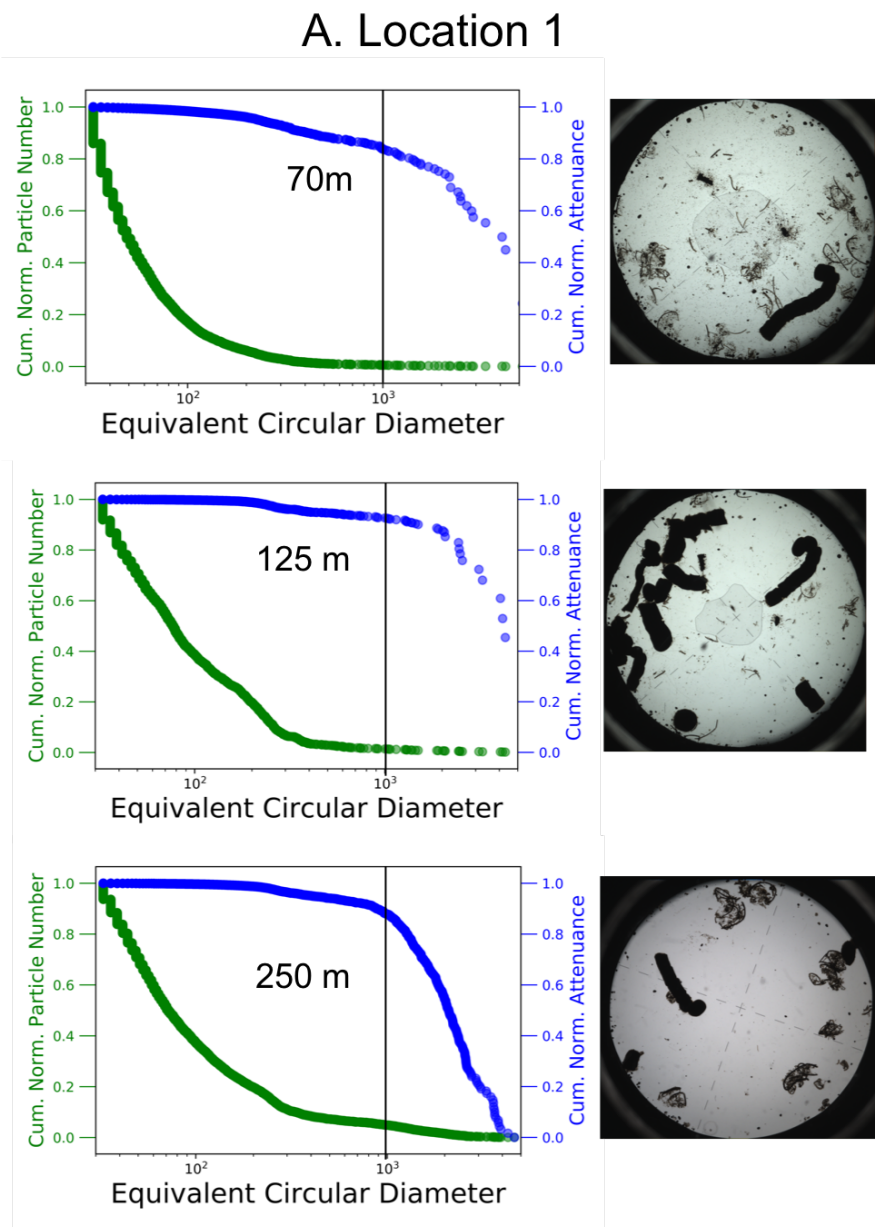

Figure 4.16: Size distribution with depth. Right hand side of the axis is cumulative normalized particle distribution. The majority of particles at all sites and depth are small. The left side of the axis represents cumulative normalized attenuance. Images on the right hand side are representative images at each location and depth.

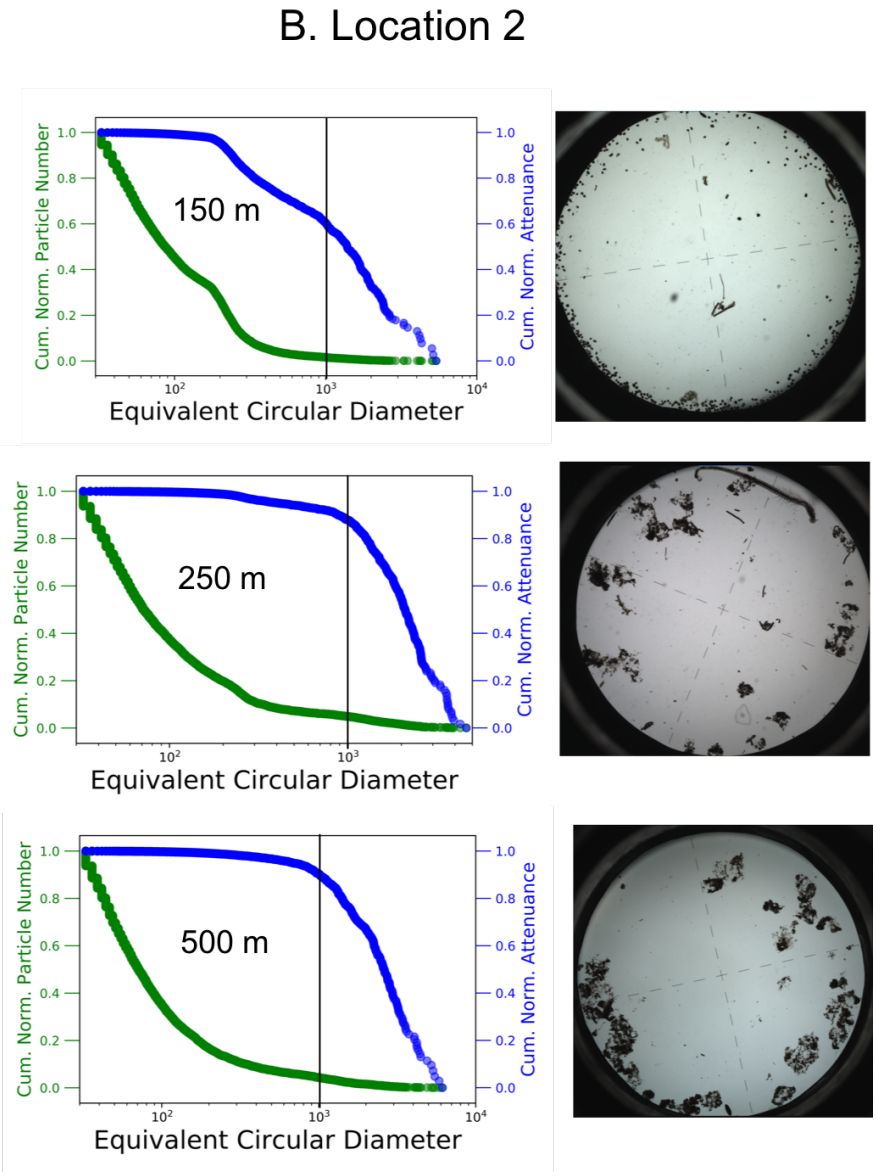

Figure 4.17: Size distribution with depth. Panels same as for figure 4.16

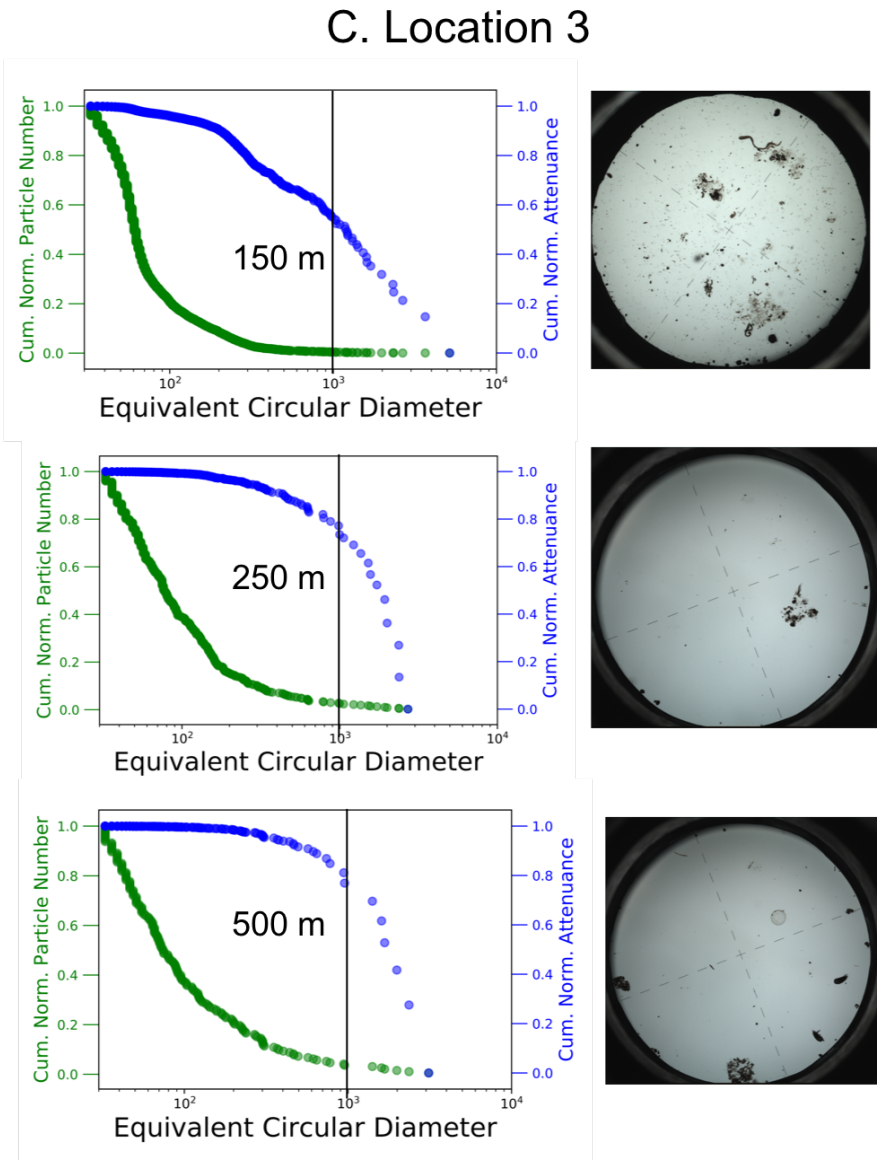

Figure 4.18: Size distribution with depth. Panels same as for figure 4.16

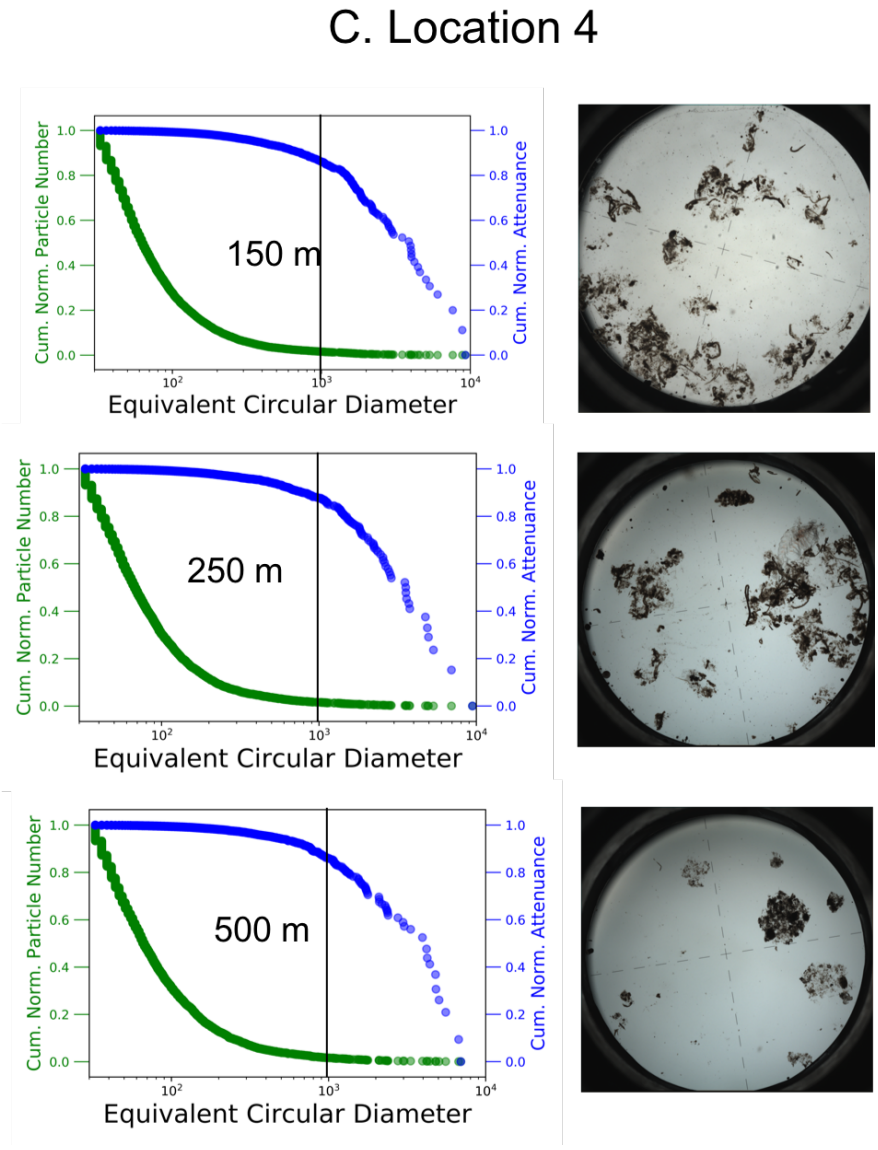

Figure 4.19: Size distribution with depth. Panels same as for figure 4.16

1 only accounted for about 7% of particle loading (Figure 4.17). At location 3, export was low overall and dominated by marine snow. At location 3, most particles at 150m were small (90% less than 300 um diameter), however several large aggregates >1 mm in diameter carried the majority of the particle loading. Flux at 150m at location 4 was dominated by large aggregates. Aggregates > 1mm carried about 80% of the particle load at location 4 (Figure 4.19).

Flux at 150m at location 2, averaged 9.6 mmol C m^{-2} d^{-1} and ranged from of 5.0-16.9 (Figure 4.23). Export at location 3 was also the lowest of any location, with an average of 3.0, and ranged from 1.1-5.9 mmol C m^{-2} d^{-1}. Though surface nitrate was relatively low at location 4, flux at 150m was relatively high with an average of 16.4 mmol C m^{-2} d^{-1}, range 4.4-31.2 mmol C m^{-2} d^{-1}.

4.3.3 Particle Export Profiles

Interestingly, none of the locations showed a decrease of flux with depth as one would expect if flux behaved following the traditional Martin curve (Figure 4.20). Flux at locations 1 and 4 remain little changed with depth while at locations 2 and 3, flux increased with depth. The trends at all sites are drastically different from the classic Martin curve where export rapidly attenuates with depth (Martin et al., 1987).

Flux at location 2 dramatically increased with depth (Figure 4.20). Flux at around 150m averaged about 9.2 mATN cm^2 cm^{-2} d^{-1} . By 250m, flux had more than doubled to 26.2 mATN cm^2 cm^{-2} d^{-1}. Flux at 500m was quadruple the flux at 150 m with about 37 mATN cm^2 cm^{-2} d^{-1} (Figure 4.20). The size of the particles also changed with depth. In the 150m results, small particles contribute about equally to flux as particles greater than 1 mm (Figure 4.21). By 250m, flux was dominated by large aggregates, with little contribution from small particles.

At location 3, in transitional waters outside the filament, flux also increased with depth. VAF at 150m (about 100m below the euphotic zone) was 2.91 mATN cm^2 cm^{-2} d^{-1} (average VAF at 143 and 167m). By 230m the flux is about 5 mATN cm^2 cm^{-2} d^{-1} and at 515m the flux is almost 7 mATN cm^2 cm^{-2} d^{-1}.

At all locations, the attenuance flux of >1mm sized aggregates increased with depth (Figure 4.16). By 500m, the majority of attenuance was carried by a relatively small number of large aggregate particles at all locations, though the number flux was dominated by particles less than 300 µm in Equivalent Circular Diameter (ECD).

This was especially pronounced at location two. At 150m, flux was carried almost equally by small and large particles, yet by 500m, flux was dominated by large aggregates (Figure 4.21a). These aggregates were up to several mm in diameter.

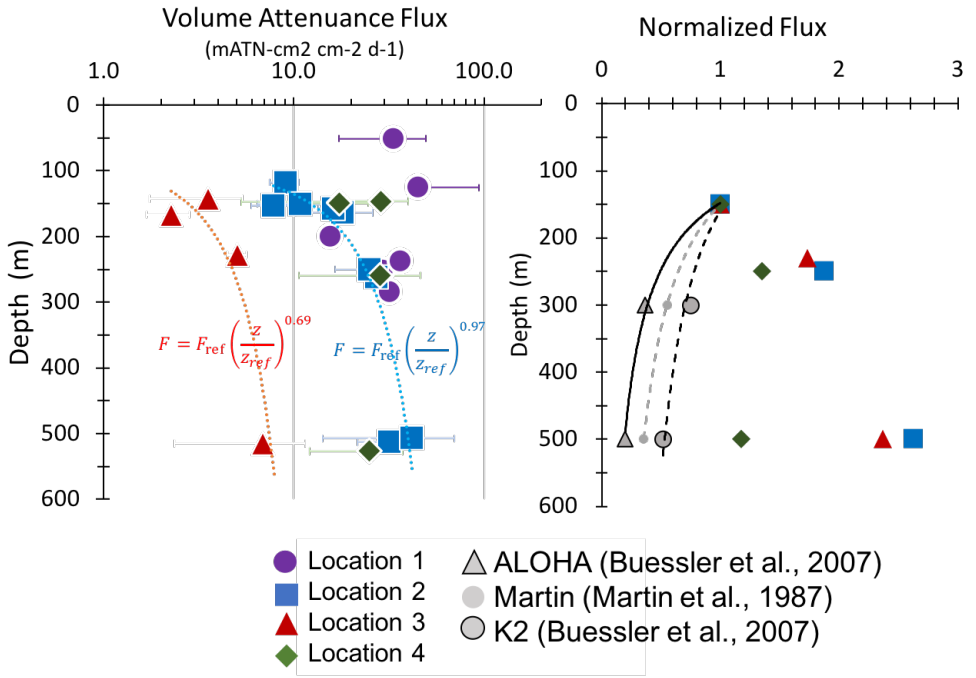

Figure 4.20: Volume attenuance flux at each location. At location 1 and 4, export is nearly constant with depth and at cycle 2 and 3, export levels increase with depth. Martin curve fits have b values of 0.97 and 0.69 for locations 2 and 3 respectfully.

4.3.4 Water Column POC

Transmissometers, which measure beam attenuation, can be used to quantitatively estimate POC in the water column (Bishop, 1999). Beam attenuation is strongly correlated to POC in the water column. Between 41 and 89% of this signal is typically due to beam interaction with small, non-sinking particles (Chung et al., 1996). POC concentration can be calculated by multiplying the beam attenuation coefficient by a factor of 27 (Bishop and Wood, 2009). Surface water POC ranged from an average of 2.4 µM at location 4 to 25.4 µM at location 1.

The integrated standing stock of POC in the water column is highest at location 1 and progressively drops with distance off shore (Figure 4.22). At location 1, where the sea floor was about 500m below the surface, relatively high levels of POC as measured by the transmissometer can be seen 100m above the seafloor, indicative of resuspended particles forming a bottom nephloid layer.

Average integrated POC from the surface to 450m between June 10th and 12th at location 1 is 1149 mmol m^{-2}. Moving to location 2a in the filament on June 14th and 15th, beam attenuation drops to 1007 mmol C m^{-2} indicating a loss of 47 mmol C m^{-2} d^{-1} from the water column.

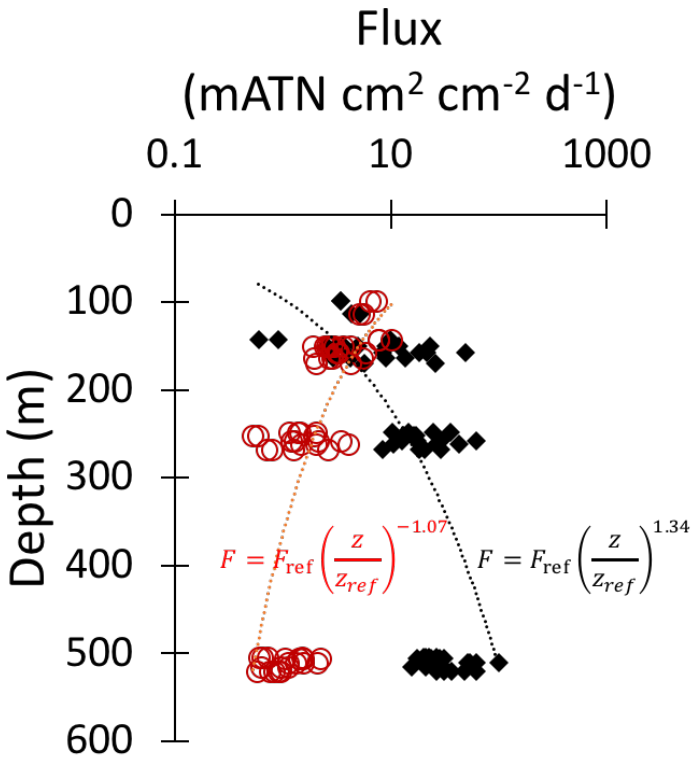

Figure 4.21: Flux of small (red) vs large (black) particles with depth at location 2. Small particle flux does decrease with depth whereas large particle flux (>1mm) increases with depth. Martin curve fits have b values of -1.07 and 1.34 for small and large particles respectfully.

4.3.5 Surface Export

In this study, CFEs were programmed to dive no shallower than 150m. Here we use nutrient and beam attenuation coefficient to estimate shallow export. We did this using data from location 2 and location 4. Based on salinity profiles, the water masses encountered in the later part of occupation at location 2 were of similar origin to the water mass encountered at cycle 4 seven days after departing location 2. Though salinity remained similar between these two locations, surface water nitrate had been drawn down by about 5 µM in the upper 20 m (Figure 4.11).

Following Johnson et al. (2017), we calculate export by integrating nitrate drawdown from surface waters and then convert to carbon using a ratio of C:NO_3^-. Johnson et al. (2017) uses the Redfield ratio of 6.6 C/NO_3^-, however, based on values published for C/N values in the area, we use a ratio of 6.4 (Stukel et al., 2013). An integration depth of 45 m was chosen as dissolved nitrate levels from the two sites converge at this depth. Subtracting integrated nitrate at location 4 from location 2b indicates an average export of 111.3 mmol

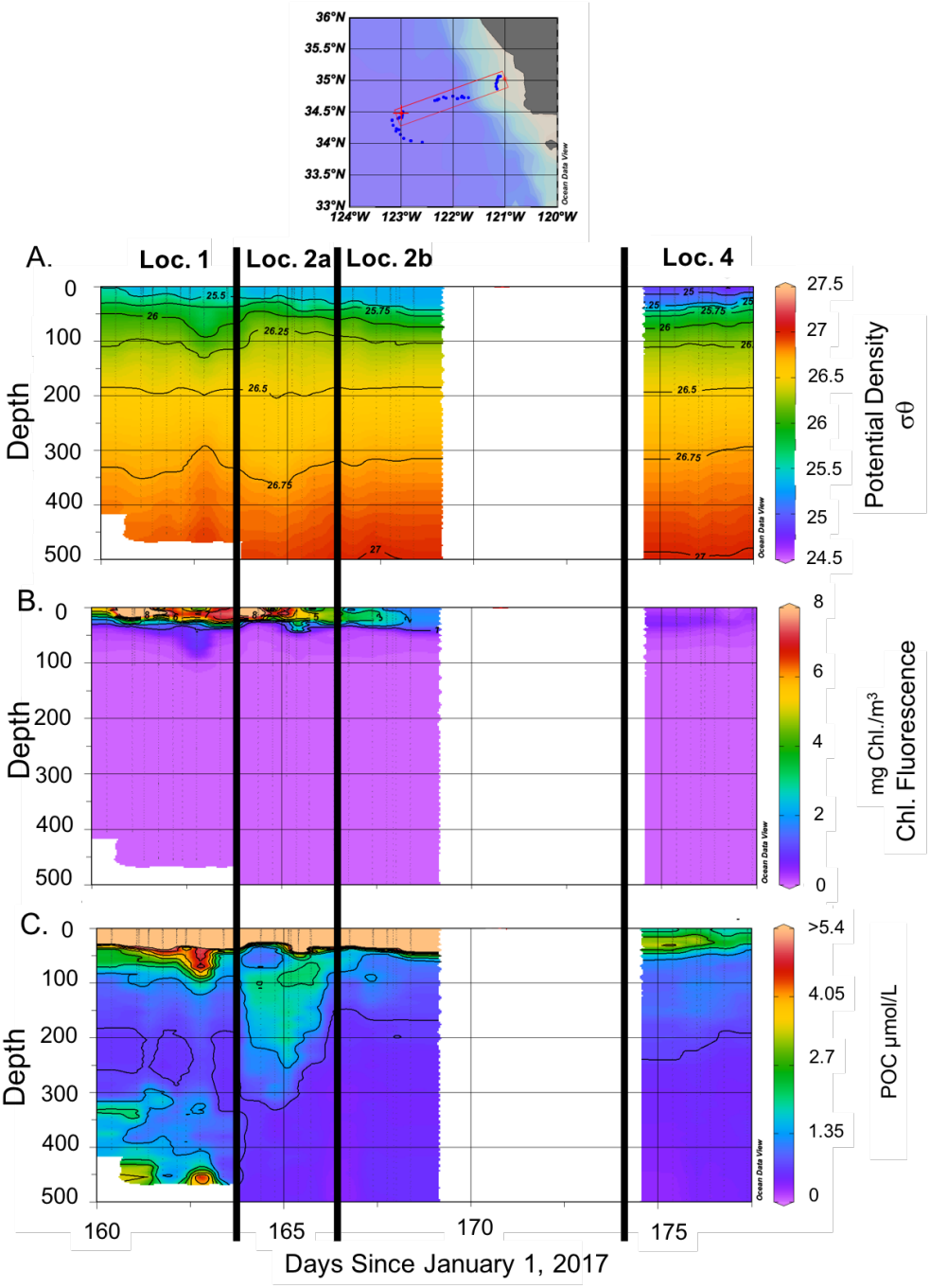

Figure 4.22: Transects along filament of potential density (a), chlorophyll fluorescence(b) and non-sinking POC (c). The bottom at location 1 is about 500m. At location 2 and 4 it is greater than 2000m deep. Vertical black lines separate the four locations.

C m^{-2} (standard deviation 32.2 mmol C m^{-2} d^{-1}) over 9 days. Integrating POC measured using the transmissometer from the surface to 45 meters at the two sites gives us an estimate of the net loss of small particles. Subtracting integrated POC at location 4 from location 2b indicates a further loss of 33 mmol C m^{-2} d^{-1}, therefore giving a total estimated export of about 144 mmol C m^{-2} d^{-1}. This calculation allows for an estimate of how much material was exported from the euphotic zone which can then be compared to export measured at depth.

4.4 Discussion

4.4.1 Circulation

When considering carbon export dynamics, especially in regions with strong current systems, it is essential to understand the vertical profile in the context of the physical environment. As mentioned previously, by June 20-25th, a depression in SSH roughly 100 km in diameter had developed about 200 km off the coast. Such an SSH depression indicates the formation of a cyclonic eddy as Ekman transport would yield a net transport out of the center to the edge of the eddy as waters rotate clockwise around the center. As CFEs are lagrangian, they drift with currents at depth during deployments, and their positions over time can be used to infer current velocity. The CFE trajectories of dives deployed from 150 to 250m all reinforce such counterclockwise motion, consistent with ADCP data (Figure 4.14). Water on the shelf at location 1 was affected by tidal motion but overall flowed offshore to the west. By location 2, the water was flowing quickly to the northwest. As this westward flowing water encountered offshore water flowing eastward, the cyclonic eddy formed, with anticyclonic eddies forming to the north and south. Location 3 was located outside of the cyclonic eddy, moving quickly to the south east. Location 4 was in slow moving waters close to the center of the eddy. These large-scale circulation patterns, with consistent directionality of water flow encountered by CFEs at all depths has implications for the flux profiles as discussed in depth below.

4.4.2 Comparison to Previous Studies

Siegel et al. (2014) estimated algal aggregates and zooplankton fecal matter export at the base of the euphotic zone from a food web model driven by satellite observations including SST, chlorophyll a concentration, net primary productivity and particle size spectrums for monthly climatological conditions. Using Siegel et al. (2014)'s modeled data, we reproduce climatological flux for our region in June (Figure 4.23). Siegel et al.'s model predicts a flux of about 20 mmol C m^{-2} d^{-1} near-shore with progressively lower fluxes further off shore to about 5 mmol C m^{-2} d^{-1} near offshore location 3. In order to compare CFE flux results at 150m and 250m, these modeled euphotic zone export magnitudes were extrapolated to 150 and 250m using equation 4.1, using a b value of -0.83 from the Martin et al. (1987) VERTEX I site (Figure 4.23).

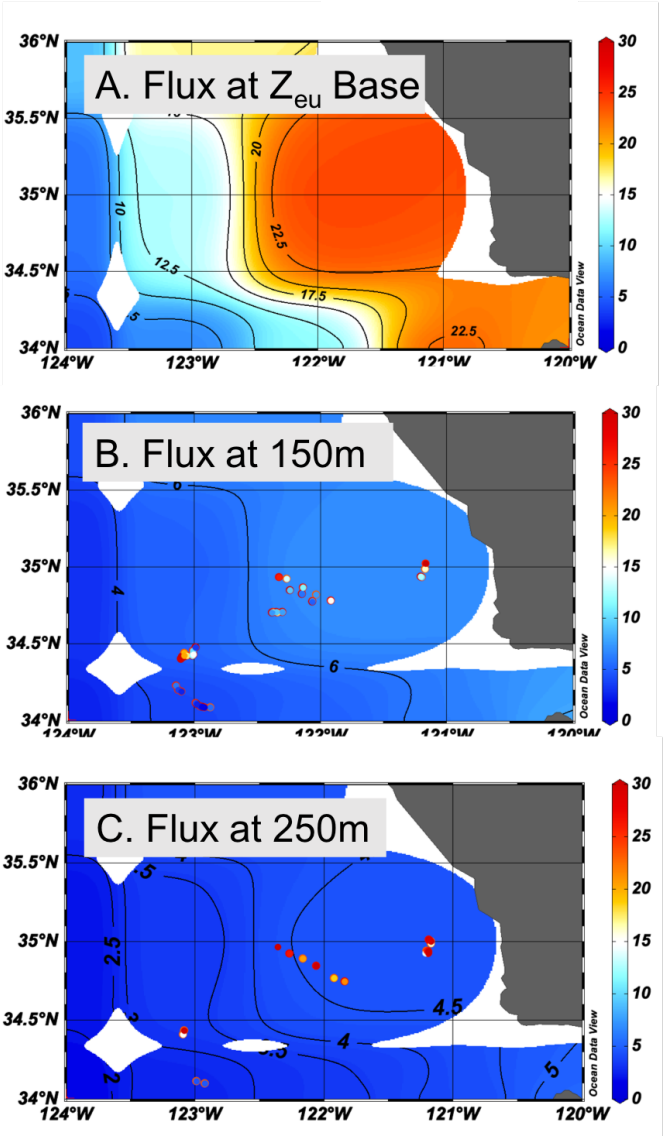

Figure 4.23: (A) Carbon flux for June climatology predicted by model in Siegel et al., 2014 (B) Extrapolating flux from Siegel et al., 2014 down to 150m using equation 4.1. The b value found at the nearby VERTEX I location (-0.83) was used (Martin et al., 1987). The euphotic zone base depth (Z_{eu}) used was June climatology data from NASA VIIRS (https://oceancolor.gsfc.nasa.gov/l3/order/) The contour plot is overlain by CFE flux data collected between 100 and 200m. (C) Carbon flux extrapolated down to 250m using the same method. The contour plot is overlain by CFE flux data collected between 200 and 300m.

One of the closest observations in terms of distance and season to measure fluxes down below 500m at this location was VERTEX station 1 reported in the classic Martin et al. (1987) study. Martin's station 1 was located off the coast of Point Sur at the same longitude as location 2 and just 1-degree further north. Measurements were made using surface tethered PIT sediment traps in June 1984 during relatively similar conditions, with intensive upwelling conditions leading to a plankton bloom and a euphotic zone about 50m. At 100m, Martin et al. (1987) measured a flux of 19.4 mmol C m^{-2} d^{-1}. In our deployments at location 1, there were three dives near 100m (average 107m, SD 32m). Average flux from these dives was 43.1 mmol C m^{-2} d^{-1} (SD 33.6). The reason for the high variability in flux measurements is that there was heavy anchovy fecal presence in the first dives. When the CFEs were redeployed several km South one day later, flux was much lower. Flux was higher in our observations, though within one SD of the VERTEX 1 location. Though fluxes observed at the two sites were relatively similar at 100m, the profile of flux with depth at these two sites was quite different. Flux at location 1 was relatively constant with depth and flux at location 2 increased with depth, whereas the flux at VERTEX station 1 attenuated quickly following the power law function shown in equation 1 with a b value of -0.83.

We can think of two reasons why two flux profiles taken in similar conditions in close proximity exhibit such different behaviors. First, our location 1 was located over a wide region of the continental shelf and location 2 offshore, down current of this feature, whereas the VERTEX location 1 off Point Sur is offshore from a much narrower shelf. The Martin et al. study was made 68 km off the coast, whereas location 1 in this study was 114 km off the coast. While our location was further offshore, location 1 was only 500m deep, still on the continental slope, whereas the VERTEX 1 site was in water >3km. When high export occurs over a broad shelf, particles can be resuspended in a nephloid layer that through lateral transport can be moved out into the open ocean. Such a layer can clearly be seen at location 1 (Figure 4.22 C). Another possibility is that many of the large aggregates seen at 250m and below are greater than 1mm; surface tethered traps may miss many such aggregates due to horizontal forces over the top of the trap especially when currents are faster than 0.02 m/s (Bishop et al., 2016). As currents were generally above this threshold and smaller particles at location 2 did attenuate with depth, while aggregate concentrations increased (Figure 4.21), there is support for this hypothesis.

4.4.3 Mechanisms for Efficient Export

In many areas of the ocean, especially the open ocean, flux observations can be fit with a power law function (Martin et al., 1987; Bishop, 1989; Buessler et al., 2007; Marsay et al., 2015). However, in dynamic coastal environments, there are many cases in which flux does not ascribe to an attenuation model. A number of studies in eastern boundary currents have found flux in the twilight zone to be either stable or increasing with depth (Bishop et al., 2016; González et al., 2000). Below, we return to the mechanisms of efficient export

described in the introduction and explore how they may or may not affect the flux profiles found at our four locations.

Efficiency of Grazing Community and Active Transport

Some heterotrophs produce fecal material that is much more efficient at being exported from the euphotic zone. Organisms such as krill and fish produce large dense fecal pellets which sink very efficiently. At location 1, the stable export with depth was due in large part to anchovy pellets sinking quickly. Saba and Steinburg (2012) found that similarly sized anchovy pellets sank on average greater than 750m in one day. Some organisms, such as copepods produce pellets that do not sink as well. It has been well reported that both copepod (Smetacek, 1980; Krause, 1981; Bathmann et al., 1987, Gonzalez et al., 2000) and protozoan (Gonzalez, 1992b; Beaumont et al., 2002) pellets do not always sink out of the surface zone. Gonzalez (2000) found only 0.1-2.5% of copepod fecal pellets in the upper 100m Humboldt current reached sediment traps at 300m. The fast recycling of copepod and oval pellets in the surface has been attributed primarily to coprophagy, the process by which zooplankton eat other zooplankton's feces (Beaumont et al., 2002; Smetacek, 1980). Evidence suggests that the fast recycling of zooplankton pellets in the epipelagic is due to the activities of other zooplankton (Turner, 2015 and references therein). There are a number of zooplankton known to eat other zooplankton's feces (coprophagy) including radiolarians (Gowing et al., 1989), tunicates (Pomeroy et al., 1984) and copepods (Sasaki et al., 1988).

At location 2 at 150m, small ovoid pellets were incredibly abundant. At 150m, these ovoid pellets were falling into the trap at a rate of 2.5 $\pm$1.2 per minute. However, by 250 m, the pellets were almost completely absent. The membrane-bound small ovoid pellets 100-300 µm in ECD were olive green in color and full of diatom frustules. As the ovoid pellets decreased with depth, the concentration of aggregates, many of which closely resemble discarded larvacean houses began to dominate export (Figure 4.21). Larvaceans produce fine mucous feeding webs that concentrate and ingest particles from 0.2 to 30 µm in diameter (Gorsky and Fenaux, 1998). Typically, a larvacean feeds on only a fraction of the material in their web before it discards it due to clogging (Berline et al., 2011). Some larvaceans create and discard up to 26 feeding webs a day. They therefore can be great contributors to carbon flux. Larvaceans can be found throughout the upper 1000 m (Stemmann et al., 2008). Larvaceans are often the most abundant mesozooplankton after copepods (Gorsky and Fenaux, 1998). In many food web models, the mesozooplankton component typically lumps all mesozooplankton together and is more parameterized towards representing copepods (Berline et al., 2011). Larvaceans are difficult to study as they are fragile, and therefore difficult to capture in either plankton nets or tethered sediment traps as they are prone to break (Berline et al., 2011; Silver et al., 1998). Because their discarded houses are greater than a mm, hydrodynamic biases may prevent their collection in surface tethered baffled sediment traps (Bishop et al., 2016).

Vertical migration likely does contribute export to depth. However, the increase of flux with depth cannot solely be explained through transport of material from the surface to depth through vertical migration. For one, vertically migrating crustacean species in the CCE have a gut turn over time of about 30 minutes, not long enough to swim to depth and then excrete material to 250 or 500 m, where we see increased flux. Furthermore, we saw no evidence of migration in the acoustic backscatter ADCP data that would indicate strong diel migration. This does not rule out that vertical migrators were present, as gelatinous organisms such as larvaceans and salps have been known to migrate daily, yet do not scatter sound waves.

Typically, metabolic processes use about 90% of food consumed, passing on only about 10% of material on. Assimilation efficiency can vary by species and prey type however. Previous work has reported that salps have only only a 61% assimilation efficiency for carbon (Madin and Purcell, 1992). Earlier, we calculated an average surface export of 144 mmol C m^{-2} d^{-1} at location 4. Even if this material were all consumed by vertically migrating organisms and excreted at depth, assuming an assimilation efficiency of 90%, this would add 14 mmol C m^{-2} d^{-1} to depth while average export at 500 m at location 4 is 36.3 mmol C m^{-2} d^{-1} . Therefore, while the community of grazers present, and vertical migrators, are likely important contributors to flux, their activities do not fully explain the depth increasing flux profiles observed.

Non-Steady State Flux (M2)

Non-steady state blooms and time variable changes of b factor can lead to inverted Martin curves as there is a temporal lag between peak biomass at the surface and peak flux to depth as particles take time to settle. One indicator of temporal delay would be slowly sinking ungrazed intact phytoplankton from the remains of a bloom seen at depth. Chlorophyll fluorescence data measured by a fluorometer on the CTD show no evidence of sinking ungrazed phytoplankton (Figure 4.22). There is also no significant trend of flux either increasing or decreasing with time (Figure 4.6).

Physical Subduction (M3)

It is unlikely that subduction substantially contributed to the apparent flux increases with seen in our CFEs. Isopycnals did slope down as denser upwelled water subducted beneath warmer less salty off shore water as the filament moved west (Figure 4.14). However, this large-scale feature only dipped to about 50 m, far higher than the depth at which our shallowest CFE collected particles. Furthermore, Stukel et al. (2018) found that in the CCE, subducted particles were primarily remineralized by 150m, too shallow to contribute to the high flux signal we observe deeper in the water column.

Eddy features can play an important role in the subduction of particles. Anticyclonic eddies push water toward the center, forming a dome at the center of which downwelling occurs. However, the filament we followed produced a cyclonic eddy whereby water was pushed to the edges, leaving a depression in the middle which would have led to upwelling, not downwelling. Eddy subduction therefore did not play a role in fluxes seen in our data.

Lateral Advection (M4)

Kelly et al. (2018) found an inverse relationship with higher e-ratios (export at euphotic zone base/NPP) in offshore regions and lower e-ratios in the more productive coastal regions over 5 CCE cruises. Furthermore, a strong correlation between sea surface temperature and export was found, which they determined not to be causal, but rather an effect of lateral advection bringing upwelled, cold productive waters offshore.

Lateral transport was likely a factor in export in our study. There were strong currents moving westward off the coast between the surface and 400m during the time of our deployments at location 2. During the first two days of the CFEs deployment, these currents moved rapidly to the northwest, with velocities on average about 0.2 m/s between 100 and 300 m. The narrow band ADCP data only resolved current speeds to about 350 m, however, CFE trajectories during 500m deployments indicate that deeper water was also moving in the same direction (Figure 4.12, 4.13). The offshore flowing currents, coupled with a high concentration of non-sinking POC over the continental slope at location 1 suggests that material was being laterally transported offshore.

Location 2a was only about 50 km from location 1 and about 30 km from the continental shelf 500m bathymetry contour. Though we did not measure sinking speeds of aggregates, the sinking rates for similarly sized aggregates and discarded larvacean houses measured in Hansen et al. (1996) was 120 m/d. Average current speeds in the region were between 0.1 and 0.2 m/s, meaning that in one day a typical large aggregate would travel 120 m vertically and between 9-17 km horizontally. Using these estimates, it does seem likely that aggregates originating from the continental shelf could be transported offshore, helping to explain the increase of flux with depth observed at location 2. While it seems likely that both active transport (M1) and lateral advection (M4) play a role in the flux profiles observed, more work is necessary to understand each mechanisms' contribution.

ATN:POC with Depth (M4)

Though volume attenuance flux increases with depth (Figure 4.20), it may be that carbon does not increase with depth at the same magnitude. We did not deploy the CFE-Cals below 150 m, so we do not have calibration samples for samples taken at 250 m and 500 m. Because

samples collected at 150 m covered a wide range of size distribution and particle types, the POC:ATN ratio likely does not decrease significantly. Furthermore, Estapa et al. (2017), did calibrate POC:ATN using a transmissometer at different depth intervals and found that all samples plotted on the same slope. Large particles sampled by in-situ filtration show that there is little shift in $\%C_{org}$ below the euphotic zone depth down to 500m (Bishop et al., 1986). This is, however, an important caveat in our results. In the future, CFE-Cals will be deployed to 500 m to gain a better understanding into the relationship of POC:ATN with depth.

4.5 Conclusions

Coastal upwelling regions are disproportionately productive relative to their total surface area due to high levels of available nutrients. We found that flux in the California Current off Point Conception does not decrease with depth following a power law function. Extrapolating flux to depth using a power law function in regions with strong currents potentially misses particles transported laterally.

In this study, the highest flux between 100 and 200 m was at location 1, where surface chlorophyll was also highest. However, the magnitude of flux did not always correlate with surface chlorophyll. Location 4 had high flux at 150m, though surface chlorophyll was very low. We found therefore that surface productivity does not always correlate with flux at depth.

The efficiency of export was affected by trophic structure. At location 1, flux was very efficient as anchovies directly grazed on primary producers, and then produced dense, fast sinking pellets. At location 2, though copepods were ubiquitous higher in the water column and their fecal pellets an important contributor to flux at 150m, they had largely disappeared by 250m depth. Their pellets were therefore not significant contributors to carbon flux deeper in the mesopelagic. Likely, this is due to the fast cycling of copepod pellets in the surface.

At both location 2, and also to an extent at location 1, there was a shift from fecal pellets near surface, to large aggregates at depth. At location 3 and 4, these large aggregates were present at all depths. These aggregates, which resembled discarded larvacean feeding webs, were abundant. This allows for particles that would otherwise be non-sinking, or very slowly sinking, to aggregate within the mucous webs, leading to more efficient export. The amount of POC present in small, non-sinking particles decreased with distance offshore. Westward moving currents laterally transported waters over the continental shelf with a high concentration of small particles offshore.

The flux profiles observed at all locations were unlike that of the Martin curve. As mentioned previously, the VERTEX 1 site in the classic Martin et al. (1987) study was located very close to our location 1 and 2 and was also made in June with similar upwelling

conditions. The reason for the differing vertical profiles of the VERTEX 1 site compared with our location 1, along with our further offshore sites, may be related to the width of the continental shelf at the two different studies. It may also be that surface tethered PIT traps are biased against aggregates greater than 1 mm as suggested by Bishop et al. (2016), which may lead to an under collection of material of large aggregates in near shore regions with strong horizontal currents.

Variations in the efficiency of sedimentation of particulate carbon in these regions will have significant impact on the ultimate rate of CO_2 uptake by the oceans. In coastal regions, carbon export needs to be understood both laterally and vertically. Autonomous observations with lagrangian instruments provides a 3D view on mechanisms of export in these regions.

Chapter 5

Conclusions and Future Research

5.1 Conclusions

In chapter 2 of this paper, using a large dataset of particle data, I presented a model which predicts global distributions of Cd. Clear patterns can be seen in the global distributions; high concentrations of Cd in particles is highly correlated to High Nutrient Low Chlorophyll areas. Uptake of Cd by plants likely is unintentional, a byproduct of transporter sites on the outside of the cell targeting essential divalent metals such as Zn and Fe(II), accidentally taking up Cd when concentrations of their intended target are low. These large-scale global patterns are therefore likely explained by processes on the cellular level. A second finding in this study was that particulate P likely occurs in 2 forms with different labilities; one phase that is more labile than Cd and another that is less labile than Cd. These differences in remineralization can explain the observed subsurface particulate Cd:P peaks which occurred near the base of the euphotic zone.

In chapter 3, I presented the development of a sampling system for the Carbon Flux Explorer and the subsequent first calibration of optical properties measured by the CFE in terms of carbon and nitrogen, essential for the development of a fully autonomous sensor. This calibration of volume attenuance flux (VAF) against organic carbon and nitrogen overcomes a key barrier and is an important step forward in the advancement of autonomous optical carbon export observations. The use of high frequency observations will significantly better inform carbon export simulations and food web models. The successful calibration of VAF in terms of POC and PN justifies expanded deployments of instruments such as the Carbon Flux Explorer.

Chapter 4 utilized flux measurements collected with CFEs, and then applied the calibration, providing insight into carbon export dynamics beneath a productive filament. Surprisingly, flux was either stable, or in some cases increased with depth. This behavior is likely caused by lateral transport of material. At all sites, particles at depth were mm scale aggregates, indicating some process at depth led to aggregation. As these particles were mainly

visible in sites below 150 m, where turbulent mixing is lower than in shallower waters, we hypothesize that the most likely cause of formation was filtration and subsequent export by organisms such as larvaceans.

5.2 Significance

Single cell plants living in the surface ocean drive the distribution of elements necessary to life in the ocean. To understand the processes that drives the availability of these elements horizontally and vertically therefore requires both a broad global understanding of distribution and also very small scale to the organism level. The finding in chapter 2, that inadvertent uptake of Cd by transporter sites in regions with low concentrations of necessary divalent trace metals likely increases the Cd:P in particles, exemplifies this.

For elements such as carbon, which have a gas phase, the uptake and subsequent export not only influence their global distribution in the ocean, but also their atmospheric concentrations. As CO_2 is a greenhouse gas, whose concentrations are rapidly increasing due to the burning of fossil fuels, understanding how the biological pump moves carbon into the deep ocean, and predicting how this may change in the future is essential. In chapter 4, I show how in a dynamic coastal region, export at depth is not just proportional to surface productivity. High levels of sinking biomass at depth are likely due to the lateral transport of material from the shallow continental shelf region and the aggregation of small particles. These mechanisms lead to a higher amount of carbon at depth contrary to what a classic Martin curve would predict. Local studies, using lagrangian, high frequency observers are necessary to understand mechanisms of carbon export to better inform global carbon cycle and food web models.

5.3 Future Research

5.3.1 Expanding Calibration Study

The calibration of optical properties measured by the Carbon Flux Explorer in terms of particulate organic carbon and nitrogen presented in Chapter 3 utilized particles collected over a broad range of fluxes with large variation in particle size distribution. All particles however were collected at 150m. In the future, calibration samples should be collected at other depths down to 500m. As particles sink deeper in the water column, respiration of material by microbes will remove carbon from the particulate pool. This could affect the VAF:POC ratio, depending on both the remineralization rate and the particle sinking rate.

As the assemblage of phytoplankton and zooplankton can vary regionally, we would ideally also like to collect samples from different areas to make the calibration more robust.

5.3.2 Deploying Multiple CFEs over Long Timescales

The deployments off the coast of California, the subject of Chapter 4, gave insight to how export varies over the evolution of a productive filament. In the future, multiple CFEs should be deployed for longer timescales from the beginning of the filament to the end. One limitation of the June 2017 study was that CFEs could only be deployed for 3 to 4 days at each location. Deploying multiple CFEs for 30 days would allow the CFEs to track the same water mass continuously over the filament evolution. This would create a more comprehensive view of particle export in the coastal region.

On an even larger scale, similar deployments should be done in other Eastern boundary upwelling regions, such as off the coast of Peru. By studying export in other regions, we can develop an understanding of if the export observations we saw off Point Conception are typical and if we can predict export in upwelling regions.

References

Archer, D. E., T. Takahashi, S. Sutherland, J. Goddard, D. Chipman, K. Rodgers, and H. Ogura (1996), Daily, seasonal and interannual variability of sea-surface carbon and nutrient concentration in the equatorial Pacific Ocean, *Deep Sea Res. Part II Top. Stud. Oceanogr.*, 43(96), 779–808. doi: 10.1016/0967-0645(96)00017-3

Baars, O., W. Abouchami, S. Galer, M. Boye, and P. Croot (2014), Dissolved cadmium in the Southern Ocean: Distribution, speciation, and relation to phosphate, *Limnol. Ocean.*, *59*(2), 385–399, doi:10.4319/lo.2014.59.2.0385

Bacon, M. P., Cochran, J. K., Hirschberg, D., Hammar, T. R., & Fleer, A. P. (1996). Export flux of carbon at the equator during the eqpac time-series cruises estimated from234th measurements. Deep-Sea Research Part II: Topical Studies in Oceanography, 43(4–6), 1133–1153. https://doi.org/10.1016/0967-0645(96)00016-1

Banse, K. (2013), Reflections About Chance in My Career, and on the Top-Down Regulated World. *Annual Review of Marine Science*, *5*(1), 1–19, doi: 10.1146/annurev-marine-121211-172359

Bar-On, Y.M., R. Phillips and R. Milo (2018), The biomass distribution on Earth, *PNAS*, 115 (25) 6506-6511, doi: 10.1073/pnas.1711842115

Bathmann, U.V., T.T. Noji, M. Voss and R. Peinert (1987), Copepod fecal pellet: abundance, sedimentation and content at a permanent station in the Norwegian Sea in May/June 1986. *Mar. Ecol. Prog. Ser.*, 38, 45-51. doi: 10.3354/meps038045

Beaumont, K. L., G. V. Nash, & Davidson, A. T. (2002). Ultrastructure, morphology and flux of microzoo- plankton faecal pellets in an east Antarctic fjord, *Mar. Ecol. Prog. Ser.*, 245, 133–148. doi: 10.3354/meps245133

Berline, O., L. Stemmann, F. Lombard, and Gorsky, G. (2011). Impact of appendicularians on detritus and export fluxes: a model approach at DyFAMed site, 33. doi: 10.1093/plankt/fbq163

Bishop, J. K. B., Ketten, D. R., & Edmond, J. M. (1978), The chemistry, biology and vertical flux

of particulate matter from the upper 400 m of the Cape Basin in the southeast Atlantic Ocean, *Deep-Sea Research*, *25*(12). doi: 10.1016/0146-6291(78)90010-3

Bishop J. K.B., S. E. Calvert S., and M. Y. S. Soon (1999), Spatial and temporal variability of POC in the northeast subarctic Pacific, *Deep. Res. Part II Top. Stud. Oceanogr.*, *46*(11–12), 2699–2733, doi:10.1016/S0967-0645(99)00081-8

Bishop, J. K. B., Davis, R. E., & Sherman, J. T. (2002), Robotic observations of dust storm enhancement of carbon biomass in the North Pacific, *Science*, *298*(5594), 817–821. doi: 10.1126/science.1074961

Bishop, J. K. B., Wood, T. J., Davis, R. E., & Sherman, J. T. (2004). Robotic observations of enhanced carbon biomass and export at 55 degrees during SOFeX, *Science*, *304*(5669), 417–420. doi: 10.1126/science.1087717

Bishop, J. K. B., & Wood, T. J. (2008). Particulate matter chemistry and dynamics in the twilight zone at VERTIGO ALOHA and K2 sites. *Deep-Sea Research Part I: Oceanographic Research Papers*, *55*(12), 1684–1706. https://doi.org/10.1016/j.dsr.2008.07.012

Bishop, J. K. B., & Wood, T. J. (2009). Year-round observations of carbon biomass and flux variability in the Southern Ocean. *Global Biogeochemical Cycles*, *23*(2), 1–12. doi: 10.1029/2008GB003206

Bishop, J. K. B., Lam, P. J., & Wood, T. J. (2012). Getting good particles: Accurate sampling of particles by large volume in-situ filtration. *Limnology and Oceanography: Methods*, *10*, 681–710. doi: 10.4319/lom.2012.10.681

Bishop, J. K. B., Fong, M. B., & Wood, T. J. (2016), Robotic observations of high wintertime carbon export in California coastal waters. *Biogeosciences*, *13*(10), 3109–3129. doi: 10.5194/bg-13-3109-2016

Boss, E., Guidi, L., Richardson, M. J., Stemmann, L., Gardner, W., Bishop, J. K. B., et al. (2015), Optical techniques for remote and in-situ characterization of particles pertinent to GEOTRACES, *Progress in Oceanography*, *133*, 43–54, doi: 10.1016/j.pocean.2014.09.007

Bourne, H.L., J.K.B. Bishop, P.J. Lam and D.C. Ohnemus (2018) Global spatial and temporal variation of Cd:P in euphotic zone particulates, *Global Biogeochemical Cycles*, 32, 1123-1141, doi: 10.1029/2017GB005842

Bourne, H.L., J.K.B. Bishop, T.J.Wood, T.J.Loew and Y. Liu, (in review), Carbon flux explorer

optical assessment of C, N and P fluxes, *Biogeosciences*

Bourne, H.L., J.K.B. Bishop, T.J.Wood and B. Connors (in prep), Carbon export beneath a dynamic upwelled filament off the coast of California, *Global Biogeochemical Cycles*

Boyd, P. W., and T. W. Trull (2007), Understanding the export of biogenic particles in oceanic waters: Is there consensus? *Progress in Oceanography*, 72(4), 276–312, doi: 10.1016/j.pocean.2006.10.007

Boyle, E. A. (1988), Cadmium: Chemical tracer of deepwater paleoceanography, *Paleoceanography*, 3(4), 471–489, doi:10.1029/PA003i004p00471.

Boyle, E.A., F. Sclater and J.M. Edmund (1976) On the marine geochemistry of Cadmium, *Nature*, 263, 42-44, doi: 10.1038/263042a0

Briggs, N., Perry, M. J., Cetinić, I., Lee, C., D'Asaro, E., Gray, A. M., & Rehm, E. (2011). High-resolution observations of aggregate flux during a sub-polar North Atlantic spring bloom. *Deep Sea Research Part I: Oceanographic Research Papers*, *58*(10), 1031–1039, doi: 10.1016/j.dsr.2011.07.007

Bruland Kenneth W. Knauer George A. Martin John H., (1978), Cadmium in northeast Pacific waters, *Limnology and Oceanography*, 23, doi: 10.4319/lo.1978.23.4.0618.

Bruland, K.W. (1980) Oceanographic distribution of cadmium, zinc, nickel and copper in the North Pacific, *Earth Planet. Sci. Lett.,* 47, 176-198

Bruland, K.W. and R.P. Franks (1983) Trace Elements in Sea Water in *Chemical Oceanography* edited by J.P. Riley and R. Chester, pp. 157-220, Vol. 8. Academic Press, London.

Buesseler, K. O., A. N., Antia, M., Chen, S. W., Fowler, W. D., Gardner, O., Gustafsson, et al. (2007). An assessment of the use of sediment traps for estimating upper ocean particle fluxes, *Journal of Marine Research*, *65*(3), 345–416, doi: 10.1357/002224007781567621

Buesseler, K. O., Lamborg, C. H., Boyd, P. W., Lam, P. J., Trull, T. W., Bidigare, R. R., et al. (2007b). Revisiting carbon flux through the ocean's twilight zone, *Science*, 316 (5824), 567–571, doi: 10.1126/science.1137959

Burd, A. B., D.A., Hansell, D.K., Steinberg, T.R., Anderson, J., Arístegui, F., Baltar, et al. (2010). Assessing the apparent imbalance between geochemical and biochemical indicators of meso- and bathypelagic biological activity: What the @$♯! is wrong with present calculations of

carbon budgets? *Deep Sea Research Part II: Topical Studies in Oceanography*, *57*(16), 1557–1571. doi:/10.1016/j.dsr2.2010.02.022

Chase, Z., P. G., Strutton, and B., Hales (2007) Iron links river runoff and shelf width to phytoplankton biomass along the U.S. West Coast, *Geophysical Research Letters*, 316, 567-571, doi: 10.1029/2006GL028069

Chavez, F.P. and R.T. Barber (1987), An estimate of new production in the equatorial Pacific, *Deep-Sea Research,* 34, 1229-1243

Coale, K. H. et al. (2004), Southern Ocean iron enrichment experiment: carbon cycling in high- and low-Si waters., *Science*, *304*(5669), 408–414, doi:10.1126/science.1089778.

Collier, R. and J. Edmond (1984), The trace element geochemistry of marine biogenic particulate matter, *Progress in Oceanography,* 13, 113-199.

Cox, A. D. (2011), Interactions of cadmium, zinc, and phosphorus in marine Synechococcus : field uptake, physiological and proteomic studies, Ph.D., Woods Hole Oceanographic Institution, Woods Hole MA .

Cox, A. D., and M. a. Saito (2013), Proteomic responses of oceanic Synechococcus WH8102 to phosphate and zinc scarcity and cadmium additions, *Front. Microbiol.*, *4*(DEC), 1–17, doi:10.3389/fmicb.2013.00387.

Croot, P. L., Baars, O., & Streu, P. (2011). The distribution of dissolved zinc in the Atlantic sector of the Southern Ocean. *Deep Sea Research Part II: Topical Studies in Oceanography*, *58*(25–26), 2707–2719. doi:10.1016/j.dsr2.2010.10.041

Cullen, J. T. (2006), On the nonlinear relationship between dissolved cadmium and phosphate in the modern global ocean: Could chronic iron limitation of phytoplankton growth cause the kink?, *Limnol. Oceanogr.*, *51*(3), 1369–1380, doi:10.4319/lo.2006.51.3.1369.

Cullen, J. T., and R. M. Sherrell (2005), Effects of dissolved carbon dioxide, zinc, and manganese on the cadmium to phosphorus ratio in natural phytoplankton assemblages, *Limonology Oceanogr.*, *50*(4), 1193–1204, doi:10.4319/lo.2005.50.4.1193.

Cullen, J. T., T. W. Lane, F. M. M. Morel, and R. M. Sherrell (1999), Modulation of cadmium uptake in phytoplankton by seawater CO2 concentration, *Nature*, *402*(6758), 165–167,

doi:10.1038/46007.

Cullen, J.T. and M.T. Maldonado (2013), Biogeochemistry of Cadmium and Its Release to the Environment in *Cadmium: From Toxicity to Essentiality*, edited by A. Sigel et al., pp. 31-62, Springer.

Danielsson, L.G. and S. Westerlund (1983) Trace metals in the Arctic Ocean in *Trace Metals in Sea Water*, pp. 85-96, edited by C.S. Wong et al., Plenum Press, New York.

Dunne, J. P., J. W. Murray, and a. K. Aufdenkampe (1999), Silicon -Nitrogen in the equatorial Pacific upwelling zone, *Global Biogeochem. Cycles*, *13*(3), 715–726, doi:10.1029/1999GB900031.

Dunne, J. P., Armstrong, R.A., Anand, G., & L., S. J. (2005). Empirical and mechanistic models for the particle export ratio. *Global Biogeochemical Cycles*, *19*(4). DOI: 10.1029/2004GB002390

Ebersbach, F., Trull, T. W., Davies, D. M., & Bray, S. G. (2011). Controls on mesopelagic particle fluxes in the Sub-Antarctic and Polar Frontal Zones in the Southern Ocean south of Australia in summer-Perspectives from free-drifting sediment traps. *Deep-Sea Research Part II: Topical Studies in Oceanography*, *58*(21–22), 2260–2276, doi: 10.1016/j.dsr2.2011.05.025

Elderfield, H., and R. Rickaby (2000), Oceanic Cd/P ratio and nutrient utilization in the glacial Southern Ocean, *Nature*, *405*(6784), 305–10, doi:10.1038/35012507.

Estapa, M. L., Buesseler, K., Boss, E., & Gerbi, G. (2013). Autonomous, high-resolution observations of particle flux in the oligotrophic ocean. *Biogeosciences*, *10*(8), 5517–5531. doi: 10.5194/bg-10-5517-2013

Estapa, M. L., Siegel, D. A., Buesseler, K. O., Stanley, R. H. R., Lomas, M. W., & Nelson, N. B. (2015). Global Biogeochemical Cycles in the Sargasso Sea, 1266–1282. https://doi.org/10.1002/2014GB004913.Received

Estapa, M., Durkin, C., Buesseler, K., Johnson, R., & Feen, M. (2017). Carbon flux from bio-optical profiling floats: Calibrating transmissometers for use as optical sediment traps. *Deep-Sea Research Part I: Oceanographic Research Papers*, *120*(December 2016), 100–111. https://doi.org/10.1016/j.dsr.2016.12.003

Falkowski, P. G., Barber, R. T., & Smetacek, V. (1998). Biogeochemical Controls and Feedbacks

on Ocean Primary Production. *Science*, *281*(5374), 200 LP-206. Retrieved from http://science.sciencemag.org/content/281/5374/200.abstract

Finkel, Z. V., a. S. Quigg, R. K. Chiampi, O. E. Schofield, and P. G. Falkowski (2007), Phylogenetic diversity in cadmium : phosphorus ratio regulation by marine phytoplankton, *Limnol. Oceanogr.*, *52*(3), 1131–1138, doi:10.4319/lo.2007.52.3.1131.

Freeland, H. (2007), A short history of Ocean Station Papa and Line P, *Prog. Oceanogr.*, *75*(2), 120–125, doi:10.1016/j.pocean.2007.08.005.

Gardner, W. D., Richardson, M. J., & Smith Walker O., J. (2000). Seasonal patterns of water column particulate organic carbon and fluxes in the Ross Sea, Antarctica. *Deep-Sea Research Part II: Topical Studies in Oceanography*, *47*(15–16), 3423–3449

Giering, S. L. C., Sanders, R., Martin, A. P., Henson, S. A., Riley, J. S., Marsay, C. M., & Johns, D. G. (2017), Particle flux in the oceans: Challenging the steady state assumption, *Global Biogeochemical Cycles*, 31(1), 159–171. doi: 10.1002/2016GB005424

González, H. E. (1992), Distribution and abundance of minipellets around the Antarctic peninsula. Implications for protistan feeding behaviour, *Mar. Ecol. Prog. Ser.*, 90, 223-236, doi: 10.3354/meps090223

González, H. E., V. C., Ortiz, and M., Sobarzo (2000). The role of faecal material in the particulate organic carbon flux in the northern Humboldt Current, Chile (23°S), before and during the 1997 – 1998 El Niño, *Journal of Plankton Research*, 22(3), 499–529, doi: 10.1093/plankt/22.3.499

Gorsky, G. and R. Fenaux (1998), The role of appendicularia in marine food webs, The Biology of Pelagic Turnicates, Oxford University Press, Oxford, 161-169

Gowing, M.M. (1989). Abundance and feeding ecology of Antarctic phaeodarian radiolarians, *Marine Biology*, 103, 107-118. doi: 10.1007/BF00391069

Gruber, N., Lachkar, Z., Frenzel, H., Marchesiello, P., Münnich, M., McWilliams, J. C., et al. (2011), Eddy-induced reduction of biological production in eastern boundary upwelling systems, *Nature Geoscience*, 4(11), 787–792, doi: 10.1038/ngeo1273

Hansen, J. L. S., T., Kiorboe and A. L. Alldredge (1996), Marine snow derived from abandoned larvacean houses: sinking rates, particle content and mechanisms of aggregate formation, *Geophysical Research Letters*, 141, 205-215

Hatta, M., Measures, C. I., Wu, J., Roshan, S., Fitzsimmons, J. N., Sedwick, P., & Morton, P. (2014), An overview of dissolved Fe and Mn Distributions during the 2010–2011 U.S. GEOTRACES north Atlantic Cruises: GEOTRACES GA03. *Deep Sea Research Part II: Topical Studies in Oceanography*, *116*, 117–129. doi:10.1016/j.dsr2.2014.07.005

Henson, S. A., Sanders, R., Madsen, E., Morris, P. J., Le Moigne, F., & Quartly, G. D. (2011). A reduced estimate of the strength of the ocean's biological carbon pump. *Geophysical Research Letters*, 38(4), 10–14. https://doi.org/10.1029/2011GL046735

Ho, T.Y., Quigg A., Finkel Z.V., Milligan A.J., Wyman K., Falkowski P.G. and F.M.M. Morel (2003), The elemental compostion of some marine phytoplankton, *J. Phycol*. 39, 1145-1159, doi: 10.1111/j.0022-3646.2003.03-090.x.

Holser, R. R., Goni, M. A., & Hales, B. (2011). Design and application of a semi-automated filtration system to study the distribution of particulate organic carbon in the water column of a coastal upwelling system. *Marine Chemistry*, *123*(1–4), 67–77. https://doi.org/10.1016/j.marchem.2010.10.001

Horner, T. J., R. B. Y. Lee, G. M. Henderson, and R. E. M. Rickaby (2013), Nonspecific uptake and homeostasis drive the oceanic cadmium cycle., *Proc. Natl. Acad. Sci. U. S. A.*, *110*(7), 2500–5, doi:10.1073/pnas.1213857110.

Janssen, D. J., T. M. Conway, S. G. John, J. R. Christian, D. I. Kramer, T. F. Pedersen, and J. T. Cullen (2014), Undocumented water column sink for cadmium in open ocean oxygen-deficient zones, *Proc. Natl. Acad. Sci.*, *111*(19), 6888–6893, doi:10.1073/pnas.1402388111.

John, S. G., J., Helgoe, and E., Townsend (2017), Biogeochemical cycling of Zn and Cd and their stable isotopes in the Eastern Tropical South Pacific, *Marine Chemistry*, doi:10.1016/j.marchem.2017.06.001

Johnson, K. S., F. P. Chavez and G. E. Friderich (1999), Continental-shelf sediment as a primary source of iron for coastal phytoplankton, *Nature*, 398, 697-699, doi:10.1038/19511.

Johnson, K. S., Plant, J. N., Dunne, J. P., Talley, L. D., & Sarmiento, J. L. (2017). Annual nitrate drawdown observed by SOCCOM profiling floats and the relationship to annual net community production. *Journal of Geophysical Research: Oceans*, 122(8), 6668–6683. doi: 10.1002/2017JC012839

Krause, M. (1981). Vertical distributions of fecal pellets during FLEX '76. *Helgolander Meersesunters*, 34(3), 313-327, doi: 10.1007/BF02074125

Kwon, E. Y., F., Primeau, and J. L., Sarmiento (2009), The impact of remineralization depth on the air–sea carbon balance, *Nature Geoscience*, 2, 630-635

Lam, P. J., & Bishop, J. K. B. (2007), High biomass, low export regimes in the Southern Ocean, *Deep-Sea Research Part II: Topical Studies in Oceanography*, 54(5–7), 601–638. doi: 10.1016/j.dsr2.2007.01.013

Lam, P. J., and J. K. B. Bishop (2008), The continental margin is a key source of iron to the HNLC North Pacific Ocean, *Geophys. Res. Lett.*, *35*(7), 1–5, doi:10.1029/2008GL033294

Lam, P. J., J. K. B. Bishop, C. C. Henning, M. a. Marcus, G. a. Waychunas, and I. Y. Fung (2006), Wintertime phytoplankton bloom in the subarctic Pacific supported by continental margin iron, *Global Biogeochem. Cycles*, *20*(1), 1–12, doi:10.1029/2005GB002557

Landry, M. R., J. Constantinou, and J. Kirshtein (1995), Microzooplankton grazing in the central equatorial Pacific during February and August, 1992, *Deep Sea Res. Part II Top. Stud. Oceanogr.*, 42(2–3), 657–671, doi:10.1016/0967-0645(95)00024-K

Lane, E. S., D. M. Semeniuk, R. F. Strzepek, J. T. Cullen, and M. T. Maldonado (2009), Effects of iron limitation on intracellular cadmium of cultured phytoplankton: Implications for surface dissolved cadmium to phosphate ratios, *Mar. Chem.*, *115*(3–4), 155–162, doi:10.1016/j.marchem.2009.07.008

Lane, E. S., K. Jang, J. T. Cullen, and M. T. Maldonado (2008), The interaction between inorganic iron and cadmium uptake in the marine diatom Thalassiosira oceanica, *Limnol. Oceanogr.*, *53*(5), 1784–1789, doi:10.4319/lo.2008.53.5.1784.

Lane, T. W., and F. M. Morel (2000), A biological function for cadmium in marine diatoms., *Proc. Natl. Acad. Sci. U. S. A.*, *97*(9), 4627–4631, doi:10.1073/pnas.090091397.

Lee, J.-M., Heller, M.I., Lam, P.J., (2018), Size distribution of particulate trace elements in the U.S. GEOTRACES Eastern Pacific Zonal Transect (GP16), *Marine Chemistry*, https://doi.org/10.1016/j.marchem.2017.09.006.

Lee, J.L., S.B. Roberts and F. M. M. Morel (1995), Cadmium: A nutrient for the marine diatom

Thalassiosira weissflogii, *Limnol. Oceanogr.,* 40(6) 1056-1063, doi: 10.4319/lo.1995.40.6.1056/

Li, Z., and N., Cassar (2011), Satellite estimates of net community production based on O2/Ar observations and comparisons to other estimates, *Global Biogeochemical Cycles*, 735–752, doi: 10.1002/2015GB005314

Lohan, M. C., D. W. Crawford, D. a. Purdie, and P. J. Statham (2005), Iron and zinc enrichments in the northeastern subarctic Pacific: ligand production and zinc availability in response to phytoplankton growth, , *50*(5), 1427–1437, doi:10.4319/lo.2005.50.5.1427

Lohan, M. C., P. J. Statham, and D. W. Crawford (2002), Total dissolved zinc in the upper water column of the subarctic North East Pacific, *Deep. Res. Part II Top. Stud. Oceanogr.*, *49*(24–25), 5793–5808, doi:10.1016/S0967-0645(02)00215-1

Lutz, M., Caldeira, K., Dunbar, R., and Behrenfeld, M.: Seasonal rhythms of net primary production and particulate organic carbon flux to depth describe the efficiency of biological pump in the global ocean, *J. Geophys. Res.-Oceans*, 112, C10011, doi:10.1029/2006JC003706, 2007

Lynn, R. J. and J. J. Simpson (1987), The California Current System: The Seasonal Variability of its Physical Characteristics*, Journal of Physical Research,* 92 (12), 12947-12966, doi.org/10.1029/JC092iC12p12947

Madin, L.P. and J.E. Purcell, (1992), Feeding, metabolism and growth of Cyclosapa Bakeri in the subarctic Pacific, *Limnology and Oceanography*, 37(6), 1236-1251, doi: 10.4319/lo.1992.37.6.1236

Marsay, C. M., Sanders, R. J., Henson, S. a, Pabortsava, K., & Achterberg, E. P. (2014). Attenuation of sinking particulate organic carbon flux through the mesopelagic ocean. https://doi.org/10.1073/pnas.1415311112

Martin, J. H., Knauer, G. a., Karl, D. M., & Broenkow, W. W. (1987). VERTEX: carbon cycling in the northeast Pacific. Deep Sea Research Part A. Oceanographic Research Papers, 34(2), 267–285. https://doi.org/10.1016/0198-0149(87)90086-0

Martin, J. H., R. M. Gordon, S. Fitzwater, and W. W. Broenkow (1989), Vertex: phytoplankton/iron studies in the Gulf of Alaska, *Deep Sea Res. Part A. Oceanogr. Res. Pap.*,

36(5), 649–680, doi:10.1016/0198-0149(89)90144-1

Mawji, E., et al., The GEOTRACES Intermediate Data Product 2014, Mar. Chem. (2015), http://dx.doi.org/10.1016/ j.marchem.2015.04.005

Mcdonnell, A. M. P., Boyd, P. W., & Buesseler, K. O. (2015), *Global Biogeochemical Cycles*, 175–193. https://doi.org/10.1002/2014GB004935

McPhee-Shaw, E.E., R.W. Sternberg, B. Mullenbach and A.S. Ogston (2004), Observations of intermediate nepheloid layers on the northern California continental margin, *Continental Shelf Research*, 24(6), 693-720, doi: 10.1016/j.csr.2004.01.004

Morrow, R. M., Ohman, M. D., Goericke, R., Kelly, T. B., Stephens, B. M., & Stukel, M. R. (2018), CCE V: Primary production, mesozooplankton grazing, and the biological pump in the California Current Ecosystem: Variability and response to El Niño. *Deep-Sea Research Part I: Oceanographic Research Papers*, 1–28. https://doi.org/10.1016/j.dsr.2018.07.012

Murray, R. W., and M. Leinen (1996), Scavenged excess aluminum and its relationship to bulk titanium in biogenic sediment from the central equatorial Pacific Ocean, *Geochim. Cosmochim. Acta*, *60*(20), 3869–3878, doi:10.1016/0016-7037(96)00236-0

Nothig, E. M., and B. V. Bodungen (1989), Occurrence and vertical flux of faecal pellets of probably protozoan origin in the southeastern Weddell Sea (Antarctica), *Mar. Ecol. Prog. Ser*., 56, 281-289, doi 10.3354/meps056281

Ohman, M., Barbeau, K., Franks, P., Goericke, R., Landry, M., & Miller, A. (2013). Ecological Transitions in a Coastal Upwelling Ecosystem. Oceanography, 26(3), 210–219, https://doi.org/10.5670/oceanog.2013.65

Ohnemus, D.C., Lam, P.J., 2015. Cycling of lithogenic marine particles in the US GEOTRACES North Atlantic transect. Deep Sea Research Part II: Topical Studies in Oceanography 116, 283-302. http://dx.doi.org/10.1016/j.dsr2.2014.11.019

Omand, M. M., Asaro, E. A. D., Lee, C. M., Jane, M., Briggs, N., Cetini, I., & Mahadevan, A. (2015). Eddy-driven subduction exports particulate organic carbon from the spring bloom, (March), 1–10.

Owens, S.A., K.O. Buesseler, C.H. Lamborg, J. Valdes, M.W. Lomas, R.J. Johnson

Pak, H., Zaneveld, R. V. and Kitchen J. (1980). Intermediate Nepheloid Layers Observed off Oregon and Washington. *Journal of Geophysical Research,* 85(11), 6697-6708, doi.org/10.1029/JC085iC11p06697.

Palmiter, R. D. (1998), The elusive function of metallothioneins., *Proc. Natl. Acad. Sci. U. S. A.*, *95*(15), 8428–8430, doi:10.1073/pnas.95.15.8428.

Passow, U. (2012). The biological pump in a high CO2 world . *Marine Ecology Progress Series*, *470*, 249–271.

Pomeroy, L.R., Hanson, R.B., McGillivary, P.A., B.F. Sherr, D. Kirchman, D. and D. Deibel. (1984) Microbiology and chemistry of fecal products of pelagic turnicates: rates and fates. *Bull. Mar. Sci.,* 35 (3), 426-439.

Price, N.M. and F.M.M. Morel (1990) Cadmium and colbalt substitiutions for zinc in a marine diatom. *Nature,* 344, 658-660

Quay, P., J. Cullen, W. Landing, and P. Morton (2015), Processes controlling the distributions of Cd and PO4 in the ocean, *Global Biogeochem. Cycles, 29,* 830-841, do1:10.10002/2014GB004998.

Resing, J. A., Sedwick, P. N., German, C. R., Jenkins, W. J., Moffett, J. W., Sohst, B. M., & Tagliabue, A. (2015). Basin-scale transport of hydrothermal dissolved metals across the South Pacific Ocean. *Nature*, *523*(7559), 200–203. doi:10.1038/nature14577

Robbins, L. J., S. V. Lalonde, M. a. Saito, N. J. Planavsky, a. M. Mloszewska, E. Pecoits, C. Scott, C. L. Dupont, a. Kappler, and K. O. Konhauser (2013), Authigenic iron oxide proxies for marine zinc over geological time and implications for eukaryotic metallome evolution, *Geobiology*, *11*(4), 295–306, doi:10.1111/gbi.12036.

Saba, G. K., and D.K. Steinberg, (2012), Abundance, composition, and sinking rates of fish fecal pellets in the santa barbara channel. *Scientific Repo*rts, 2, 1–6, https://doi.org/10.1038/srep00716

Sabine, C.L., R. A. Freely, N. Gruber, R. M. Key, L. Kitack, J.L. Bullister, R. Wanninkhhof, C.S. Wong, D.W.R. Wallace, B. Tilbrook, F.J. Millero, T.-H. Peng, A. Kozyr, T. Ono and A.F. Rios (2004), The Oceanic Sink for Antropogenic CO2, *Science*, 305, 367-371, doi: 10.1126/science.1097403

Saito, M. A., D. M. Sigman, and F. M. M. Morel (2003), The bioinorganic chemistry of the ancient ocean: The co-evolution of cyanobacterial metal requirements and biogeochemical cycles at the Archean-Proterozoic boundary, *Inorganica Chim. Acta*, *356*, 308–318, doi:10.1016/S0020-1693(03)00442-0.

Sasaki, H., H. Hattori and S. Nishizawa (1988), Downward flux of particulate organic matter and vertical distribution of calanoid copepods in the Oyasio Waters in the summer, *Deep-Sea Res*., 35, 505-515

Siegel, D. A., Buesseler, K. O., Doney, S. C., Sailley, S. F., Behrenfeld, M. J., & Boyd, P. W. (2014). Global Biogeochemical Cycles. *Global Biogeochemical Cycles*, *28*, 181–196. https://doi.org/10.1002/2013GB004743.Received

Siegel, D. A., Buesseler, K. O., Behrenfeld, M. J., Benitez-nelson, C. R., Boss, E., Brzezinski, M. A., et al. (2016). Prediction of the Export and Fate of Global Ocean Net Primary Production : The EXPORTS Science Plan, 3(March), 1–10. https://doi.org/10.3389/fmars.2016.00022

Siegelman-charbit, L., Koslow, J. A., Jacox, M. G., Hazen, E. L., Bograd, S. J., & Miller, E. F. (2018). Physical forcing on fish abundance in the southern California Current System, (May 2016). https://doi.org/10.1111/fog.12267

Silver, M. W., Coale, S. L., Pilskaln, C. H., & Steinberg, D. R. (1998). Giant aggregates: Importance as microbial centers and agents of material flux in the mesopelagic zone. Limnology and Oceanography, 43(3), 498–507, doi:10.4319/lo.1998.43.3.0498

Smetacek, V.S. (1980) Zooplankton standing stock, copepod faecal pellets and particulate detritus in Kiel bight, *Estuarine and Coastal Marine Science*, 11, 477-490, doi: 10.1016/S0302-3524(80)80001-6

Stanley, R. H. R., K.O. Buesseler, S.J. Manganini, D.K. Steinberg and J.R. Valdes (2004), A comparison of major and minor elemental fluxes collected in neutrally buoyant and surface-tethered sediment traps, *Deep-Sea Res. Pt. I*, 51, 1387–1395, doi: 0.1016/j.dsr.2004.05.010

Stanley, R. H. R., Doney, S. C., Jenkins, W. J., & Lott, D. E. (2012), Apparent oxygen utilization rates calculated from tritium and helium-3 profiles at the Bermuda Atlantic Time-series Study site. *Biogeosciences*, *9*(6), 1969–1983, doi: 10.5194/bg-9-1969-2012

Stemmann, L., and E., Boss (2012), Plankton and particle size and packaging: from determining optical properties to driving the biological pump. *Annual Review of Marine Science*, 4, 263–290

Stemmann, L., L., Prieur, L., Legendre, I., Taupier-Letage, M., Picheral, L., Guidi, and G., Gorsky (2008), Effects of frontal processes on marine aggregate dynamics and fluxes: an interannual study in a permanent geostrophic front (NW Mediterranean), *Journal of Marine Systems*, 70, 1–20

Stukel, M. R., Ohman, M. D., Benitez-Nelson, C. R., & Landry, M. R. (2013), Contributions of mesozooplankton to vertical carbon export in a coastal upwelling system. *Mar. Ecol. Prog. Ser.*, 491, 47–65, https://doi.org/10.3354/meps10453

Stukel, M. R., Asher, E., Couto, N., Schofield, O., Strebel, S., Tortell, P., & Ducklow, H. W. (2015). Global Biogeochemical Cycles. Global Biogeochemical Cycles, 29, 1400–1420. https://doi.org/10.1002/2015GB005211

Stukel, M. R., Song, H., Goericke, R., & Miller, A. J. (2018). The role of subduction and gravitational sinking in particle export, carbon sequestration, and the remineralization length scale in the California Current Ecosystem, 363–383. https://doi.org/10.1002/lno.10636

Sunda, W. G., and S. a. Huntsman (1995), Cobalt and zinc interreplacement in marine phytoplankton: Biological and geochemical implications, *Limnol. Oceanogr.*, *40*(8), 1404–1417, doi:10.4319/lo.1995.40.8.1404

Sunda, W. G., and S. A. Huntsman (1996), Antagonism between cadmium and zinc toxicity and manganese limitation in a coastal diatom, *Limnol. Oceanogr.*, *41(3)*, 373-387, doi: 10.4319/lo.1996.41.3.0373

Sunda, W. G., and S. a. Huntsman (1998), Interactions among Cu2+, Zn2+, and Mn2+ in controlling cellular Mn, Zn, and growth rate in the coastal alga Chlamydomonas, *Limnol. Oceanogr.*, *43*(6), 1055–1064, doi:10.4319/lo.1998.43.6.1055

Sunda, W. G., and S. A. Huntsman (2000), Effect of Zn, Mn, and Fe on Cd accumulation in phytoplankton: Implications for oceanic Cd cycling, *Limnol. Oceanogr.*, *45*(7), 1501–1516, doi:10.4319/lo.2000.45.7.1501

Thunell, R. C. (1998). Particle fluxes in a coastal upwelling zone: sediment trap results from Santa Barbara Basin, California. *Deep Sea Research Part II: Topical Studies in Oceanography*, *45*(8), 1863–1884. https://doi.org/https://doi.org/10.1016/S0967-0645(98)80020-9

Turner, J. T. (2015). Progress in Oceanography Zooplankton fecal pellets, marine snow, phytodetritus and the ocean's biological pump. Progress in Oceanography, 130, 205–248. https://doi.org/10.1016/j.pocean.2014.08.005

Twining, B. S., and S. B. Baines (2013), The trace metal composition of marine phytoplankton, *Annual Review of Marine Scienc*e, 5(1), 191-215, doi:10.1146/annurev-marine-121211-172322

Urrère MA, Knauer GA (1981), Zooplankton fecal pellet fluxes and vertical transport of particulate organic material in the pelagic environment, *J Plankton Res*, 3: 369−387, doi: 10.1093/plankt/3.3.369

Waeles, M., H. Planquette, I. Afandi, N. Delebecque, F. Bouthir, A. Donval, R. U. Shelley, P.-A. Auger, R. D. Riso, and L. Tito de Morais (2016), Cadmium in the waters off South Morocco: Nature of particles hosting Cd and insights into the mechanisms fractionating Cd from phosphate, *J. Geophys. Res. Oceans*, 121, 3106–3120, doi: 10.1002/2016JC011688

Waeles, M., J.-F. Maguer, F. Baurand, and R. D. Riso (2013), Off Congo waters (Angola Basin, Atlantic Ocean): A hot spot for cadmium-phosphate fractionation, *Limnol. Oceanogr.*, *58*(4), 1481–1490, doi:10.4319/lo.2013.58.4.1481

Whitney, F.A. and H.J. Freeland (1999) Variability in upper-ocean water properties in the NE Pacific Ocean, *Deep Sea Research,*46, 2351-2370, doi: 10.1016/S0967-0645(99)00067-3.

Wyatt, N. J., A. Milne, E. M. S. Woodward, A. P. Rees, T. J. Browning, H. A. Bouman, P. J. Worsfold, and M. C. Lohan (2014), Biogeochemical cycling of dissolved zinc along the GEOTRACES South Atlantic transect GA10 at 40°S, *Global Biogeochem. Cycles*, 28, 44–56, doi:10.1002/2013GB004637

Xie, R.C., S. J. G. Galer, W. Abouchami, M. J. A. Rijkenberg, J. D. Jong, H. J. W. de Baar and M. O. Andreae (2015), The cadmium-phosphate relationship in the western South Atlantic - The importance of mode and intermediate waters on the global systematics., *Marine Chemistry*,

177, 110-123, doi: 10.1016/j.marchem.2015.06.011

Xu, Y., L. Feng, P. D. Jeffrey, Y. Shi, and F. M. M. Morel (2008), Structure and metal exchange in the cadmium carbonic anhydrase of marine diatoms., *Nature*, *452*(7183), 56–61, doi:10.1038/nature06636

Yao, X., & Schlitzer, R. (2013). Assimilating water column and satellite data for marine export production estimation. *Geoscientific Model Development*, *6*(5), 1575–1590. https://doi.org/10.5194/gmd-6-1575-2013

Yoder, J. A., S. G. Ackleson, R. T. Barber, P. Flament, and W. M. Balch (1994), A line in the sea, *Nature*, 371(6499), 689–692, doi:10.1038/371689a0